IFS DOCUMENTATION – Cy47r3
Operational implementation 12 Oct 2021

PART VII: ECMWF WAVE MODEL

REVISION HISTORY

Changes since CY46R1

- New wave physics in CY46r1.

Changes since CY43R1

None

Changes since CY41R2

- New subsection on Maximum Spectral Steepness in Chapter 2.
- New chapter 10 based on ECMWF Post-processing section in Chapter 6.

Chapter 1

Introduction

Table of contents

This document is partly based on Chapter III of "Dynamics and Modelling of Ocean Waves" by Komen *et al.* (1994). For more background information on the fundamentals of wave prediction models this book comes highly recommended. A comprehensive and more recent account of the theory of surface gravity waves (such as the coupling between wind and waves, nonlinear wave-wave interactions and freak waves) and the verification of model results is given by Janssen (2004). Here, after a historical introduction, we will describe the basic evolution equation, including a discussion of the parametrization of the source functions. This is then followed by a brief discussion of the ECMWF wave data assimilation scheme. The document closes with a presentation of the ECMWF version of the numerical scheme and the structure of the software.

1.1   BACKGROUND

The principles of wave prediction were already well known at the beginning of the 1960s. Yet none of the wave models developed in the 1960s and 1970s computed the wave spectrum from the full energy balance equation. Additional *ad hoc* assumptions have always been introduced to ensure that the wave spectrum complies with some preconceived notions of wave development that were in some cases not consistent with the source functions. The reasons for introducing simplifications in the energy balance equation were twofold. On the one hand, the important role of the wave–wave interactions in wave evolution was not recognized. On the other hand, the limited computer power in those days precluded the use of the nonlinear transfer in the energy balance equation.

The first wave models, which were developed in the 1960s and 1970s, assumed that the wave components suddenly stopped growing as soon as they reached a universal saturation level (Phillips, 1958). The saturation spectrum, represented by the one-dimensional f^{-5} frequency spectrum of Phillips and an empirical equilibrium directional distribution, was prescribed. Nowadays it is generally recognized that a universal high-frequency spectrum (in the region between 1.5 and 3 times the peak frequency) does not exist because the high-frequency region of the spectrum not only depends on whitecapping but also on wind input and on the low-frequency regions of the spectrum through nonlinear transfer. Furthermore, from the physics point of view, it has now become clear that these so-called first generation wave models exhibit basic shortcomings by overestimating the wind input and disregarding nonlinear transfer.

The relative importance of nonlinear transfer and wind input became more evident after extensive wave growth experiments (Mitsuyasu, 1968, 1969; Hasselmann *et al.*, 1973) and direct measurements of the wind input to the waves (Snyder *et al.*, 1981; Hasselmann *et al.*, 1986). This led to the development of second generation wave models which attempted to simulate properly the so-called overshoot phenomenon and the dependence of the high-frequency region of the spectrum on the low frequencies. However, restrictions resulting from the nonlinear transfer parametrization effectively required the spectral shape of the wind sea spectrum to be prescribed. The specification of the wind sea spectrum was imposed either at the outset in the formulation of the transport equation itself (parametrical or hybrid models) or as a side condition in the computation of the spectrum (discrete models). These models therefore suffered basic problems in the treatment of wind sea and swell. Although, for typical synoptic-scale wind fields the evolution towards a quasi-universal spectral shape could be justified by two scaling arguments (Hasselmann *et al.*, 1976), nevertheless complex wind seas generated by rapidly varying wind fields (in, for example, hurricanes or fronts) were not simulated properly by the second generation models.

The shortcomings of first and second generation models have been documented and discussed in the SWAMP wave-model intercomparison study (SWAMP Group (1985)). The development of third generation models was suggested in which the wave spectrum was computed by integration of the energy balance equation, without any prior restriction on the spectral shape. As a result the WAM Group was established, whose main task was the development of such a third generation wave model. In this document we shall describe the ECMWF version of the so-called WAM model.

Komen *et al.* (1994) gave an extensive overview of what is presently known about the physics of wave evolution, in so far as it is relevant to a spectral description of ocean waves. This covers detailed knowledge of the generation of ocean waves by wind and the impact of the waves on the air flow, the importance of the resonant nonlinear interactions for wave evolution, and the state of knowledge on spectral dissipation of wave energy by whitecapping and bottom friction.

1.2   STRUCTURE OF THE DOCUMENTATION

In this document we will try to make optimal use of the knowledge of wave evolution in the context of numerical modelling of ocean waves. However, in order to be able to develop a numerical wave model that produces forecasts in a reasonable time, compromises regarding the functional form of the source terms in the energy balance equation have to be made. For example, a traditional difficulty of numerical wave models has been the adequate representation of the nonlinear source term. Since the time needed to compute the exact source function expression greatly exceeds practical limits set by an operational wave model, some form of parametrization is clearly necessary. Likewise, the numerical solution of the momentum balance of air flow over growing ocean waves, as presented in Janssen (1989), is by far too time consuming to be practical for numerical modelling. It is therefore clear that a parametrization of the functional form of the source terms in the energy balance equation is a necessary step to develop an operational wave model.

The remainder of this document is organised as follows. In Chapter 2 we discuss the kinematic part of the energy balance equation: advection in both deep and shallow water, refraction due to currents and bottom topography. Chapter 3 is devoted to a parametrization of the input source term and the nonlinear interactions. The adequacy of these approximations is discussed in detail, as is the energy balance in growing waves.

In Chapter 4 a brief overview is given of the method that is used to assimilate Altimeter wave height data. This method is called Optimum Interpolation (OI) and is more or less a one to one copy obtained from the work of Lorenc (1981). A detailed description of the method that is used at ECMWF, including extensive test results is provided by Lionello *et al.* (1992). SAR data may be assimilated in a similar manner.

Next, in Chapter 5 we discuss the numerical implementation of the model. We distinguish between a prognostic part of the spectrum (that part that is explicitly calculated by the numerical model) (WAMDI Group (1988)), and a diagnostic part. The diagnostic part of the spectrum has a prescribed spectral shape, the level of which is determined by the energy of the highest resolved frequency bin of the prognostic part. Knowledge of the unresolved part of the spectrum allows us to determine the nonlinear energy transfer from the resolved part to the unresolved part of the spectrum. The prognostic part of the spectrum is obtained by numerically solving the energy balance equation. The choice of numerical schemes for advection, refraction and time integration is discussed. The integration in time is performed using a fully-implicit integration scheme in order to be able to use large time steps without incurring numerical instabilities in the high-frequency part of the spectrum. For advection and refraction we have chosen a first order, upwinding flux scheme. Advantages of this scheme are discussed in detail, especially in connection with the so-called garden sprinkler effect (see SWAMP Group (1985), p. 144). Alternatives to first order upwinding, such as the semi-Lagrangian scheme which is gaining popularity in meteorology, will be discussed as well.

Chapter 6, is devoted to software aspects of the WAM model code with emphasis on flexibility, universality and design choices. A brief summary of the detailed manual accompanying the code is given as well (Günther *et al.*, 1992). In Chapter 7 we give a list of applications of wave modelling at ECMWF, including the two-way interaction of winds and waves, while in Chapter 8 a brief description is given of a method to provide statistical information on extreme sea states from the two-dimensional wave spectrum. Chapter 9 describes how second order corrections can be computed and added to the first order spectra in order to compute the integrated parameters from the second order spectra. A brief description of the model output parameters and how they

are computed is given in Chapter 10. It does not however give a full description of how to make best use of these parameters.

Chapter 2

The kinematic part of the energy balance equation

Table of contents

In this chapter we shall briefly discuss some properties of the energy balance equation in the absence of sources and sinks. Thus, shoaling and refraction – by bottom topography and ocean currents – are investigated in the context of a statistical description of gravity waves.

2.1   BASIC TRANSPORT EQUATION

Let x_1 and x_2 be the spatial coordinates and k_1, k_2 the wave coordinates, and let

$$\mathbf{z} = (x_1, x_2, k_1, k_2) \tag{2.1}$$

be their combined four-dimensional vector. The most elegant formulation of the "energy" balance equation is in terms of the action density spectrum N which is the energy spectrum divided by the so-called intrinsic frequency σ. The action density plays the same role as the particle density in quantum mechanics. Hence there is an analogy between wave groups and particles, because wave groups with action N have energy σN and momentum kN. Thus, the most fundamental form of the transport equation for the action density spectrum $N(\mathbf{k}, \mathbf{x}, t)$ without the source term can be written in the flux form

$$\frac{\partial}{\partial t} N + \frac{\partial}{\partial z_i} (\dot{z}_i N) = 0 \tag{2.2}$$

where $\dot{\mathbf{z}}$ denotes the propagation velocity of a wave group in the four-dimensional phase space of $\mathbf{x}$ and $\mathbf{k}$. This equation holds for any field $\dot{\mathbf{z}}$, and also for velocity fields which are not divergence-free in four-dimensional phase space. In the special case when $\mathbf{x}$ and $\mathbf{k}$ represent a canonical vector pair – this is the case, for example, when they are the usual Cartesian coordinates – the propagation equations for a wave group (also known as the Hamilton–Jacobi propagation equations) are

$$\dot{x}_i = \frac{\partial}{\partial k_i} \Omega \tag{2.3a}$$

$$\dot{k}_i = -\frac{\partial}{\partial x_i} \Omega \tag{2.3b}$$

where Ω denotes the dispersion relation

$$\omega = \Omega(\mathbf{k}, \mathbf{x}, t) = \sigma + \mathbf{k} \cdot \mathbf{U} \tag{2.4}$$

with σ the so-called intrinsic frequency

$$\sigma = \sqrt{gk \tanh(kh)} \tag{2.5}$$

where the depth $h(\mathbf{x}, t)$ and the current $\mathbf{U}(\mathbf{x}, t)$ may be slowly-varying functions of $\mathbf{x}$ and t.

The Hamilton–Jacobi equations have some intriguing consequences. First of all, (2.3a) just introduces the group speed $\partial\Omega/\partial k_i$ while (2.3b) expresses conservation of the number of wave crests. Secondly, the transport equation for the action density may be expressed in the advection form

$$\frac{\mathrm{d}}{\mathrm{d}t}N = \frac{\partial N}{\partial t} + \dot{z}_i \frac{\partial}{\partial z_i}N = 0 \tag{2.6}$$

because, due to (2.3a) and (2.3b), the field $\dot{\mathbf{z}}$ for a continuous ensemble of wave groups is divergence-free in four-dimensional phase space so

$$\frac{\partial}{\partial z_i}\dot{z}_i = 0 \tag{2.7}$$

Thus, along a path in four-dimensional phase space defined by the Hamilton–Jacobi equations (2.3a) and (2.3b), the action density N is conserved. This property only holds for canonical coordinates for which the flow divergence vanishes (Liouville's theorem – first applied by Dorrestein (1960) to wave spectra). Thirdly, the analogy between Hamilton's formalism of particles with Hamiltonian H and wave groups obeying the Hamilton–Jacobi equations should be pointed out. Indeed, wave groups may be regarded as particles and the Hamiltonian H and angular frequency Ω play similar roles. Because of this similarity Ω is expected to be conserved as well (under the restriction that Ω does not depend on time). This can be verified by direct calculation of the rate of change of Ω following the path of a wave group in phase space,

$$\frac{\mathrm{d}}{\mathrm{d}t}\Omega = \dot{z}_i \frac{\partial}{\partial z_i}\Omega = \dot{x}_i \frac{\partial}{\partial x_i}\Omega + \dot{k}_i \frac{\partial}{\partial k_i}\Omega = 0 \tag{2.8}$$

The vanishing of $\mathrm{d}\Omega/\mathrm{d}t$ follows at once upon using the Hamilton–Jacobi equations (2.3a) and (2.3b). Note that the restriction of no time dependence of Ω is essential for the validity of (2.8), just as the Hamiltonian H is only conserved when it does not depend on time t. The property (2.8) will play an important role in our discussion of refraction.

Now turn to the important case of spherical coordinates. When one transforms from one set of coordinates to another there is no guarantee that the flow remains divergence-free. However, noting that (2.2) holds for any rectangular coordinate system, the generalization of the standard Cartesian geometry transport equation to spherical geometry is straightforward (see also Groves and Melcer (1961) and WAMDI Group (1988)). To that end let us consider the spectral action density $\hat{N}(\omega, \theta, \phi, \lambda, t)$ with respect to angular frequency ω and direction θ (measured clockwise relative to true north) as a function of latitude ϕ and longitude λ. The reason for the choice of frequency as the independent variable (instead of, for example, the wavenumber k) is that for a fixed topography and current the frequency Ω is conserved when following a wave group; therefore the transport equation is simplified. In general, the conservation equation for $\hat{N}$ thus reads

$$\frac{\partial}{\partial t}\hat{N} + \frac{\partial}{\partial\phi}(\dot{\phi}\hat{N}) + \frac{\partial}{\partial\lambda}(\dot{\lambda}\hat{N}) + \frac{\partial}{\partial\omega}(\dot{\omega}\hat{N}) + \frac{\partial}{\partial\theta}(\dot{\theta}\hat{N}) = 0 \tag{2.9}$$

and since $\dot{\omega} = \partial\Omega/\partial t$ the term involving the derivative with respect to ω drops out in the case of time-independent current and bottom. The action density $\hat{N}$ is related to the normal spectral density N with respect to a local Cartesian frame (x, y) through $\hat{N}\,\mathrm{d}\omega\,\mathrm{d}\theta\,\mathrm{d}\phi\,\mathrm{d}\lambda = N\,\mathrm{d}\omega\,\mathrm{d}\theta\,\mathrm{d}x\,\mathrm{d}y$, or

$$\hat{N} = NR^2\cos\phi \tag{2.10}$$

where R is the radius of the earth. Substitution of (2.10) into (2.9) yields

$$\frac{\partial}{\partial t}N + (\cos\phi)^{-1}\frac{\partial}{\partial\phi}(\dot{\phi}\cos\phi N) + \frac{\partial}{\partial\lambda}(\dot{\lambda}N) + \frac{\partial}{\partial\omega}(\dot{\omega}N) + \frac{\partial}{\partial\theta}(\dot{\theta}N) = 0 \tag{2.11}$$

With c_{g} the magnitude of the group velocity,

$$\dot{\phi} = (c_{\mathrm{g}}\cos\theta - \mathbf{U}|_{\text{north}})R^{-1} \tag{2.12a}$$

$$\dot{\lambda} = (c_{\mathrm{g}}\sin\theta - \mathbf{U}|_{\text{east}})(R\cos\phi)^{-1} \tag{2.12b}$$

$$\dot{\theta} = c_{\mathrm{g}}\sin\theta\tan\phi R^{-1} + (\dot{\mathbf{k}}\times\mathbf{k})k^{-2} \tag{2.12c}$$

$$\dot{\omega} = \partial\Omega/\partial t \tag{2.12d}$$

represent the rates of change of the position and propagation direction of a wave packet. Equation (2.11) is the basic transport equation which we will use in the numerical wave prediction model. The remainder of this chapter is devoted to a discussion of some of the properties of (2.11). We first discuss some peculiarities of (2.11) for the infinite depth case in the absence of currents and next we consider the special cases of shoaling and refraction due to bottom topography and currents.

2.2 PROPERTIES OF THE BASIC TRANSPORT EQUATION

2.2.1 Great circle propagation on the globe

From (2.12a)–(2.12d) we infer that in spherical coordinates the flow is not divergence-free. Considering the case of no depth refraction and no explicit time dependence, the divergence of the flow becomes

$$\frac{\partial}{\partial\phi}\dot{\phi} + \frac{\partial}{\partial\lambda}\dot{\lambda} + \frac{\partial}{\partial\theta}\dot{\theta} + \frac{\partial}{\partial\omega}\dot{\omega} = c_{\mathrm{g}}\cos\theta\tan\phi/R \neq 0 \tag{2.13}$$

which is non-zero because the wave direction, measured with respect to true north, changes while the wave group propagates over the globe along a great circle. As a consequence wave groups propagate along a great circle. This type of refraction is therefore entirely apparent and only related to the choice of coordinate system.

2.2.2 Shoaling

Now discuss finite depth effects in the absence of currents by considering some simple topographies. We first discuss shoaling of waves for the case of wave propagation parallel to the direction of the depth gradient. In this case, depth refraction does not contribute to the rate of change of wave direction $\dot{\theta}$ because, with (2.3b), $\mathbf{k} \times \dot{\mathbf{k}} = 0$. In addition, we take the wave direction θ to be zero so that the longitude is constant ($\dot{\lambda} = 0$) and $\dot{\theta} = 0$. For time-independent topography (hence $\partial\Omega/\partial t = 0$) the transport equation becomes

$$\frac{\partial}{\partial t}N + (\cos\phi)^{-1}\frac{\partial}{\partial\phi}(\dot{\phi}\cos\phi N) = 0 \tag{2.14}$$

where

$$\dot{\phi} = c_{\mathrm{g}}\cos\theta R^{-1} = c_{\mathrm{g}}/R \tag{2.15}$$

and the group speed only depends on latitude ϕ. Restricting our attention to steady waves we immediately find conservation of the action density flux in the latitude direction so that

$$\frac{c_{\mathrm{g}}\cos\phi}{R}N = \mathrm{const} \tag{2.16}$$

If, in addition, it is assumed that the variation of depth with latitude occurs on a much shorter scale than the variation of $\cos\phi$, the latter term may be taken constant for present purposes. It is then found that the action density is inversely proportional to the group speed c_{g} so

$$N \sim 1/c_{\mathrm{g}} \tag{2.17}$$

and if the depth is decreasing for increasing latitude, conservation of flux requires an increase of the action density as the group speed decreases for decreasing depth. This phenomenon, which occurs in coastal areas, is called shoaling. Its most dramatic consequences may be seen when tidal waves, generated by earthquakes, approach the coast resulting in tsunamis. It should be emphasized though, that in the final stages of a tsunami the kinetic description of waves, as presented here, breaks down because of strong nonlinearity.

2.2.3 Refraction

The second example of finite depth effects that we consider is refraction. We again assume no current and a time-independent topography. In the steady state the action balance equation becomes

$$(\cos\phi)^{-1}\frac{\partial}{\partial\phi}\left(\frac{c_{\mathrm{g}}}{R}\cos\theta\cos\phi N\right) + \frac{\partial}{\partial\lambda}\left(\frac{c_{\mathrm{g}}\sin\theta}{R\cos\phi}N\right) + \frac{\partial}{\partial\theta}(\dot{\theta}_{\mathrm{o}}N) = 0 \tag{2.18}$$

where

$$\dot{\theta}_{\mathrm{o}} = \left(\sin\theta \frac{\partial}{\partial\phi}\Omega - \frac{\cos\theta}{\cos\phi}\frac{\partial}{\partial\lambda}\Omega \right)(kR)^{-1} \tag{2.19}$$

In principle, (2.18) can be solved by means of the method of characteristics. The details of this are not given, but we would like to point out the role of the $\dot{\theta}_{\mathrm{o}}$ term for the simple case of waves propagating along the shore. Consider, therefore, waves propagating in a northerly direction (hence $\theta = 0$) parallel to the coast. Suppose that the depth only depends on longitude such that it decreases towards the shore. The rate of change of wave direction is then positive as

$$\dot{\theta}_{\mathrm{o}} = -\frac{1}{kR\cos\phi}\frac{\partial}{\partial\lambda}\Omega > 0 \tag{2.20}$$

since $\partial\Omega/\partial\lambda < 0$. Therefore, waves which are propagating initially parallel to the coast will turn towards the coast. This illustrates that, in general, wave rays will bend towards shallower water resulting in, for example, focusing phenomena and caustics. In this way a sea mountain plays a similar role for gravity waves as a lens for light waves.

2.2.4 Current effects

Finally, we consider some current effects on wave evolution. First of all, a horizontal shear may result in wave refraction; the rate of change of wave direction follows from (2.18) by taking the current into account

$$\dot{\theta}_{\mathrm{c}} = \frac{1}{R}\left(\sin\theta\left[\cos\theta\frac{\partial}{\partial\phi}U_{\phi} + \sin\theta\frac{\partial}{\partial\phi}U_{\lambda}\right] - \frac{\cos\theta}{\cos\phi}\left[\cos\theta\frac{\partial}{\partial\lambda}U_{\phi} + \sin\theta\frac{\partial}{\partial\lambda}U_{\lambda}\right] \right) \tag{2.21}$$

where U_{ϕ} and U_{λ} are the components of the water current in latitudinal and longitudinal directions. Considering the same example as in the case of depth refraction, we note that the rate of change of the direction of waves propagating initially along the shore is given by

$$\dot{\theta}_{\mathrm{c}} = -\frac{1}{R\cos\phi}\frac{\partial}{\partial\lambda}U_{\phi} \tag{2.22}$$

which is positive for an along-shore current which decreases towards the coast. In that event the waves will turn towards the shore.

The most dramatic effects may be found when the waves propagate against the current. For sufficiently large current, wave propagation is prohibited and wave reflection occurs. This may be seen as follows. Consider waves propagating to the right against a slowly varying current U_{o}. At $x \to -\infty$ the current vanishes, decreasing monotonically to some negative value for $x \to +\infty$. Let us generate at $x \to -\infty$ a wave with a certain frequency value Ω_0. Following the waves, we know from (2.8) that for time-independent circumstances the angular frequency of the waves is constant, hence for increasing strength of the current the wavenumber increases as well. Now, whether the surface wave will arrive at $x \to +\infty$ or not depends on the magnitude of the dimensionless frequency $\Omega_0 U_{\mathrm{m}}/g$ (where U_{m} is the maximum strength of the current); for $\Omega_0 U_{\mathrm{m}}/g < 1/4$ propagation up to $x \to +\infty$ is possible, whereas in the opposite case propagation is prohibited. Considering deep water waves only, the dispersion relation reads

$$\Omega = \sqrt{gk} - kU_{\mathrm{o}} \tag{2.23}$$

and the group velocity $\partial\Omega/\partial k$ vanishes for $k = g/4U_{\mathrm{o}}^2$ so that the value of Ω at the extremum is $\Omega_{\mathrm{c}} = g/4U_{\mathrm{o}}$. At the location where the current has maximum strength the critical angular frequency Ω_{c} is the smallest. Let us denote this minimum value of Ω_{c} by $\Omega_{\mathrm{c,min}}(= g/4U_{\mathrm{m}})$. If now the oscillation frequency $\Omega_0 < \Omega_{\mathrm{c,min}}$ is in the entire domain of consideration, then the group speed is always finite and propagation is possible (this of course corresponds to the condition $\Omega_0 U_{\mathrm{m}}/g < 1/4$), but in the opposite case propagation is prohibited beyond a certain point in the domain. What actually happens at that critical point is still under debate. Because of the vanishing group velocity, a large increase of energy at that location may be expected suggesting that wave breaking plays a role. On the other hand, it may be argued that near such a critical point the usual geometrical optics approximation breaks down and that tunnelling and wave reflection occurs (Shyu and Phillips, 1990). A kinetic description of waves which is based on geometrical optics then breaks down as well. This problem is not solved in the WAM model. In order to avoid problems with singularities and non-uniqueness (note that for finite Ω_{c} one frequency Ω corresponds to two wavenumbers) we merely transform to the intrinsic frequency σ (instead of frequency Ω) because a unique relation between σ and wavenumber k exists.

2.3 CONCLUDING REMARK

Note that a global third generation wave model solves the action balance equation in spherical coordinates. By combining previous results of this chapter, the action balance equation becomes

$$\frac{\partial}{\partial t}N + (\cos\phi)^{-1}\frac{\partial}{\partial\phi}(\dot{\phi}\cos\phi N) + \frac{\partial}{\partial\lambda}(\dot{\lambda}N) + \frac{\partial}{\partial\omega}(\dot{\omega}N) + \frac{\partial}{\partial\theta}(\dot{\theta}N) = S \tag{2.24}$$

where

$$\dot{\phi} = (c_{\mathrm{g}}\cos\theta - \mathbf{U}|_{\mathsf{north}})R^{-1} \tag{2.25a}$$

$$\dot{\lambda} = (c_{\mathrm{g}}\sin\theta - \mathbf{U}|_{\mathsf{east}})(R\cos\phi)^{-1} \tag{2.25b}$$

$$\dot{\theta} = c_{\mathrm{g}}\sin\theta\tan\phi R^{-1} + \dot{\theta}_{\mathrm{D}} \tag{2.25c}$$

$$\dot{\omega} = \partial\Omega/\partial t \tag{2.25d}$$

and

$$\dot{\theta}_{\mathrm{D}} = \left(\sin\theta\frac{\partial}{\partial\phi}\Omega - \frac{\cos\theta}{\cos\phi}\frac{\partial}{\partial\lambda}\Omega\right)(kR)^{-1} \tag{2.26}$$

and Ω is the dispersion relation given in (2.4). Before discussing possible numerical schemes to approximate the left-hand side of (2.24) we shall first discuss the parametrization of the source term S, where S is given by

$$S = S_{\mathrm{in}} + S_{\mathrm{nl}} + S_{\mathrm{ds}} + S_{\mathrm{bot}} \tag{2.27}$$

These terms represent the physics of wind input, wave–wave interactions, dissipation due to whitecapping, and bottom friction.

Chapter 3

Parametrization of source terms

Table of contents

In this chapter we will be faced with the task of providing an efficient parametrization of the source terms as they were introduced in Komen *et al.* (1994).

3.1   INTRODUCTION

The need for a parametrization is evident when it is realized that both the exact versions of the nonlinear source term and the wind input require, per grid point, a considerable amount of computation time, say 10 seconds, on the fastest computer that is presently available. In practice, a typical one day forecast should be completed in a time span of the order of two minutes, so it is clear that compromises have to be made regarding the functional form of the source terms in the action balance equation. Even optimization of the code representing the source terms by taking as most inner do-loop, a loop over the number of grid points (thus taking optimal advantage of vectorization) is not of much help here as the gain in efficiency is at most a factor of 10 and as practical applications usually require several thousands of grid points or more. Furthermore, although modern machines have parallel capabilities which result in a considerable speed up, there has been a tendency to use this additional computation power for increases in spatial resolution, and angular and frequency resolution rather then introducing more elaborate parametrizations of the source terms. The present version of the ECMWF wave prediction system has a spatial resolution of 28 km while the spectrum is discretized with 36 directions and 36 frequencies.

In Section 3.2 we discuss a parametrization of wind input and dissipation while Section 3.3 is devoted to a discrete-interaction operator parametrization of the nonlinear interactions. The adequacy of the approximation for wind input and nonlinear transfer is discussed as well. Finally, in Section 3.4 in which we study the energy balance equation in growing wind sea, the relative importance of the physics source terms will be addressed.

3.2   WIND INPUT AND WHITECAP DISSIPATION

3.2.1   Before CY46R1 (iphys=0), before June 2019

The following section describes the parameterisation used until the operational implementation of CY46R1. This option is still available as namelist variable iphys=0.

(a)   *Wind input*

Results of the numerical solution of the momentum balance of air flow over growing surface gravity waves have been presented in a series of studies by Janssen (1989), Janssen *et al.* (1989b) and Janssen (1991). The main conclusion was that the growth rate of the waves generated by wind depends on the ratio of friction velocity and phase speed and on a number of additional factors, such as the atmospheric density stratification, wind gustiness and wave age. So far systematic investigations of the impact of the first additional two effects have not been made, except by Janssen and Komen (1985) and Voorrips *et al.* (1994). It is known that stratification effects observed in fetch-limited wave growth can be partly accounted for by scaling with u_* (which is consistent with theoretical results). The remaining effect is still poorly understood, and is therefore ignored in the standard WAM model. In this section we focus on the dependence of wave growth on wave age, and the related dependence of the aerodynamic drag on the sea state (the effect of which is fully included in the WAM model).

A realistic parametrization of the interaction between wind and wave was given by Janssen (1991), a summary of which is given below. The basic assumption Janssen (1991) made, which was corroborated by his numerical results of 1989, was that even for young wind sea the wind profile has a logarithmic shape, though with a roughness length that depends on the wave-induced stress. As shown by Miles (1957), the growth rate of gravity waves due to wind then only depends on two parameters, namely

$$x = \left(\frac{u_*}{c}\right) \max(\cos(\theta - \phi), 0), \quad (**) \tag{3.1}$$

and

$$\Omega_{\mathrm{m}} = g\kappa^2 z_{\mathrm{o}}/u_*^2 \tag{3.2}$$

As usual, u_* denotes the friction velocity, c the phase speed of the waves, ϕ the wind direction and θ the direction in which the waves propagate. The so-called profile parameter Ω_{m} characterizes the state of the mean air flow through its dependence on the roughness length z_{o}. Thus, through Ω_{m} the growth rate depends on the roughness of the air flow, which, in its turn, depends on the sea state. A simple parametrization of the growth rate of the waves follows from a fit of numerical results presented in Janssen (1991). One finds

$$\frac{\gamma}{\omega} = \epsilon\beta x^2 \tag{3.3}$$

where γ is the growth rate, ω the angular frequency, ϵ the air–water density ratio and β the so-called Miles' parameter. In terms of the dimensionless critical height $\mu = kz_{\mathrm{c}}$ (with k the wavenumber and z_{c} the critical height defined by $U_{\mathrm{o}}(z = z_{\mathrm{c}}) = c$) the Miles' parameter becomes as recently extended to any water depth h.

$$\beta = \frac{\beta_{\mathrm{m}}}{\kappa^2} \tanh(kh)\mu \ln^4(\mu), \quad \mu \le 1 \tag{3.4}$$

where κ is the von Kármán constant and β_{m} a constant. In terms of wave and wind quantities μ is given as

$$\mu = \frac{1}{\kappa^2}\left(\frac{u_*}{c}\right)^2 \tanh(kh)\Omega_{\mathrm{m}} \exp(\kappa/\hat{x}), \quad (**) \tag{3.5}$$

$$\hat{x} = ((u_*/c) + z_\alpha)\cos(\theta - \phi) \tag{3.6}$$

with z_α the wave age tuning parameter.

The input source term S_{in} of the WAM model is then given by

$$S_{\mathrm{in}} = \gamma N \tag{3.7}$$

where γ follows from (3.3) and N is the action density spectrum.

(**) NOTE: It turns out that even though (3.1) and (3.5) are formulated in term of (u_*/c), in the WAM code, $((u_*/c) + z_\alpha)$ has been used instead. This is also the case in the code of WaveWatch 3. Reverting

to using (u_*/c) will require a retuning. For this option (iphys=0), this has not been done, but for the new iphys=1 option, this was done (see section below).

The stress of air flow over sea waves depends on the sea state and from a consideration of the momentum balance of air it is found that the kinematic stress is given as (Janssen, 1991)

$$u_*^2 = \tau = (\kappa U(z_{\mathrm{obs}})/ \ln(z_{\mathrm{obs}}/z_{\mathrm{o}}))^2 \tag{3.8}$$

where

$$z_{\mathrm{o}} = \hat{\alpha}\tau/g\sqrt{1-y}, \quad y = \tau_{\mathrm{w}}/\tau \tag{3.9}$$

Here z_{obs} is the mean height above the waves (currently 10m) and τ_{w} is the stress induced by gravity waves (the "wave stress")

$$\tau_{\mathrm{w}} = \epsilon^{-1}g \int \mathrm{d}\omega \, \mathrm{d}\theta \, \gamma N \mathbf{k} \tag{3.10}$$

The frequency integral extends to infinity, but in its evaluation only an f^{-5} tail of gravity waves is included (see Chapter 5 for details on how the high frequency contribution is computed) and the higher level of capillary waves is treated as a background small-scale roughness. In practice, we note that the wave stress points in the wind direction as it is mainly determined by the high-frequency waves which respond quickly to changes in the wind direction. Note that (3.8) with (3.9) and (3.10) is solved for u_* using an iterative Newton-Raphson scheme. Until CY45R1, it used to be tabulated in pre-computed look-up table as a function of $U(z_{\mathrm{obs}})$, τ_{w} and the dynamic cut-off frequency ((see Chapter 5). With CY45R1, it is now computed efficiently every time using the same iterative scheme.

The relevance of relation (3.9) cannot be overemphasized. It shows that the roughness length is given by a Charnock relation (Charnock, 1955)

$$z_{\mathrm{o}} = \alpha\tau/g \tag{3.11}$$

However, the dimensionless Charnock parameter α is not constant but depends on the sea state through the wave-induced stress since

$$\alpha = \hat{\alpha}/\sqrt{1 - \frac{\tau_{\mathrm{w}}}{\tau}} \tag{3.12}$$

Evidently, whenever τ_{w} becomes of the order of the total stress in the surface layer (this happens, for example, for young wind sea) a considerable enhancement of the Charnock parameter is found, resulting in an efficient momentum transfer from air to water. The consequences of this sea-state-dependent momentum transfer is discussed in Chapter 7. Note that z_{o} is not capped by any maximum value.

This finally leaves us with the choice of three unknowns namely $\hat{\alpha}$ from (3.12), β_{m} from (3.4) and z_{α} from (3.5). Until CY47R1, $\hat{\alpha}$ was a tunable constant that was chosen in such a way that for old wind sea the Charnock parameter α has the mean value 0.0165 in agreement with observations collected by Wu (1982) on the drag over sea waves. It should be realized though, that the determination of $\hat{\alpha}$ is not a trivial task, as beforehand the ratio of wave-induced stress to total stress is simply not known. It requires the running of a wave model. Since CY47R1, it was realised that the Charnock parameter should reduce quite considerably under strong tropical winds (above 33 m/s). This was achieved by making $\hat{\alpha}$ a function of 10m wind speed U_{10}
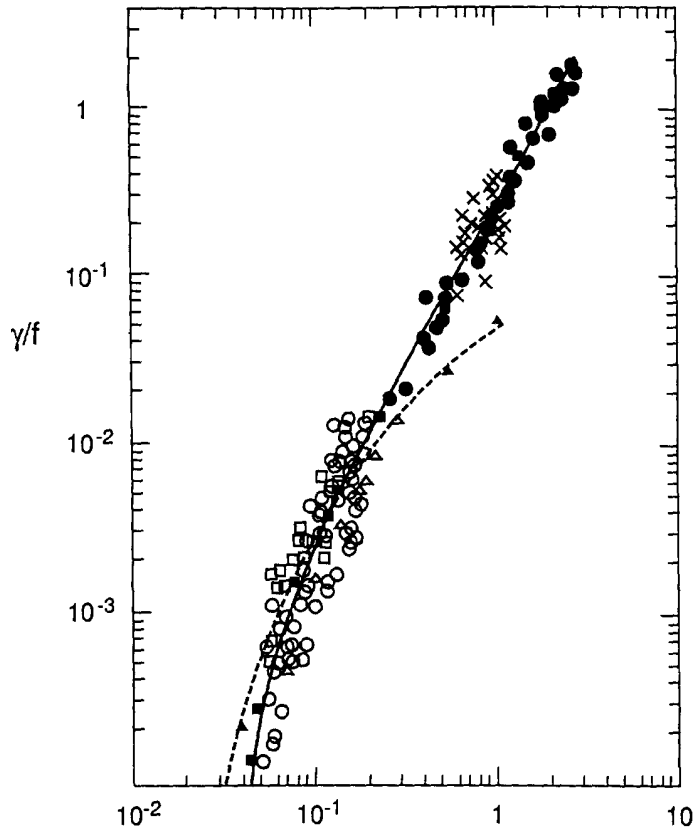
$$\hat{\alpha} = \hat{\alpha}_{min} + 0.5(\hat{\alpha}_o - \hat{\alpha}_{min})[1 - \tanh(U_{10} - 33)] \tag{3.13}$$

The values for $\hat{\alpha}$ were found by trial and error (see (3.23)).

The constant β_{m} is chosen in such a way that the growth rate γ in (3.3) is in agreement with the numerical results obtained from Miles' growth rate. For $\beta_{\mathrm{m}} = 1.2$, $z_{\alpha} = 0.011$ and a Charnock parameter $\alpha = 0.0144$ we have shown in Fig. 3.1 the comparison between Miles' theory and (3.3). In addition observations as compiled by Plant (1982) are shown. Realizing that the relative growth rate γ/f varies by four orders of magnitude it is concluded that there is a fair agreement between our fit (3.3), Miles' theory and observations. We remark that the Snyder et al. (1981) fit to their field observations, which is also shown in Fig. 3.1, is in perfect accordance with the growth rate of the low-frequency waves although growth rates of the high-frequency

waves are underestimated. Since the wave-induced stress is mainly carried by the high-frequency waves an underestimation of the stress in the surface layer would result.

Note however that since CY38R1, z_α was reduced to 0.008 (from 0.011). The reduction was motivated by the known tendency of the model to generate too much waves at low frequencies. As seen in Fig. 3.2, the new value of z_α reduces the wind input of long waves. The whitecap dissipation source function was adapted accordingly as described below. Note that this small adjustment of z_α still fits the observational data used by Janssen to develop his formulation (Janssen (1991)).
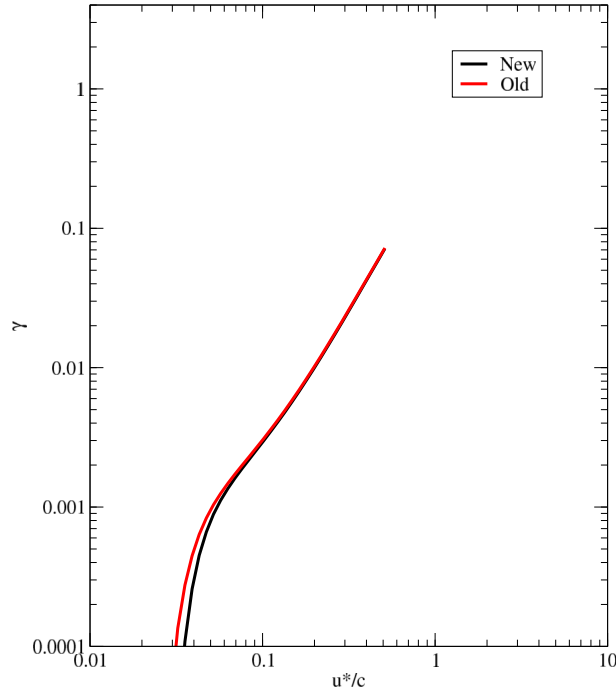

Figure 3.1 *Comparison of theoretical growth rates with observations compiled by Plant (1982). Full line: Miles' theory; full squares: parametrization of Miles' theory (3.3); dashed line: the fit by Snyder et al. (1981). ($\beta_m = 1.2$, $z_\alpha = 0.011$ and $\alpha = 0.0144$)*

We conclude that our parametrization of the growth rate of the waves is in good agreement with the observations. The next issue to be considered is how well our approximation of the surface stress compares with observed surface stress at sea. Fortunately, during HEXOS (Katsaros *et al.*, 1987) the wind speed at 10 m height, U_{10}, surface stress τ and the one-dimensional frequency spectrum were measured simultaneously so that our parametrization of the surface stress may be verified experimentally. For a given observed wind speed and wave spectrum, the surface stress is obtained by solving (3.8) for the stress τ in an iterative fashion as the roughness length z_o depends, in a complicated manner, on the stress. Since the surface stress was measured by means of the eddy correlation technique, a direct comparison between observed and modelled stress is possible. The work of Janssen (1992) shows that the agreement is good.

It is concluded that the parametrized version of quasi-linear theory gives realistic growth rates of the waves and a realistic surface stress. However, the success of this scheme for wind input critically depends on a proper description of the high-frequency waves. The reason for this is that the wave-induced stress depends in a sensitive manner on the high-frequency part of the spectrum. Noting that for high frequencies the growth rate of the waves (3.3) scales with wavenumber as

$$\gamma \sim k^{3/2} \tag{3.14}$$

Figure 3.2 *Non dimensional growth rate γ/f for a Charnock parameter $\alpha = 0.0144$. New (black) is for $z_\alpha = 0.008$ and old (red) for $z_\alpha = 0.011$.*

and the usual whitecapping dissipation scales as

$$\gamma_{\mathrm{d}} \sim k \tag{3.15}$$

an imbalance in the high-frequency wave spectrum may be anticipated. Eventually, wind input will dominate dissipation due to wave breaking, resulting in energy levels which are too high when compared with observations.

(b)   Whitecap dissipation

Janssen *et al.* (1989a) realized that the wave dissipation source function has to be adjusted in order to obtain a proper balance at the high frequencies. The dissipation source term of Hasselmann (1974) is thus extended as

$$S_{\mathrm{ds}} = -C_{\mathrm{ds}}\langle\omega\rangle(\langle k\rangle^2 m_0)^2[(1-\delta)k/\langle k\rangle + \delta(k/\langle k\rangle)^2]N \tag{3.16}$$

where C_{ds} and δ are constants, m_0 is the total wave variance per square metre, k the wavenumber, and $\langle\omega\rangle$ and $\langle k\rangle$ are the mean angular frequency and mean wavenumber, respectively. The choice of the above dissipation source term may be justified as follows. In Hasselmann (1974), it is argued that whitecapping is a process that is weak-in-the-mean, therefore the corresponding dissipation source term is linear in the wave spectrum. Assuming that there is a large separation between the length scale of the waves and the whitecaps, the power of the wavenumber in the dissipation term is found to be equal to one. For the high-frequency part of the spectrum, however, such a large gap between waves and whitecaps may not exist, allowing the possibility of a different dependence of the dissipation on wavenumber.

Before Cy29r1, the mean frequency $\langle\omega\rangle$ was defined by means of the inverse mean frequency

$$\langle\omega\rangle = \int d\mathbf{k}\, F(\mathbf{k})/ \int d\mathbf{k}\, F(\mathbf{k})/\omega \tag{3.17}$$

with $F(\mathbf{k})$ the wavenumber spectrum, $\mathbf{k}$ the wavenumber and ω the angular frequency. A similar relation for the mean wavenumber $\langle k\rangle$ is used

$$\sqrt{\langle k\rangle} = \int d\mathbf{k}\, F(\mathbf{k})/ \int d\mathbf{k}\, F(\mathbf{k})/\sqrt{k}. \tag{3.18}$$

Using the discrete interaction approximation (DIA) to the nonlinear transfer, Janssen (see Komen *et al.*, 1994) found optimal results with $\delta = 0.5$ and $C_{ds} = 4.5$.

Upon inspection of (3.17) and (3.18), it is apparent that the mean steepness and mean frequency parameters used in the above parametrization of the dissipation are to a considerable extent determined by the low frequency part of the spectrum (swell) rather than by the windsea part of the spectrum. As discussed in Bidlot *et al.* (2006), this had unwanted consequences when both swell and windsea are present.

Hence, since Cy29r1, the mean wave number $\langle k \rangle$ and mean frequency $\langle \omega \rangle$ are defined using weighted spectral integrals that put more emphasis on the high frequencies. The mean angular frequency $\langle \omega \rangle$ is now defined by means of the first ω-moment of the spectrum

$$\langle \omega \rangle = \int d\mathbf{k} \, \omega F(\mathbf{k}) / \int d\mathbf{k} \, F(\mathbf{k}) \tag{3.19}$$

A similar relation for the mean wavenumber $\langle k \rangle$ is also used

$$\sqrt{\langle k \rangle} = \int d\mathbf{k} \, \sqrt{k} F(\mathbf{k}) / \int d\mathbf{k} \, F(\mathbf{k}) \tag{3.20}$$

This concludes the description of the input source term and the dissipation source term due to whitecapping. Although the wind input source function is fairly well-known from direct observations, there is relatively little hard evidence on dissipation. Presently, the only way out of this is to take the functional form for the dissipation in (3.16) for granted and to tune the constants C_{ds} and δ in such a way that the action balance equation (2.24) produces results which are in good agreement with data on fetch-limited growth and with data on the dependence of the surface stress on wave age. In addition, a reasonable dissipation of swell should be obtained. A tuning exercise was performed in such a way that the duration limited growth curve for significant wave height and the time evolution of the Charnock parameter resembled as much as possible the corresponding results of the previous version of the wave model. As a result we found that

$$C_{ds} = 2.10, \ \delta = 0.6 \text{ and } \hat{\alpha} = 0.0095 \quad \text{before CY38R1,} \tag{3.21}$$

$$C_{ds} = 1.33, \ \delta = 0.5 \text{ and } \hat{\alpha} = 0.0060 \quad \text{since CY38R1 until CY46R1,} \tag{3.22}$$

$$C_{ds} = 1.33, \ \delta = 0.5 \text{ and } \hat{\alpha}_o = 0.0060; \ \hat{\alpha}_{min} = 0.0001 \quad \text{since CY47R1.} \tag{3.23}$$

3.2.2 Since CY46R1 (iphys=1), June 2019

The parameterisations for input and whitecap dissipation of (Ardhuin *et al.*, 2010) have been implemented in WAM. Besides the actual selection of the different parameters, a few changes were made as indicated in the following section.

(a)   Wind input

The wind input is an adapted version of the previous parametrisation (iphys=0), but as justified by (Ardhuin *et al.*, 2010), it is reduced at high frequency to allow a better balance with the new saturation based dissipation (next section). It is achieved by replacing the friction velocity u_* used in (3.1) to (3.6) by a wave number dependent $u_*'(k)$ defined by

$$u_*'^2 = u_*^2 (\cos(\phi), \sin(\phi)) - tauwshelter \quad \epsilon^{-1} g \int_0^{2\pi} \int_0^k d\omega d\theta \, \frac{k}{\omega} S_{in}(\cos(\theta), \sin(\theta)) \tag{3.24}$$

where the sheltering coefficient *tauwshelter* can be used to tune the wind stresses. This sheltering coefficient is also applied to the diagnostic tail ((see Chapter 5).

Also in this case, (3.1) and (3.5) are formulated in term of (u_*/c). This was not the case in the code of WaveWatch 3 (see sub section (a) of 3.2).

Following tuning exercises, the following values were selected

$$tauwshelter = 0.25, \ \beta_m = 1.42, \ z_\alpha = 0.008 \text{ and } \hat{\alpha} = 0.0062 \quad \text{in CY46R1.} \tag{3.25}$$

$$tauwshelter = 0.25, \ \beta_m = 1.40, \ z_\alpha = 0.008 \text{ and } \hat{\alpha}_o = 0.0065; \ \hat{\alpha}_{min} = 0.0001 \quad \text{since CY47R1.} \tag{3.26}$$

(b) *Whitecap dissipation*

The whitecap dissipation formulation of (Ardhuin *et al.*, 2010) has been implemented. However, it was found that the cumulative breaking term was extremely expensive (roughly doubling the computation time), and yet, it did not produce any significant difference on a global scale (cm differences in mean significant wave heights), provided that a high frequency diagnostic tail is specified (see Chapter 5). It was decided to not compute the cumulative breaking term by setting SSDSC3 to 0. All other coefficients are set to the values used by WaveWatch3, ST4, TEST471.

3.2.3   Wind gustiness and air density

The input source term given in (3.7) and (3.3) assumes homogeneous and steady wind velocity within a model grid-box and during a time-step. Assuming that the wind speed variations with scales much larger than both the spatial resolution and the time step are already resolved by the atmospheric model, we need to include the impact of the wind variability at scales comparable to or lower than the model resolution (which is called wind gustiness). To achieve this, an enhanced input source term with the mean impact of gustiness can be estimated as

$$\bar{\gamma}(u_*) = \frac{1}{\sigma_* \sqrt{2\pi}} \int_{-\infty}^{\infty} \exp\left\{ -\frac{(u_* - \bar{u}_*)^2}{2\sigma_*^2} \right\} \gamma(u_*) \mathrm{d}u_* \tag{3.27}$$

where u_* represents the instantaneous (unresolved) wind friction velocity, σ_* is the standard deviation of the friction velocity and the over-barred quantity represents the mean value of the quantity over the whole grid-box/time-step. Note that this is the (gust-free) value obtained from the atmospheric model. The integral above can be approximated using the Gauss-Hermite quadrature as

$$\bar{\gamma}(u_*) = 0.5 \left[\gamma(\bar{u}_* + \sigma_*) + \gamma(\bar{u}_* - \sigma_*) \right] \tag{3.28}$$

The magnitude of variability can be represented by the standard deviation of the wind speed. To estimate the standard deviation value, one can use the empirical expression proposed by Panofsky *et al.* (1977) which can be written as

$$\frac{\sigma_{10}}{u_*} = \left\{ b_{\mathrm{g}} + \frac{1}{2} \left(\frac{z_i}{-L} \right) \right\}^{1/3} \tag{3.29}$$

where σ_{10} is the standard deviation of the 10 m wind speed (U_10), z_i is the height of the lowest inversion, L is the Monin-Obukhov length, and b_{g} is a constant representing the background gustiness level that exists at all times irrespective of the stability conditions. The quantity z_i/L, which is a measure for the atmospheric stability, is readily available from the atmospheric model. In order to use (3.29) to derive σ_*, we use the following expression for the drag coefficient C_{d} in terms of 10m wind speed U_{10} based on the paper by Edson *et al.* (2013) and corrigendum Edson *et al.* (2014)

$$u_* = \sqrt{C_{\mathrm{d}}} \, U_{10} \tag{3.30}$$

$$C_{\mathrm{d}} = (c_1 + c_2 \, U_{10}^{p_1})^{p_2}, \quad c_1 = 1.03 \, 10^{-3}, \quad c_2 = 0.04 \, 10^{-3}, \quad p_1 = 1.48, \quad p_2 = -0.21 \tag{3.31}$$

which yields

$$\frac{\sigma_*}{u_*} = \frac{1}{U_{10}} \left\{ 1 + \frac{0.5 \, U_{10}}{C_{\mathrm{d}}} \left(p_2 c_1 + (p_1 + p_2) \, c_2 \, U_{10}^{p_1}) U_{10}^{(p_2-1)} \right) \right\} \left\{ b_g \, u_*^3 + \frac{1}{2} \, \kappa \, w_*^3) \right\}^{1/3} \tag{3.32}$$

where w_* is the free convection velocity scale which is obtained from the atmospheric model

$$w_* = u_* \left\{ \frac{1}{\kappa} \left(\frac{z_i}{-L} \right) \right\}^{1/3} \quad for \; L < 0 \quad and \quad w_* = 0 \quad for \; L >= 0 \tag{3.33}$$

Note that the impact of the background level of gustiness is assumed to be implicitly included in the parametrisations of the atmospheric model as well as in the wave model. Therefore, b_{g} is set to 0 (Abdalla and Bidlot, 2002). Note that we also limit 3.32 to a maximum of 0.1.

The growth rate of waves is proportional to the ratio of air to water density, ϵ, as can be seen in (3.3). Under normal conditions, seawater density varies within a very narrow range and, therefore, it can be assumed to be constant. On the other hand, air density has a wider variability and needs to be evaluated for better wave predictions. Based on basic thermodynamic concepts, it is possible to compute the air density using the formula

$$\rho_{air} = \frac{P}{RT_v} \tag{3.34}$$

where P is the atmospheric pressure, $R \simeq 287.04 \, \mathrm{J \, kg^{-1} \, K^{-1}}$ is a constant defined as $R = R_+/m_a$, with R_+ the universal gas constant $(R_+ \simeq 8314.36 \, \mathrm{J \, kmol^{-1} \, K^{-1}})$ and m_a is the molecular weight of the dry air $(\simeq 28.966 \, \mathrm{kg \, kmol^{-1}})$, and T_v is the virtual temperature. The virtual temperature can be related to the actual air temperature, T, and the specific humidity, q, by: $T_v \simeq (1 + 0.6078q)T$ (Abdalla and Bidlot, 2002). To avoid using diagnostic variables , the pressure, the temperature and humidity at the lowest model level are now used.

3.2.4   Use of neutral winds

As follows from the expression of the growth rate of waves by wind, the WAM model is based on friction velocity scaling. Therefore, the friction velocity u_* is required. In the practice of ocean wave modelling the friction velocity is not available, but surface winds at 10m height are available. In the original version of the WAM model the friction velocity was then obtained by assuming that the relation between u_* and the wind speed at a given height is given by the logarithmic profile. This assumes neutral stable conditions, which is only approximately correct. A proper solution is to transform the surface winds into their neutral wind counterparts. In the coupled IFS/WAM system, this transformation can easily be achieved on the IFS side by using the atmospheric surface stress and the logarithmic wind profile with the roughness length based on the Charnock parameter (Fig. 3.3). See 10.4.1 for more details on how the 10m neutral winds are computed for ECWAM.
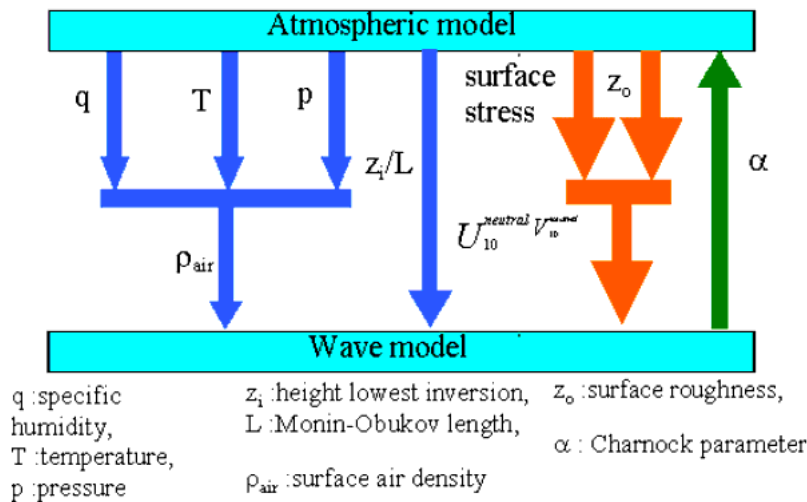

Figure 3.3 *Schematic representation of the interface between the IFS and WAM.*

3.2.5   Surface Stokes drift

The IFS has a scheme to model the warm layer over the ocean. Following Takaya *et al.* (2010), the scheme has been extended to account for the impact of Langmuir mixing on the upper ocean heat balance. For this reason, the two components of the surface Stokes drift are returned since CY36R4 to the atmospheric model along side the Charnock parameter. The surface Stokes drift components are also an output parameter of the model as given by (10.23).

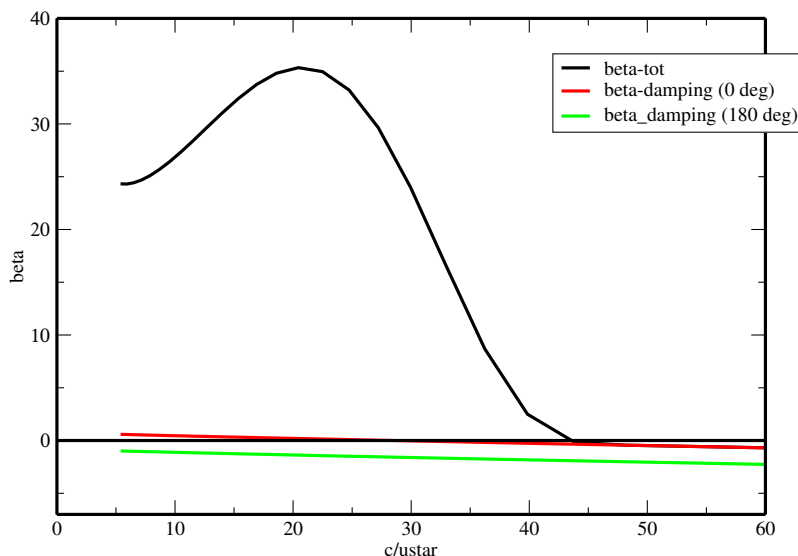### 3.2.6 Damping of long waves

(a) *with iphys=0*

The Miles critical layer theory is, to some extent, an idealization of reality because effects of turbulent eddies on wave growth have not been taken into account. The first attempts to include effects of turbulence were based on the classical eddy viscosity model, however, typically too large damping rates of the long waves were found: for 15 seconds waves spatial damping scales are of the order of 75 km, with the consequences that no swells would arrive in the Tropics generated by storms in the extra-Tropics.

The classical eddy viscosity model is based on the assumption that air-turbulence is the fastest process, much faster than the typical period of the ocean waves. This assumption is however not valid for swells which have propagation speeds that are much faster than a typical wind speed scale $V = U(z = L)$ where $L = 1/k$ with k the wavenumber. In those circumstances momentum transport by turbulent eddies is much less effective. A more quantitative discussion of the truncation of transport by turbulent eddies is given in Janssen (2004). An asymptotic analysis of the resulting boundary value problem (i.e. including the small effects of turbulent eddies) then allows to obtain the following expression for the relative growth rate γ/ω

$$\frac{\gamma}{\omega} = \epsilon \tanh{(kh)} \left\{ \beta x^2 + 2\kappa \left(\frac{u_*}{c} \right)^2 \left(\cos(\theta - \phi) - \frac{c}{V} \right) \right\}. \tag{3.35}$$

NOTE: It turns out that even though (3.35) is formulated in term of (u_*/c), in the WAM code, $((u_*/c)+ z_\alpha)$ was used instead.

The first term on the right-hand side then corresponds to the Miles critical layer effect (cf. Eq. 3.4) while the second term gives a normally small correction to the growth rate due to air turbulence. Nevertheless this small correction gives important effects for swells propagating over large distances as happens e.g. for ocean waves generated by extra-tropical storms which propagate towards the East Tropical Pacific. Typical damping scales according to 3.35 are of the order of thousands of kilometers. For waves propagating with the wind a plot of the Miles parameter β as function of the dimensionless phase speed c/u_* is given in Fig. 3.4. In order to appreciate the effects of growth/damping due to air turbulence the second term of Eq. (3.35) is plotted separately for two different wave propagation angles namely, with and against the wind. The plot shows that when $c > V \cos(\theta - \phi)$ the waves are damped, but, clearly, compared to the growth rate of the short waves the damping rates are small.

Figure 3.4 *The Miles parameter $\beta = \gamma/\epsilon\omega x^2$ as function of c/u_* for waves propagating in the wind direction. The effect of air turbulence for different propagation direction is shown as well.*

Experiments with the inclusion of the weak damping term over a one-year period have shown that there are beneficial reductions of the systematic wave height error and the standard deviation of error (as measured against Altimeter wave height data) in the Tropical areas of the East Pacific, the Tropical Atlantic and the Eastern Part of the Indian Ocean.

When swell is the dominant feature of the sea state, the weak damping term may give rise to a reduction of the wave-induced stress τ_w as defined in Eq. 3.10, hence resulting in a reduction of the roughness length of the logarithmic wind profile. This is of course just a reflection of the fact that when waves are propagating faster than the wind then there is a momentum transfer from waves to wind, thus speeding up the surface wind. However, with the present parametrization of the wave damping, cf. Eq. (3.35), this speed up of the surface wind is small.

(b) *with iphys=1*

The swell dissipation terms of (Ardhuin *et al.*, 2010) have been implemented.

However, it was found that the roughness estimate for the dissipation due to the oscillatory flow was too strong for large wind conditions. This parameterisation takes a small fraction (Z0RAT) of the actual aerodynamical roughness length scale z_o to set the estimate for the roughness seen by the oscillatory flow. Limiting z_o to a value of 0.0005 for that estimate gave slightly better results.

A fixed value of the critical Reynolds number (SWELLF4 = 150000) was selected by setting SWELLF6 to 1 as it was considered that using the wave height dependent fomulation was not really meaningful. Also the limits used in the tabulated friction factor of Grant and Madsen's theory, ABMIN and ABMAX were respectively set to 0.3 and 8.0

All other coefficients are set to the values used by WaveWatch3, ST4, TEST471.

3.2.7   Maximum spectral steepness

It has been reported that the values of the drag coefficient tail off for large winds (Doyle J. and Wang (2012), Holthuijsen and Pietrzak (2012)). In ECWAM, from about 1.3 times the peak frequency the model has an ω^{-4} spectrum which is caused by the nonlinear interactions pumping energy from the low frequency waves to the high frequency waves. In fact, the model spectra take the form of the Toba spectrum in that frequency range.

$$F(\omega) = \alpha_t \, g \, u_* \, \omega^{-4} \tag{3.36}$$

However, clearly for strong winds and hence large u_*, the Toba spectrum cannot hold because the waves in that frequency range become too steep and breaking should happen.

Therefore, the idea is to impose a limitation to the high frequency part of the spectrum based on a limiting Phillips spectrum

$$F_{max}(f) = \alpha_{max} \, g^2 \, (2\pi)^{-4} \, f^{-5} \tag{3.37}$$

which in the two dimensions can be written as

$$F_{max}(f, \theta) = \frac{\alpha_{max}}{\pi} g^2 \, (2\pi)^{-4} \, f^{-5} \tag{3.38}$$

In ECWAM, the limiting Phillips spectrum (3.38) is imposed immediately after the spectral update following the source term integration:

$$F(f, \theta) = min(F(f, \theta), F_{max}(f, \theta)) \tag{3.39}$$

The value of α_{max} is a tuning parameter. By trial and error, a value $\alpha_{max} = 0.03$ was selected for iphys=0 and 0.031 for iphys=1.

This change was implemented in CY43R1 (November 2016). It had a net impact of reducing the drag coefficient for high wind ($> 25m/s$), more in line with estimate of drag in high wind conditions. Note however that the change introduced with CY47R1 on limiting the value of $\hat{\alpha}$ (3.13) had a more pronounce impact on the drag.

3.2.8 Bottom dissipation

Dissipation owing to bottom friction is not discussed here because the details of its parametrization were presented in Komen *et al.* (1994, chapter II) as well as the relative merits of this approach being fully discussed. We merely quote the main result

$$S_{\text{bot}} = -2C_{\text{bot}} \frac{k}{\sinh(2kh)} N \tag{3.40}$$

where the constant $C_{\text{bot}} = 0.038/g$ and h the water depth.

3.3   NONLINEAR TRANSFER

In Komen *et al.* (1994) the derivation of the source function S_{nl}, describing the nonlinear energy transfer, was given from first principles. For surface gravity waves the nonlinear energy transfer is caused by four resonantly interacting waves, obeying the usual resonance conditions for the angular frequency and the wave numbers. Owing to resonant four-wave interactions the rate of change of the action density spectrum $N = gF(\mathbf{k})/\omega$ (where F is the wave variance spectrum) is given by

$$S_{\text{nl}} = 4 \int d\mathbf{k}_{1,2,3} T_{1,2,3,4}^2 \delta(\mathbf{k}_1 + \mathbf{k}_2 - \mathbf{k}_3 - \mathbf{k}_4) R_i(\Delta\omega, t) \left[N_1 N_2 (N_3 + N_4) - N_3 N_4 (N_1 + N_2) \right], \tag{3.41}$$

where for resonant waves $R_i(\Delta\omega, t) = \pi\delta(\omega_1 + \omega_2 - \omega_3 - \omega_4)$ and $T_{1,2,3,4}$ is a known interaction coefficient. The evaluation of S_{nl} therefore requires an enormous amount of computation because a three-dimensional integral needs to be evaluated. In the past several attempts have been made to try to obtain a more economical evaluation of the nonlinear transfer. The approach that was most successful to date is the one by Hasselmann *et al.* (1985). The reason for this is that their parametrization is both fast and it respects the basic properties of the nonlinear transfer, such as conservation of momentum, energy and action, while it also produces the proper high-frequency spectrum.

To this end, Hasselmann *et al.* (1985) constructed a nonlinear interaction operator by considering only a small number of interaction configurations consisting of neighbouring and finite distance interactions. It was found that, in fact, the exact nonlinear transfer could be well simulated by just one mirror-image pair of intermediate range interactions configurations. In each configuration, two wavenumbers were taken as identical $\mathbf{k}_1 = \mathbf{k}_2 = \mathbf{k}$. The wavenumbers $\mathbf{k}_3$ and $\mathbf{k}_4$ are of different magnitude and lie at an angle to the wavenumber $\mathbf{k}$, as required by the resonance conditions. The second configuration is obtained from the first by reflecting the wavenumbers $\mathbf{k}_3$ and $\mathbf{k}_4$ with respect to the $\mathbf{k}$-axis. The scale and direction of the reference wavenumber are allowed to vary continuously in wavenumber space.

The simplified nonlinear operator is computed by applying the same symmetrical integration method as is used to integrate the exact transfer integral (see also Hasselmann and Hasselmann, 1985), except that the integration is taken over a two-dimensional continuum and two discrete interactions instead of five-dimensional interaction phase space. Just as in the exact case the interactions conserve energy, momentum and action.

For the configurations

$$\begin{aligned} \omega_1 &= \omega_2 = \omega \\ \omega_3 &= \omega(1 + \lambda) = \omega_+ \\ \omega_4 &= \omega(1 - \lambda) = \omega_- \end{aligned} \tag{3.42}$$

where $\lambda = 0.25$, satisfactory agreement with the exact computations was achieved. From the resonance conditions the angles θ_3, θ_4 of the wavenumbers $\mathbf{k}_3(\mathbf{k}_+)$ and $\mathbf{k}_4(\mathbf{k}_-)$ relative to $\mathbf{k}$ are found to be $\theta_3 = 11.5°, \theta_4 = -33.6°$.

The discrete interaction approximation has its most simple form for the rate of change in time of the action density in wavenumber space. In agreement with the principle of detailed balance, we have

$$\frac{\partial}{\partial t} \begin{pmatrix} N \\ N_+ \\ N_- \end{pmatrix} = \begin{pmatrix} -2 \\ +1 \\ +1 \end{pmatrix} Cg^{-8} f^{19} [N^2(N_+ + N_-) - 2NN_+N_-] \Delta\mathbf{k} \tag{3.43}$$

where $\partial N/\partial t$, $\partial N_+/\partial t$, $\partial N_-/\partial t$ are the rates of change in action at wavenumbers $\mathbf{k}$, $\mathbf{k}_+$, $\mathbf{k}_-$ due to the discrete interactions within the infinitesimal interaction phase-space element $\Delta\mathbf{k}$ and C is a numerical constant. The net source function S_{nl} is obtained by summing 3.43 over all wavenumbers, directions and interaction configurations.

For a JONSWAP spectrum the approximate and exact transfer source functions have been compared in Komen *et al.* (1994). The nonlinear transfer rates agree reasonably well, except for the strong negative lobe of the discrete-interaction approximation. This feature is, however, less important for a satisfactory reproduction of wave growth than the correct determination of the positive lobe which controls the down shift of the spectral peak.

The usefulness of the discrete-interaction approximation follows from its correct reproduction of the growth curves for growing wind sea. This is shown in Fig. 3.5 where a comparison is given of fetch-limited growth curves for some important spectral parameters computed with the exact nonlinear transfer, or, alternatively, with the discrete-interaction approximation. Evidence of the stronger negative lobe of the discrete interaction approximation is seen through the somewhat smaller values of the Phillips constant α_{p}. The broader spectral shape corresponds with the smaller values of peak enhancement γ for the parametrized case. On the other hand, the agreement of the more important scale parameters, the energy ϵ_* and the peak frequency ν_*, is excellent (note that as always an asterisk denotes non-dimensionalization of a variable through g and the friction velocity u_*).
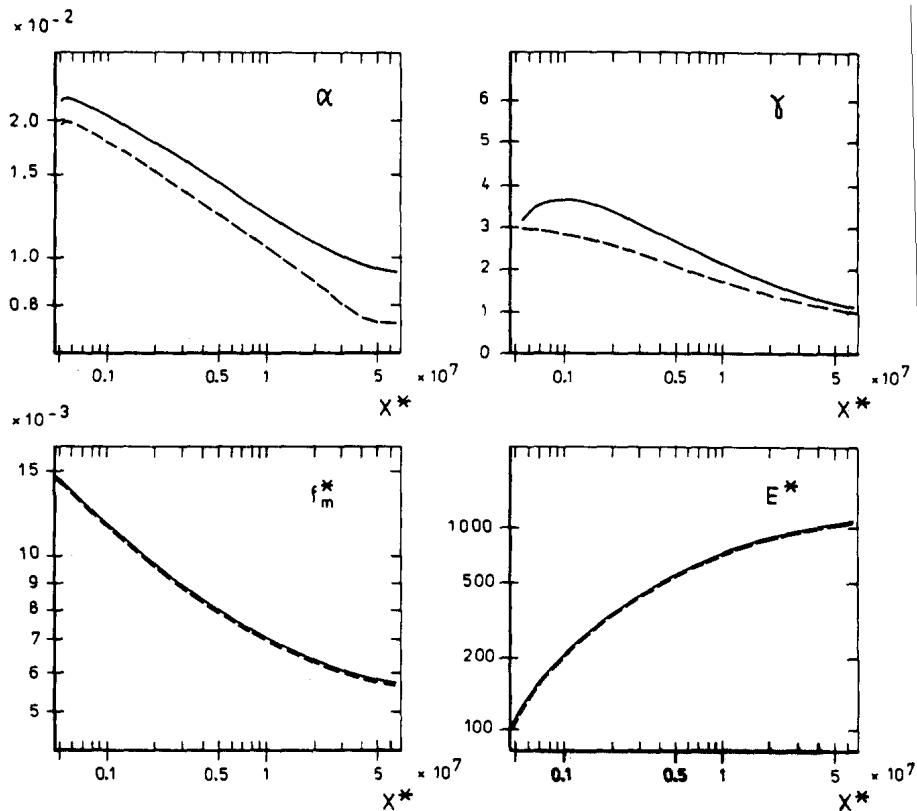

Figure 3.5 *Comparison of fetch-growth curves for spectral parameters computed using the exact form and the discrete interaction approximation of S_{nl}. All variables are made dimensionless using u_* and g.*

The above analysis considered deep water waves only. Finite-amplitude Finite-amplitude deep-water waves are subject to modulational instability which results in a nonlinear energy transfer among the components in the wave spectrum, which eventually can lead to the formation of extreme waves. However, in shallow water, finite-amplitude surface gravity waves generate a current and deviations from the mean surface elevation. This stabilizes the modulational instability, and as a consequence, in a fairly wide range around $kD = 1.363$ the nonlinear transfer becomes small. In addition, while for $kD > 1.363$ there is nonlinear focusing giving the

possibility of the formation of extreme waves, in the opposite case the process of nonlinear focusing ceases to exist. This is a well-known property of surface gravity waves.

Numerical computations by Hasselmann and Hasselmann (1981) of the full Boltzmann integral for water of arbitrary depth have shown that there is an approximate relation between transfer rates in deep water and water of finite depth: for a given frequency-direction spectrum, the transfer for finite depth is identical to the transfer for infinite depth, except for a rescaling factor R :

$$\mathrm{Snl} = R(\bar{k}h)\mathrm{Snl}(deep),\qquad(3.44)$$

where $\bar{k}$ is the mean wavenumber. This rescaling relation holds in the range $\bar{k}h > 1$, where the exact computations could be closely reproduced with the rescaling factor

$$R(x) = 1 + \frac{5.5}{x}\left(1 - \frac{5x}{6}\right)\exp\left(-\frac{5x}{4}\right),\qquad(3.45)$$

with $x = \frac{3}{4}\bar{k}h$. This approximation was used in the original WAM model.

However, Janssen and Onorato (2007) have discussed the consequences of the generation of a wave-induced current for the evolution of the wave spectrum. For wave forecasting purposes the evaluation of the three dimensional integral given in (3.41) is too time consuming and in practice we resort to the Direct-Interaction Approximation (DIA) of Hasselmann *et al.* (1985) described above. In the direct interaction approximation, the strength of the nonlinear interactions is estimated using the narrow-band approximation as given by (3.41). Hence, in DIA the nonlinear interactions scale with the scaling factor S given by

$$S = \frac{k^2 T_{0,0,0,0}^2}{|\omega_0''|},\qquad(3.46)$$

where ω_0'' is the second derivative of angular frequency with respect to carrier wavenumber k. The second derivative stems from the delta-function for the frequencies in the limit of a narrow-band spectrum. For surface gravity waves on water of finite depth D the dispersion relation reads

$$\omega_0 = \sqrt{gk_0 T_0},\ T_0 = \tanh x,\ x = k_0 D,\qquad(3.47)$$

while the first and second derivative become

$$v_g = \omega_0' = \frac{1}{2}c_0\left\{1 + \frac{2x}{\sinh 2x}\right\},\ c_0 = \frac{\omega_0}{k_0},\qquad(3.48)$$

and

$$\omega_0'' = -\frac{g}{4\omega_0 k_0 T_0}\times\Omega'',\qquad(3.49)$$

with

$$\Omega'' = \left\{T_0 - x\left(1 - T_0^2\right)\right\}^2 + 4x^2 T_0^2\left(1 - T_0^2\right).\qquad(3.50)$$

Note that for any value of the depth D the second derivative is always negative. Finally, the narrow-band limit of the interaction coefficient is given by

$$T_{0,0,0,0}/k_0^3 = X_{nl} = \frac{9T_0^4 - 10T_0^2 + 9}{8T_0^3} - \frac{1}{k_0 D}\left\{\frac{(2v_g - c_0/2)^2}{c_S^2 - v_g^2} + 1\right\}.\qquad(3.51)$$

with $c_S = \sqrt{gD}$ which is the shallow water wave velocity. Notice that the interaction coefficient consists of two terms where the first term is connected with the nonlinear dispersion relation for surface gravity waves, while the second term is due to effects of wave-induced current and corresponding changes in the mean sea level. These two terms are of definite sign so they may cancel each other, which, in fact, happens for

$x = k_0 D = 1.363$. Hence, for intermediate water depth waves the nonlinear interactions are expected to play a relatively minor role. So far this property of the nonlinear transfer has not been incorporated in modern wave prediction models.

It is of interest to study the scaling factor S in the deep water limit first. Then, $T_{0,0,0,0} \to k_0^3$, $\omega_0'' \to -g/4k_0\omega_0$, while $\omega_0 \to \sqrt{gk_0}$. The scaling factor becomes, apart from a constant,

$$S = \frac{\omega_0^{19}}{g^{10}}, \qquad (3.52)$$

which is the usual scaling factor found in the deep-water DIA. In the general case one finds

$$S = \frac{\omega_0 k_0^9}{g} \frac{T_0 X_{nl}^2}{\Omega''} = \frac{\omega_0^{19}}{g^{10}} \frac{1}{T_0^8} \frac{X_{nl}^2}{\Omega''}, \qquad (3.53)$$

and as a natural extension of the deep-water DIA towards shallow waters we have introduced the scaling factor (3.53) into Cy33r1 of the ECMWF wave model software. This scaling factor will give rise to an expected reduction of the strength of the nonlinear transfer around $k_0 D = 1.363$, which has consequences for the frequency downshift of the spectrum in shallow waters. Note that for very shallow water, the scaling factor can become, very large. In the current implementation, we have limited its value. Namely,

$$S = \frac{\omega_0^{19}}{g^{10}} \max\left(\frac{1}{T_0^8} \frac{X_{nl}^2}{\Omega''}, 10\right). \qquad (3.54)$$

As expected, this new addition to S is only active in shallow water. On a global scale, its impact will be limited to the few shallow areas around the world. Furthermore, as discussed in Janssen and Onorato (2007) there are also implications for the determination of the surface elevation kurtosis (and therefore for the generation of extreme events) as for $k_0 D < 1.363$ the nonlinear transfer gives rise to defocusing rather than focusing (as happens in the opposite case of $k_0 D > 1.363$).

However, it was discovered that the approximations in (3.54) may not always hold. It was decided to revert to (3.45) with CY40R1, pending further investigation.

3.4 THE ENERGY BALANCE IN A GROWING WIND SEA

Having discussed the parametrization of the physics source terms we now proceed with studying the impact of wind input, nonlinear interaction and whitecap dissipation on the evolution of the wave spectrum for the simple case of a duration-limited wind sea. To this end we numerically solved (2.24) for infinite depth and a constant wind of approximately 18 m/s, neglecting currents and advection. Typical results are shown in Fig. 3.6 for a young wind sea ($T = 3$ h) and in Fig. 3.7 for an old wind sea ($T = 96$ h). In either case the directional averages of S_{nl}, S_{in} and S_{ds} are shown as functions of frequency. First of all we observe that, as expected from our previous discussions, the wind input is always positive, and the dissipation is always negative, while the nonlinear interactions show a three lobe structure of different signs. Thus, the intermediate frequencies receive energy from the airflow which is transported by the nonlinear interactions towards the low and high frequencies.

Concentrating for the moment on the case of young wind sea, we immediately conclude that the one-dimensional frequency spectrum in the "high"-frequency range must be close to f^{-4}, because the nonlinear source term is quite small (see the discussion in chapter II.3.10 of Komen *et al.* (1994) on the energy cascade caused by the four-wave interactions and the associated equilibrium shape of the spectrum). We emphasize, however, that because of the smallness of S_{nl} it cannot be concluded that the nonlinear interactions do not control the shape of the spectrum in this range. On the contrary, a small deviation from the equilibrium shape would give rise to a large nonlinear source term which will drive the spectrum back to its equilibrium shape. The role of wind input and dissipation in this relaxation process can only be secondary because these source terms are approximately linear in the wave spectrum. The combined effect of wind input and dissipation is more of a global nature in that they constrain the magnitude of the energy flow through the spectrum (which is caused by the four-wave interactions).

At low frequencies we observe from Fig. 3.6 that the nonlinear interactions maintain an "inverse" energy cascade by transferring energy from the region just beyond the location of the spectral peak (at $f \simeq 0.12$ Hz)
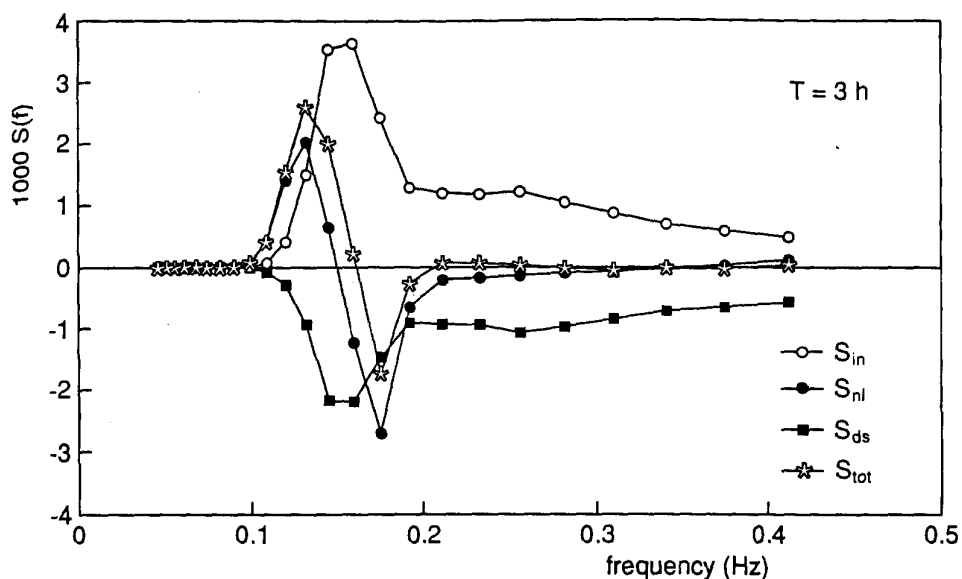
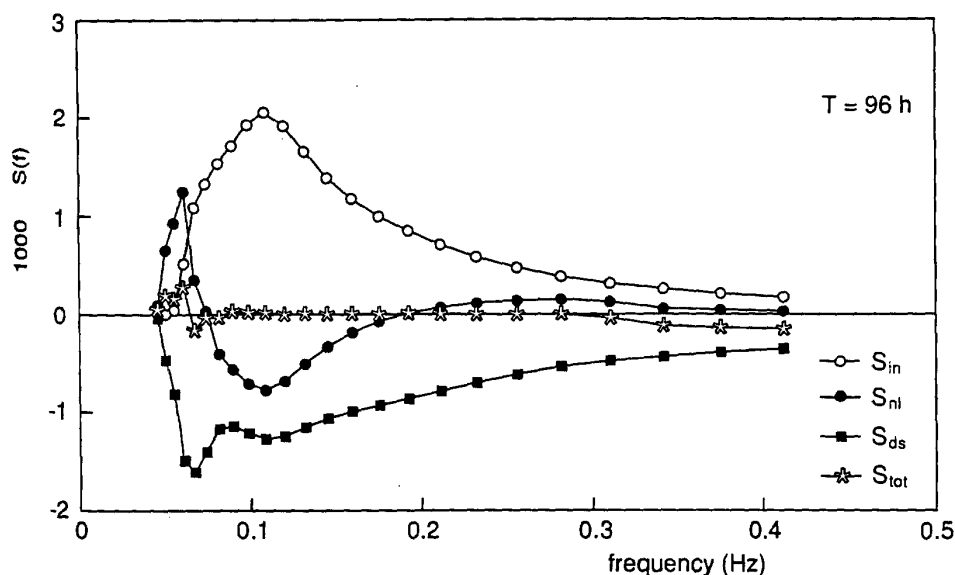**Figure 3.6** *The energy balance for young duration-limited wind sea.*

Figure 3.7 *The energy balance for old wind sea.*

to the region just below the spectral peak, thereby shifting the peak of the spectrum towards lower frequencies. This frequency downshift is, however, to a large extent determined by the shape and magnitude of the spectral peak itself. For young wind sea, having a narrow peak with a considerable peak enhancement, the rate of down-shifting is significant while for old wind sea this is much less so. During the course of time the peak of the spectrum gradually shifts towards lower frequencies until the peak of the spectrum no longer receives input from the wind because these waves are running faster than the wind. Under these circumstances the waves around the spectral peak are subject to a considerable dissipation so that their wave steepness becomes reduced. Consequently, because the nonlinear interactions depend on the wave steepness, the nonlinear transfer is reduced as well. The peak of the positive low-frequency lobe of the nonlinear transfer remains below the peak of the spectrum, where it compensates the dissipation. As a result, a quasi-equilibrium spectrum emerges. The corresponding balance of old wind sea is shown in Fig. 3.7. The nature of this balance depends on details of the directional distribution (see Komen *et al.* (1984) for additional details). The question of whether an exact equilibrium exists appears of little practical relevance. For old wind sea the timescale of down-shifting becomes much larger than the typical duration of a storm. Thus, although from the present knowledge of

wave dynamics it cannot be shown that wind-generated waves evolve towards a steady state, for all practical purposes they do!

Chapter 4

Data assimilation in WAM

Table of contents

The optimal interpolation method described in this chapter was developed for the WAM model and is operational at ECMWF (Lionello *et al.*, 1992). Similar single-time level data assimilation techniques for satellite altimeter wave heights have been applied by Janssen *et al.* (1987, 1989a), Hasselmann *et al.* (1988), Thomas (1988), and Lionello and Janssen (1990).

4.1   INTRODUCTION

We are dealing with the well-known problem that there are more degrees of freedom than observations because the altimeter only provides us with significant wave height. Thus, instead of estimating the full state vector, we estimate only the significant wave height field $\mathbf{H}$ (the index S in the notation for the significant wave height is dropped in the following discussion). The data vector $\mathbf{d}^\mathrm{f}$ consists then of the first-guess model wave heights, interpolated to the locations of the altimeter observations, while $\mathbf{d}^\mathrm{o}$ are the actually observed altimeter wave heights.

The assimilation procedure consists of two steps.

- An analysed field of significant wave heights is created by optimum interpolation, in accordance with the general optimum interpolation (OI) approach outlined in Lorenc (1981) and with appropriate assumptions regarding the error covariances.
- This field is used to retrieve the full two-dimensional wave spectrum from a first-guess spectrum, introducing additional assumptions to transform the information of a single wave height measurement into separate corrections for the wind sea and swell components of the spectrum.

The problem of using wave height observations for correcting the full two-dimensional spectrum was first considered by Hasselmann *et al.* (1988) and Bauer *et al.* (1992), who assimilated SEASAT altimeter wave heights into the WAM model by simply applying a constant correction factor, given by the ratio of altimeter and model wave heights, to the entire spectrum. A shortcoming of this method was that the wind field was not corrected. Thus, although swell corrections were retained for several days, the corrected wind sea relaxed back rapidly to the original incorrect state due to the subsequent forcing by uncorrected winds. Janssen *et al.* (1987) removed this shortcoming by extending the method to include wind corrections, but nevertheless achieved only short relaxation times due to the choice of an insufficient correlation scale (the corrections were essentially limited to a single gridpoint). This was remedied in later versions of the scheme described below.

As in most of these schemes, the present method corrects the two-dimensional spectrum by introducing appropriate rescaling factors to the energy and frequency scales of the wind sea and swell components of the spectrum, and also updates the local forcing wind speed. The rescaling factors are computed for two classes of spectra: wind sea spectra, for which the rescaling factors are derived from fetch and duration growth relations, and swell spectra, for which it is assumed that the wave steepness is conserved. All observed spectra are assigned to one of these two classes. This restriction will be removed in the planned extension of the scheme to include SAR wave mode data.

4.2   WAVE HEIGHT ANALYSIS

First, an analysis of the significant wave height field $\mathbf{H}^{\mathrm{a}} = (H_i^{\mathrm{a}})$ is created by optimum interpolation (cf. Lorenc, 1981) so that

$$\mathbf{H}_i^{\mathrm{a}} = \mathbf{H}_i^{\mathrm{f}} + \sum_{j=1}^{n_{\mathrm{obs}}} W_{ij}(\mathbf{H}_j^{\mathrm{o}} - \mathbf{H}_j^{\mathrm{f}}) \tag{4.1}$$

where $\mathbf{H}^{\mathrm{o}}$ denotes the significant wave height field observed by the altimeter and $\mathbf{H}^{\mathrm{f}}$ is the first-guess significant wave height field computed by the WAM model. Since long-term statistics of the prediction and observational error covariance matrices equation were not available, empirical expressions were taken given by

$$\sigma_{ij}^{\mathrm{f}} = \sigma^{\mathrm{f}} \exp(-|x_i - x_j|/L) \quad \text{and} \quad \sigma_{ij}^{\mathrm{o}} = \delta_{ij}(\sigma_i^{\mathrm{o}}/\sigma_j^{\mathrm{f}}) \tag{4.2}$$

Good results were obtained for a correlation length $L = 1650$ km. This is consistent with the optimal scale length found by Bauer *et al.* (1992) using a triangular interpolation scheme. However, at ECMWF we use a much smaller value of 300 km.

4.2.1   The analysed wave spectrum

In the next step, the full two-dimensional wave spectrum is retrieved from the analysed significant wave height fields. Two-dimensional wave spectra are regarded either as wind sea spectra, if the wind sea energy is larger than $3/4$ times the total energy, or, if this condition is not satisfied, as swell.

In both cases an analysed two-dimensional wave spectrum $F^{\mathrm{a}}(f, \theta; \mathbf{x}, t)$ is computed from the first-guess wave spectrum $F^{\mathrm{f}}(f, \theta; \mathbf{x}, t)$ and the optimally interpolated wave heights H_i^{a} by rescaling the spectrum with two scale parameters A and B such that

$$F^{\mathrm{a}}(f, \theta) = AF^{\mathrm{f}}(Bf, \theta) \tag{4.3}$$

Different techniques are applied to compute the parameters A and B for wind sea or swell spectra.

4.2.2   Retrieval of a wind sea spectrum

The parameters A and B in (4.3) can be determined from empirical duration-limited growth laws relating, in accordance with the scaling laws of Kitaigorodskii (1962), the non-dimensional energy $\epsilon_* = g^2 \epsilon / u_*^4$ (where $\epsilon = (H_{windsea}/4)^2$), mean frequency $\bar{f}_* = u_* \bar{f}_{windsea}/g$ and duration $t_* = gt/u_*$. Specifically, we take the following relations

$$\epsilon_*(t_*) = EGRCRV \times [t_*/(t_* + AGRCRV)]^{BGRCRV} \tag{4.4}$$

$$EGRCRV = 1108, \ AGRCRV = 6000, \ BFCRV = 9.700 \quad \text{for iphys=0,} \tag{4.5}$$
$$EGRCRV = 1065, \ AGRCRV = 6550, \ BFCRV = 10.906 \quad \text{for iphys=1} \tag{4.6}$$

and

$$\epsilon_*(\bar{f}_*) = AFCRV \bar{f}_*^{BFCRV} \tag{4.7}$$

$$AFCRV = 0.0004 \, \text{and} \, BFCRV = -3.0000 \quad \text{for iphys=0,} \tag{4.8}$$
$$AFCRV = 0.0002453 \, \text{and} \, BFCRV = -3.1236 \quad \text{for iphys=1} \tag{4.9}$$

These relationships deviate from the ones proposed by Lionello *et al.* (1992).

Note that it is the significant wave height and the mean frequency of the windsea part of the spectrum that is used. The windsea part of the spectrum is determined by (10.1). The mean frequency is preferred to the peak frequency because its computation is more stable.

Since the first-guess friction velocity was used to generate the waves and the first-guess wave height is known, an estimate of the duration T of the wind sea can be derived from the duration-limited growth laws. Assuming this estimated duration is correct, the analysed wave height yields from the growth laws, (4.4) and (4.7), the best estimates of the friction velocity u_*^a and mean frequency $\bar{f}^a$. The analysed wave height and mean frequency determine then the two parameters A and B given by

$$A = \left(\frac{H^a}{H^f}\right)^2 B \quad \text{and} \quad B = \bar{f}^f / \bar{f}^a \tag{4.10}$$

The corrected best-estimate winds are then used to drive the model for the rest of the wind time step. In a comprehensive wind and wave assimilation scheme, the corrected winds should be also inserted into the atmospheric data assimilation scheme to provide an improved wind field in the forecast model.

4.2.3 Retrieval of a swell spectrum

A spectrum is converted to swell and begins to decay at the edge of a storm, before dispersion has separated the swell into spatially distinct frequencies. One can therefore distinguish between a nonlinear swell regime close to the swell source and a more distant linear regime, where dispersion has reduced the swell wave slopes to a level at which nonlinear interactions have become negligible. Because of these complexities, and also because of a lack of adequate data, there exist no empirical swell decay curves comparable to the growth curves in the wind sea case. However, Lionello and Janssen (1990) showed that for the WAM model swell spectra the average wave steepness is

$$s = \langle k \rangle H / 8\pi \tag{4.11}$$

is approximately the same for all spectra at the same decay times, despite the wide range of significant wave heights and mean frequencies of their data set. Assuming that the effective decay time and therefore the wave steepness is not affected by the correction of the wave spectrum, the scale factors are then given by

$$B = (H^a/H^f)^{\frac{1}{2}} \tag{4.12}$$

$$A = B(H^a/H^f)^2 \tag{4.13}$$

Intuitively, this approach appears reasonable, because a more energetic spectrum will generally also have a lower peak frequency, and increasing the energy without decreasing the peak frequency produces a swell of unrealistic steepness. Since the swell spectrum is not related to the local stress, and only the local wind field is corrected in the assimilation scheme, the wind field is not updated in the case of swell.

4.2.4 The general case

It was shown in Lionello et al. (1992) that the wind sea and swell retrieval scheme works well for simple cases or pure wind sea or swell. If the spectrum consists of a superposition of wind sea and swell, and the wind sea is well separated from the swell, the wind sea and swell correction methods can, in principle, still be applied separately to the two components of the spectrum. In this case, however, one needs to introduce additional assumptions regarding the partitioning of the total wave height correction between wind sea and swell.

The arbitrariness of the present and similar methods of distributing a single wave height correction over the full two-dimensional wave spectrum could presumably be partially alleviated by using maximum likelihood methods based on a large set of observed data, which is now becoming available through ERS-1. However, a more satisfactory solution is clearly to assimilate additional data, such as two-dimensional SAR spectral retrievals, to overcome the inherently limited information content of altimeter wave height data.

4.2.5 Shallow water case

Until now the formulation used to update the wave spectrum assimilation was based on deep water consideration only. The updating scheme has been modified to account for basic shallow water physics, namely

the maximum wave energy and the frequency down shifting are controlled by the water depth. For the wind sea spectrum the maximum energy should not exceed a limit set by the local water depth d

$$\epsilon_*(d_*) = 1711 \tanh(8.0 \times 10^{-4} d_*^{0.96}) \tag{4.14}$$

where the nondimensional depth $d_* = d(g/u_*^2)$ It was found that 4.4 and 4.7 are still good approximations in shallow water, provided that ϵ_* does not exceed the value given by 4.14. The swell update relies on the assumption of conservation of wave steepness. However in shallow water the frequency downshifting is arrested at around $k_0 D = 1.363$. This shallow water behaviour must be respected. It was found empirically that the frequency downshifting in the swell update should only happen up to a point when the mean wave number k_{mean} reaches a minimum limit k_{min}.

$$k_{min} = 0.0981/d_*^{0.425} \tag{4.15}$$

The mean wave number k_{mean} is computed using 3.18. Once this limit is reached, than the spectrum is only adjusted to match the energy level as found from the analysed wave height.

Finally, to avoid updating the sea state across land barriers, the OI scheme was also modified by prescribing that any observation can only modify the value at a given grid point if there is a direct line of view over sea between the observation location and the model point. The proxy for the land/sea mask is taken from the wave height field.

4.3 WAVE SPECTRUM ANALYSIS

4.3.1 Assimilation of wave data

The operational wave model at ECMWF has used altimeter wave height observations since August 1993, first with ERS-1 data and then with ERS-2 until the end of October 2003 when altimeter data from ENVISAT was used instead of ERS-2 because of the lost of ERS-2 global coverage in June 2003. In addition, since February 2006 Altimeter data from Jason is used in the operational analysis as well, and therefore Altimeters provide a good coverage over the world oceans. Until recently, altimeter data was the only data source in the wave model assimilation. Unfortunately, the altimeter only yields significant wave heights and wind speeds over a small footprint. A more accurate description of the sea state requires the full two-dimensional wave energy spectrum. Such observations, albeit neither necessarily fully comprehensive nor independent, are already available with the ERS synthetic aperture radar (SAR). With the launch of ENVISAT, an advanced SAR (ASAR) with a higher spectral resolution operates at twice the current ERS data coverage by providing data every 100 km along the SAR swath over the oceans.

4.3.2 SAR data

Spectra as derived from the ERS-2 SAR wave mode imagette spectra are processed operationally to retrieve ocean wave spectra using an inversion scheme based on the work done by Hasselmann *et al.* (1996) at the Max Planck Institut (MPI). The inversion scheme relies on a model first guess to resolve the directional ambiguity and to provide first guess information on the high frequency part of the wave spectrum. A basic monitoring of the data is done and reported to ESA (http://w3ec2.ecmwf.int/wave/ers/ers2-reports.html). Note however, that due to the motion of the scattering elements induced by the long waves, the SAR only images part of the total wave spectrum. Waves with wavelength shorter than an observation dependent cut-off wavelength are not detected or are heavily distorted. In preparation to the assimilation of SAR data, WAM was modified to include the SAR inversion software as a callable subroutine; therefore all pertinent information from the inversion can be passed to the assimilation.

4.3.3 SAR data assimilation

So far we have only evaluated a method that has already been tested in previous studies. The method is based on the assimilation of wave systems as derived from a spectral partitioning scheme, which works on the principle of the inverted catchment area (Hasselmann *et al.*, 1997; Breivik *et al.*, 1998; Voorrips *et al.*, 1997). The different wave systems are characterized by means of their mean energy, frequency and direction. The mean parameters are assimilated using an optimal interpolation scheme following a cross assignment procedure that correlates the observed and modelled wave systems. The analysed spectra are reconstructed

by resizing and reshaping the model spectra based on the mean parameters obtained from the OI scheme. The SAR assimilation software has been included in the WAM code and can be called in conjunction with the inversion package. Note that the SAR assimilation is performed before the altimeter assimilation as described in Section 4.2.

As reported in the preliminary assessment of the method at the ECMWF workshop on ocean wave forecasting, difficulties were encountered when the method was tested at the current spectral resolution of the wave model (24 directions, 30 frequencies). At the end, it was necessary to introduce some smoothing to reduce the number of spectral partitions and to limit the assimilation to wave systems that are longer than the cut-off wavelength as determined by the SAR inversion.

Following an extensive testing period (Research Department Memorandum R60.9/JB/0274, http://w3ec2.ecmwf.int/wave/documents/memo CY25R3.pdf), the scheme became operational in January 2003. Unfortunately, the ERS-2 global coverage was lost in June 2003 and is now mostly limited to the North Atlantic. Assimilation of ENVISAT ASAR data commenced in February 2006.

Chapter 5

Numerical scheme

Table of contents

In this chapter we discuss the numerical aspects of the solution of the action balance equation as implemented in the ECMWF version of the WAM model.

5.1 TREATMENT OF THE HIGH FREQUENCIES

Although, thus far, we have discussed the transport equation for gravity waves for the action density, because this is the most natural thing to do from a theoretical point of view, the actual WAM model is formulated in terms of the frequency-direction spectrum $F(f, \theta)$ of the variance of the surface elevation. The reason for this is that in practical applications one usually deals with surface elevation spectra, because these are measured by buoys. The relation between the action density and the frequency spectrum is straightforward. It is given by

$$F(\omega, \theta) = \sigma N(\omega, \theta) \tag{5.1}$$

where σ is the intrinsic frequency (see also (2.4)). This relation is in accordance with the analogy between wave packets and particles, since particles with action N have energy σN and momentum kN.

The continuous wave spectrum is approximated in the numerical model by means of step functions which are constant in a frequency-direction bin. The size of the frequency-direction bin depends on frequency. A distinction is being made between a prognostic part and a diagnostic part of the spectrum. The prognostic part of the spectrum has KL directional bands and ML frequency bands. These frequency bands are on a logarithmic scale, with $\Delta f/f = 0.1$, spanning a frequency range $f_{\max}/f_{\min} = (1.1)^{ML-1}$. The logarithmic scale has been chosen in order to have uniform relative resolution, and also because the nonlinear transfer scales with frequency. The starting frequency may be selected arbitrarily. The present version of the ECMWF wave prediction system has 36 directions and 36 frequencies, with starting frequency $f_{\mathrm{o}} = 0.035$ Hz.

Beyond the high-frequency limit f_{c} of the prognostic region of the spectrum, an f^{-5} tail is added, with the same directional distribution as the last band of the prognostic region. The diagnostic part of the spectrum is therefore given as

$$F(f, \theta) = F(f_{\mathrm{c}}, \theta)\left(\frac{f}{f_{\mathrm{c}}}\right)^{-5} \quad \text{for } f > f_{\mathrm{c}} \tag{5.2}$$

In the ECMWF version of the WAM model the high-frequency limit is set as

$$f_{\mathrm{c}} = \min\{f_{\max}, 2.5\langle f\rangle_{\mathrm{windsea}}\} \quad \text{for iphys=0,} \tag{5.3}$$

$$f_{\mathrm{c}} = \min\{f_{\max}, \max\{2.5\langle f\rangle_{\mathrm{windsea}}, 3.0 f_{PM}\}\} \quad \text{for iphys=1} \tag{5.4}$$

where f_{PM} is Pierson-Moskowitz frequency based on friction velocity

$$f_{PM} = \frac{g}{28 \; 2\pi \; u_*} \tag{5.5}$$

Thus, the high-frequency extent of the prognostic region is scaled by the mean frequency $\langle f \rangle_{\text{windsea}}$ of the local windsea. A dynamic high-frequency cut-off, f_c, rather than a fixed cut-off at f_{max} is necessary to avoid excessive disparities in the response time scales within the spectrum.

A diagnostic tail needs to be added for $f > f_c$ to compute the nonlinear transfer in the prognostic region and also to compute the integral quantities which occur in the dissipation source function and the wave induced stress. Tests with an f^{-4} tail show that (apart from the calculation of the wave-induced stress) the results are not sensitive to the precise form of the diagnostic tail. The contribution to the total energy from the diagnostic tail is normally negligible. Because observations seem to favour an f^{-5} power law (Birch and Ewing, 1986; Forristall, 1981; Banner, 1990) this power law is used for the high-frequency part of the spectrum.

Using (3.7),the kinematic wave induced stress (3.10) can be written as

$$\tau_{\text{w}} = \epsilon^{-1} g \int_0^{2\pi} \int_0^{\omega_c} d\omega d\theta \, \frac{\mathbf{k}}{\omega} S_{in} + \epsilon^{-1} g \int_0^{2\pi} \int_{\omega_c}^{\infty} d\omega d\theta \, \frac{\mathbf{k}}{\omega} \gamma F(\omega, \theta), \tag{5.6}$$

The first integral on the right hand side of (5.6) is the prognostic part of the spectrum which is obtained by numerically solving the energy balance equation. The second integral can be parameterized by assuming the f^{-5} power law for the spectrum, deep water physics, and that at high frequency, the stress is in the wind direction. Moreover, at high frequency, the growth rate γ is virtually independent of direction (Janssen (1991)), and (3.5) can be written as

$$\mu_{hf} = \frac{g z_{\text{o}}}{c^2} \exp\left(\frac{\kappa}{(u_*/c) + z_\alpha}\right), \quad \mu_{hf} <= 1 \tag{5.7}$$

For iphys=0, using (3.1), (3.3) and (3.4) for deep water, the magnitude of the high frequency contribution to the kinematic wave induced stress can be written as the product of two integrals)

$$\tau_{\text{w}_{hf}} = \frac{(2\pi)^4 f_c^5}{g^2} \, u_*^2 \int_0^{2\pi} d\theta \, F(f_c, \theta)[\max(\cos(\theta - \phi), 0)]^3 \; \frac{\beta_{\text{m}}}{\kappa^2} \int_{\omega_c}^{\infty} \frac{d\omega}{\omega} \, \mu_{hf} \ln^4(\mu_{hf}), \tag{5.8}$$

The integral over directions can be evaluated using the prognostic part of the spectrum, where as the second integral is only function of u_* and the Charnock parameter (3.11). Until CY45R1, It was tabulated beforehand. Note that the integration is bounded because $\mu_{hf} <= 1$

$$TAUHF = \frac{\beta_{\text{m}}}{\kappa^2} \int_{\omega_c}^{\infty} \frac{d\omega}{\omega} \, \mu_{hf} \ln^4(\mu_{hf}) = \frac{\beta_{\text{m}}}{\kappa^2} \int_{Y_c}^{1} \frac{dY}{Y} \, \mu_{hf} \ln^4(\mu_{hf}), \quad Y_c = \max\left(\omega_c, x_0 \frac{g}{u_*}\right) \sqrt{\frac{z_0}{g}} \tag{5.9}$$

where x_0 is the solution of $\mu_{hf} = 1$ in terms of $x = \frac{\omega}{g/u_*}$

$$\mu_{hf} = \alpha x^2 \exp\left(\frac{\kappa}{x + z_\alpha}\right) = 1, \tag{5.10}$$

where for typical values of the Charnock parameter α, $x_0 \sim 0.05$

Since CY45R1 (June 2018), it was found that it was as numerically efficient to compute the integral in (5.9) following the variable transformation $X = \ln(Y)$ and only a few discretised points using the Simpson integration method.

For iphys=1, because of the sheltering coefficient, u_*^2 has to be moved inside the integral for TAUHF (5.9) and be replaced by a frequency dependent $u_*'^2(\omega)$

$$u_*'^2 = u_*^2 - tauwshelter \int_{\omega_c}^{\omega} \frac{d\omega'}{\omega'} \mu_{hf} \ln^4(\mu_{hf}) \tag{5.11}$$

where *tauwshelter* is given by (3.26)

We will now discuss the different numerical schemes and time steps that are used to integrate the source functions and the advective terms of the transport equation.

5.2 IMPLICIT INTEGRATION OF THE SOURCE FUNCTIONS

An implicit scheme was introduced for the source function integration to enable the use of an integration time step that was greater than the dynamic adjustment time of the highest frequencies still treated prognostically in the model. In contrast to first and second generation wave models, the energy balance of the spectrum is evaluated in detail up to a high cut-off frequency. The high-frequency adjustment time scales are considerably shorter than the evolution time scales of the energy-containing frequency bands near the peak of the spectrum, in which one is mainly interested in modelling applications. Thus, in the high-frequency region it is sufficient to determine the quasi-equilibrium level to which the spectrum adjusts in response to the more slowly changing low-frequency waves, rather than the time history of the short time scale adjustment process itself. An implicit integration scheme whose time step is matched to the evolution of the lower frequency waves meets this requirement automatically: for low-frequency waves, the integration method yields, essentially, the same results as a simple forward integration scheme, while for high frequencies the method yields the (slowly changing) quasi-equilibrium spectrum (WAMDI Group (1988)).

The original WAM model used a time-centred implicit integration scheme, but Hersbach and Janssen (1999) found that numerical noise occurred which may be avoided by a two-time level, fully implicit approach. The fully implicit equations (leaving out the advection terms) are given by

$$F_{n+1} = F_n + \Delta t S_{n+1} \tag{5.12}$$

where Δt is the time step and the index n refers to the time level.

If S_{n+1} depends linearly on F_{n+1}, (5.12) could be solved directly for the spectrum F_{n+1} at the new time step. Unfortunately, none of the source terms are linear. We therefore introduce a Taylor expansion

$$S_{n+1} = S_n + \frac{\partial S_n}{\partial F} \Delta F + \cdots \tag{5.13}$$

The functional derivative in (5.13) (numerically a discrete matrix M_n) can be divided into a diagonal matrix Λ_n and a non-diagonal residual N_n,

$$\frac{\partial S_n}{\partial F} = M_n = \Lambda_n + N_n \tag{5.14}$$

Substituting (5.13) and (5.14) into (5.12), realizing, in addition, that the source term S may depend on the friction velocity u_* at time level $n + 1$, we obtain

$$[1 - \Delta t\{\Lambda_n(u_*^{n+1}) + N_n(u_*^{n+1})\}]\Delta F = \Delta t S_n(u_*^{n+1}) \tag{5.15}$$

with $\Delta F = F_{n+1} - F_n$. A number of trial computations indicated that the off diagonal contributions were generally small if the time step was not too large. Disregarding these contributions, the matrix on the left-hand side can be inverted, yielding for the increment ΔF,

$$\Delta F = \Delta t S_n(u_*^{n+1})[1 - \Delta t \Lambda_n(u_*^{n+1})]^{-1} \tag{5.16}$$

Nevertheless, in practice numerical instability is found in the early stages of wave growth. These are either caused by the neglect of the off diagonal contributions or by the circumstance that the solution is not always close to the attractor of the complete source function. Therefore a growth limitation needs to be imposed. In the ECMWF version of WAM a variant of the growth limiter of Hersbach and Janssen (1999) is used: the maximum increment in the spectrum, $|\Delta F|_{\max}$, is given by

$$|\Delta F|_{\max} = 5 \times 10^{-7} g u_* f^{-4} \langle f \rangle_{\mathrm{windsea}} \Delta t \tag{5.17}$$

where again $\langle f \rangle_{\mathrm{windsea}}$ is an appropriately defined mean frequency for windsea. For a typical test case, good agreement was obtained between an explicit integration with a time step of 1 minute and the implicit scheme with only diagonal terms for time steps up to about 20 minutes.

At the end of the integration time step, the wave-induced stress τ_w and the total stress τ are evaluated using the spectrum F_{n+1} at the next time level. This is important in case of rapidly varying circumstances, and had a noticeable impact on cases of rapid cyclo-genesis and on atmospheric scores (Janssen and Bidlot, 2001).

5.3 ADVECTIVE TERMS AND REFRACTION

The advective and refraction terms in the energy balance equation have been written in flux form. We shall only consider, as an example, the one-dimensional advection equation
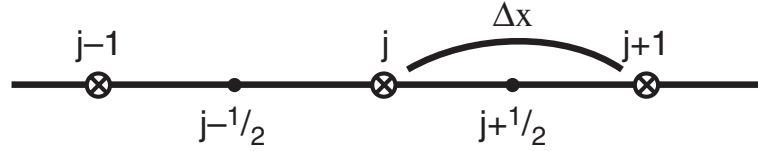
$$\frac{\partial}{\partial t} F = -\frac{\partial}{\partial x} \Phi \tag{5.18}$$

with flux $\Phi = c_{\mathrm{g}} F$, since the generalization to four dimensions λ, ϕ, θ and ω is obvious. Two alternative propagation schemes were tested, namely a first order upwinding scheme and a second order leap frog scheme (for an account of the numerical schemes of the advection form of the energy balance equation see WAMDI Group (1988)). The first order scheme is characterized by a higher numerical diffusion, with an effective diffusion coefficient $D \sim \Delta x^2 / \Delta t$, where Δx denotes grid spacing and Δt is the time step. For numerical stability the time step must satisfy the inequality $\Delta t < \Delta x / c_{\mathrm{g}}$, so that $D > c_{\mathrm{g}} \Delta x$. The advection term of the second order scheme has a smaller, inherent, numerical diffusion, but suffers from the drawback that it generates unphysical negative energies in regions of sharp gradients. This can be alleviated by including explicit diffusion terms. In practice, the explicit diffusion required to remove the negative side lobes in the second order scheme, is of the same order as the implicit numerical diffusion of the first order scheme, so that the effective diffusion is generally comparable for both schemes.

As shown in WAMDI Group (1988) both schemes have similar propagation and diffusion properties. An advantage of the second order scheme is that the lateral diffusion is less dependent on the propagation direction than in the first order scheme, which shows significant differences in the diffusion characteristics for waves travelling due south-north or west-east compared with directions in between. The first order scheme has the additional problem that there is excessive shadowing behind islands when waves are propagating along the coordinate axes. However, these undesirable features in the first order upwinding scheme may be alleviated by rotating the spectra by half its angular resolution, in such a way that no spectral direction coincides with the principle axes of the spatial grid. In general, the differences between the model results using first or second order propagations methods were found to be small, but there is a preference for the first order scheme because of its efficiency and simplicity.

Historically, the main motivation for considering the second order scheme in addition to the first order scheme was not to reduce diffusion, but to be able to control it. In contrast to most other numerical advection problems, an optimal propagation scheme for a spectral wave model is not designed to minimize the numerical diffusion, but rather to match it to the finite dispersion associated with the finite frequency-direction spectral resolution of the model (SWAMP Group (1985), appendix B). In this context, it should be pointed out that an ideal propagation scheme would give poor results for sufficiently large propagation times, since it would not account for the dispersion associated with the finite resolution in frequency and direction (the so-called garden sprinkler effect). Now, the dispersion due to the different propagation velocities of the different wave components within a finite frequency-direction bin increases linearly with respect to propagation time or distance, whereas most propagation schemes yield a spreading of the wave groups which increases with the square root of the propagation time or distance. However, Booij and Holthuijsen (1987) have shown that linear spreading rates may be achieved by introducing a variable diffusion coefficient proportional to the age of the wave packets. This idea has been tested in the context of a third generation wave model by Chi Wai Li (1992) and Tolman (2000) who use an averaged age of the wave packets per ocean basin.

To summarize our discussion, we have chosen the first order upwinding scheme because it is the simplest scheme to implement (requiring less computer time and memory) and because in practice it gives reasonable results. Applied to the simple advection scheme in flux form (5.18) we obtained the following discretization, where for the definition of grid points we refer to Fig. 5.1.

Figure 5.1 *Definition of grid points for first order upwinding scheme.*

The rate of change of the spectrum ΔF_j in the jth grid point is given by

$$\Delta F_j = -\frac{\Delta t}{\Delta x}(\Phi_{j+1/2} - \Phi_{j-1/2}) \tag{5.19}$$

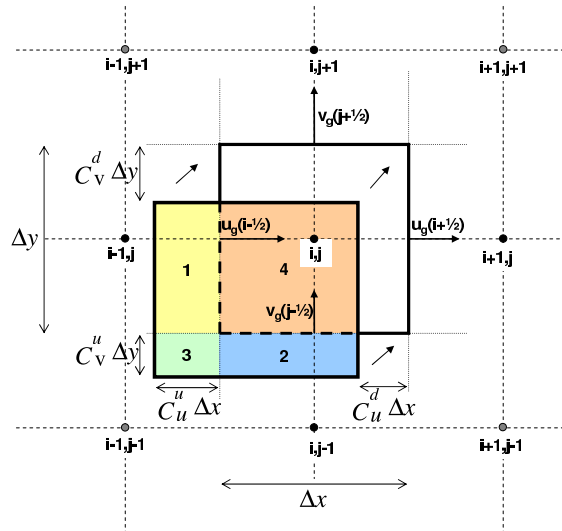where Δx is the grid spacing and Δt the propagation time step, and

$$\Phi_{j+1/2} = \frac{1}{2}[v_j + |v_j|]F_j + \frac{1}{2}[v_j - |v_j|]F_{j+1} \tag{5.20}$$

where $v_j = 0.5(c_{g,j} + c_{g,j+1})$ is the mean group velocity and the flux at $j - 1/2$ is obtained from (5.20) by replacing $j + 1/2$ with $j - 1/2$. The absolute values of the mean speeds arise because of the upwinding scheme. For example, for flow going from the left to the right the speeds are positive and, as a consequence, the evaluation of the gradient of the flux involves the spectra at grid points $j - 1$ and j.

From Cy33r1 onwards the above upwinding scheme was improved by considering the corner points as well. In order to appreciate this point we study the simple case of the advection in x,y space. The wave energy balance equation in flux form becomes

$$\frac{\partial}{\partial t}F + \frac{\partial}{\partial x}(u_g F) + \frac{\partial}{\partial y}(v_g F) = 0, \tag{5.21}$$
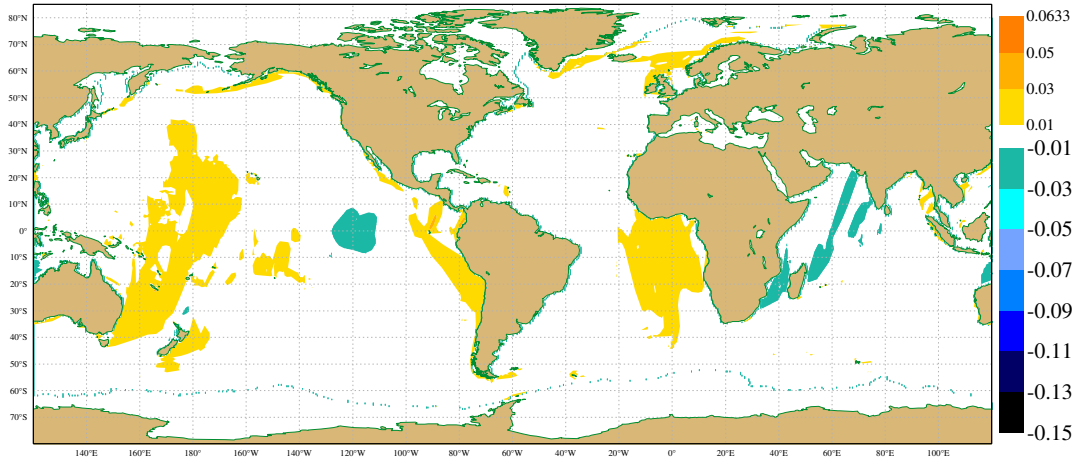
where F is the wave variance spectrum and (u_g, v_g) are the group speed x and y- components. Until Cy33r1,

Figure 5.2 *Schematic representation of the volumes swept in the corner transport method*

(5.21) was solved using a first order upwinding scheme. One of the drawbacks of using this scheme is that it

Figure 5.3 *Mean difference in significant wave heights over 3 months between a hindcast run with the new corner transport scheme (f11m) and a run with the original upwinding scheme (f0sn). Both experiments used the 40 km standalone ECWAM, forced by 10 m neutral winds from the operational analysis.*

only considers contributions from neighbouring grid points in the x and y directions, no contributions from the corners of the grid are considered. The simple upwinding scheme can be extended to account for the corner points by using the so-called Corner Transport Upstream (CTU) scheme. One way to understand how the CTU algorithm works is to follow how a grid box cell, centered at point (i, j) is advected backwards over one time step by the group speed velocities on each gridbox facet $(u_g(i \pm 1/2), v_g(j \pm 1/2))$ Fig. 5.2.

$$u_g(i \pm 1/2) = \frac{u_g(i) + u_g(i \pm 1)}{2}, v_g(j \pm 1/2) = \frac{v_g(j) + v_g(j \pm 1)}{2}. \tag{5.22}$$

Following the location of the gridbox at time level $n + 1$ back in time, one gets the picture in Fig. 5.2, where the transported cell overlaps on three upstream cells. The area of intersections represents the weights to attribute to F on the original grid but at the previous time level n. The scheme can then be written as:

$$F_{i,j}^{n+1} = (1 - C_u^d)(1 - C_v^d)F_{i,j}^n + C_u^u(1 - C_v^d)F_{i-1,j}^n + C_v^u(1 - C_u^d)F_{i,j-1}^n + C_u^u C_v^u F_{i-1,j-1}^n \tag{5.23}$$

where the Courant numbers in x and y directions are

$$C_u^u = \frac{u_g(i - 1/2)\Delta t}{\Delta x}, C_v^u = \frac{v_g(j - 1/2)\Delta t}{\Delta y},$$

$$C_u^d = \frac{u_g(i + 1/2)\Delta t}{\Delta x}, C_v^d = \frac{v_g(j + 1/2)\Delta t}{\Delta y}. \tag{5.24}$$
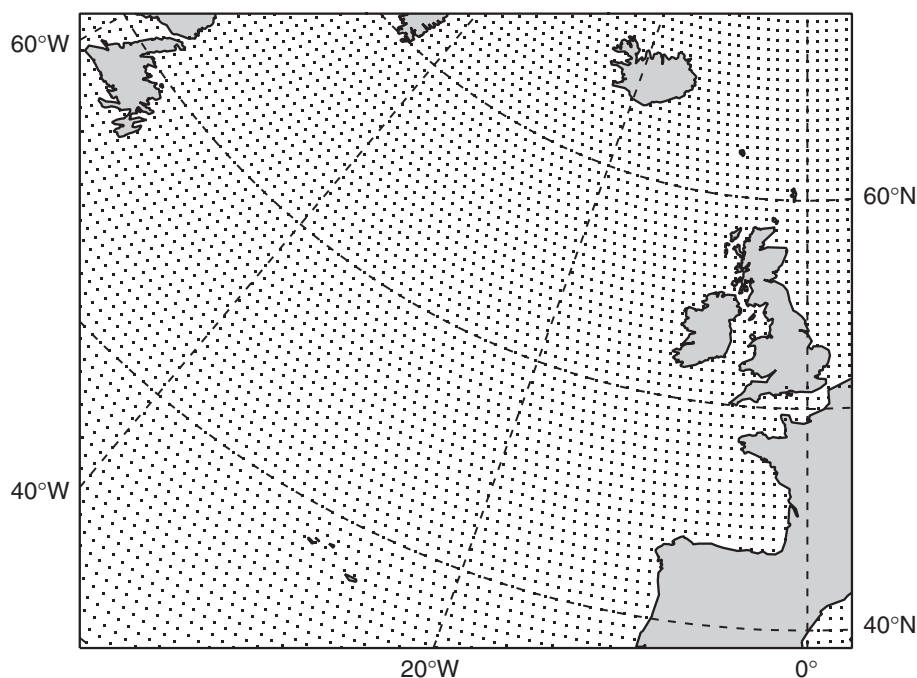
As in the upwinding scheme, stability is conditional on all Courant numbers to be between 0 and 1. This scheme was generalized for spherical coordinates and for irregular lat-lon grid as used in operations.

This new scheme will yield a slightly more uniform propagation in all directions. However, in the mean, the main impact of the scheme is along coastline and around islands as can be seen in Fig. 5.3.

We furthermore remark that one could consider using a semi-Lagrangian scheme for advection. This scheme is gaining popularity in meteorology because it does not suffer from the numerical instabilities which arise in conventional discretization schemes when the time step is so large that the Courant–Friedrichs–Levy (CFL)

criterion is violated. The wave model community has, so far, not worried too much about this problem because advection is a relatively inexpensive part of the computations. In addition, in most applications, the propagation time is larger or equal to the source time step, which is usually 20 min. According to the CFL criterion, short propagation time steps (less than, say, 10 min) are only required for very high resolution ($\Delta x < 20$ km). But in these circumstances the advection will induce changes in the physics on a short time scale, so that it is advisable to decrease the source time step accordingly. Nevertheless, adopting a pragmatic point of view, this may result in a considerable increase in computation time and in the present versions of the ECWAM model it is therefore allowed to have a propagation time step which is less or equal to the source time step.

We also comment on the so-called pole problem in the case of the use of spherical coordinates. When moving towards the poles, the distance in the latitudinal direction decreases. Clearly, close to the poles violation of the CFL criterion occurs. In the ECMWF version of the WAM model this problem is solved by choosing an irregular spherical grid in such a way that the distance in the latitude direction is more or less fixed to its value at the equator (this is effectively a polar stereographic grid). An example of such a grid from the present operational ECMWF WAM model is shown in Fig. 5.4. The advection scheme is still formulated in terms of spherical coordinates but the gradient in the longitudinal fluxes is evaluated by linear interpolation of the fluxes from the closest neighbours. The additional advantages of the use of an irregular spherical grid is a reduction in the total number of grid points by 30%, giving a substantial reduction in the cpu consumption.

Figure 5.4 *Irregular grid for North Atlantic area on a polar stereographic projection.*

Finally, the wave model grid has so far only extended up to 81^0 North. It therefore did not include the North Pole as it was assumed that this area was always covered by ice. Nowadays it is known that this is not always guaranteed and it is expected that in the near future there is no sea ice over the North Pole during part of the Summer. For this reason the wave model grid has since CY35r2 been extended up to the North pole. The singularity at the North pole is avoided by allowing a slight offset of the latitude from 90^0.

5.4 BOUNDARY CONDITIONS AND GRID NESTING

Normally the wave model grid is surrounded by land points. Therefore, the natural boundary conditions are no energy flux into the grid and free advection of energy out of the grid at the coast line.

The generation and propagation of ocean waves covers a wide range of space and time scales. In the open ocean, the scale of a wind sea system is determined by the size of a depression, which typically has scales of

the order of 1000 km. On the other hand, near the coast, the scale of a wave system is determined by the coastal geometry and bottom topography, which have usually much smaller scales. A wave model which covers all scales uniformly is not practicable because of computer limitations. In addition, running a high-resolution wave model for the open ocean seems a waste of computer time.

There are several ways out of this problem. One approach would be to run a wave model with a variable grid, having a high resolution whenever needed (for example near the coast) and having a coarse resolution in the open ocean. So far this approach has not been followed. The WAM model was developed with the practical application in mind of running a global ocean wave model at ECMWF and running limited area models at the European National Weather Centres. Therefore, preference was given to another solution, in which one has the option to run the model on nested grids. This gives the opportunity to use results of a coarse mesh model from a large region in a fine mesh regional model. Several successive levels of nesting may be necessary. The two-dimensional spectra computed by the coarse mesh model are saved at grid points which are on the boundary of the limited area, high-resolution grid. These spectra are then interpolated in space and time to match the high resolution at the grid boundaries. It should be pointed out, however, that a straightforward linear interpolation of spectra gives problems because the interpolated spectra are usually not well balanced, resulting in their rejection when used as boundary conditions for a fine mesh run. To circumvent this problem, the following interpolation procedure is used. Instead of linearly interpolating the spectra from the adjacent points of the coarse grid directly, we rescale these spectra in such a way that the rescaled spectrum has the same mean frequency, mean wave direction and wave energy as found from a linear interpolation of these mean quantities to the fine mesh grid point. The wave spectrum at the fine mesh grid point is then found by linearly interpolating the rescaled spectra. This procedure seems to give satisfactory results.

5.5 PARAMETRIZATION OF SUBGRID BATHYMETRY

5.5.1 The problem

By looking at monthly mean analysis wave height increments, especially during the northern hemisphere summer, it appears that there are areas where the wave model first guess is systematically too high or too low. The underestimation in wave heights tends to be located in the active storm track areas or in areas affected by the Indian sub-continent monsoon. It is known that this underestimation is likely caused by too weak model winds. On the other hand, the overestimation for most of the tropical and northern Pacific cannot be explained in terms of local winds. After further scrutiny, it appears that these systematic overestimations are often present in areas where small island chains exist (French Polynesia and Micronesia in the Pacific Ocean, Maldives Islands and Andaman Islands in the Indian Ocean and Azores and Cape Verde Islands in the Atlantic Ocean, ...).

Hence, it appears that small islands and submerged bathymetric features that are not at all resolved by the coarse wave model grid (55 km) may have a larger impact on the wave climate than it is usually assumed. Although, in the operational grid up to Cy28r1, the representation of some islands were artificially enhanced to produce the necessary blocking to wave propagation, the results were not very satisfactory. A more appropriate and automatic procedure has been designed to deal with small and not so small islands and reefs. This simple parametrization was successfully implemented in Cy28r1.

5.5.2 Treatment of unresolved bathymetry

Up to Cy28r1, the operational 55 km wave model grid was based on the ETOPO5 data set that represents the land and sea-bottom elevation on a 5-minute latitude/longitude grid. This data set is available from the National Geophysical Data Center (http://www.ngdc.noaa.gov/mgg/). Recently, NGDC produced a finer data set, namely ETOPO2 that has a 2-minute resolution. Fig. 5.5 shows the bathymetry for an area centred on the Tuamotu Archipelago in the South Pacific as derived from the ETOPO2 data (only sea points with water depth less than 300 m are shown). The complexity of the bathymetry is clearly visible. This data set can be used to produce the wave model grid by averaging the depths of all ETOPO2 sea points within a model grid box and vice-versa for land points. A model grid box is considered to be over sea if more than half the ETOPO2 points are sea points and a small area 4 by 4 minutes centred on the model grid point is not land. Fig. 5.6 shows the resulting mean depth for the 55 km grid. Much of the shallow features of the archipelago are
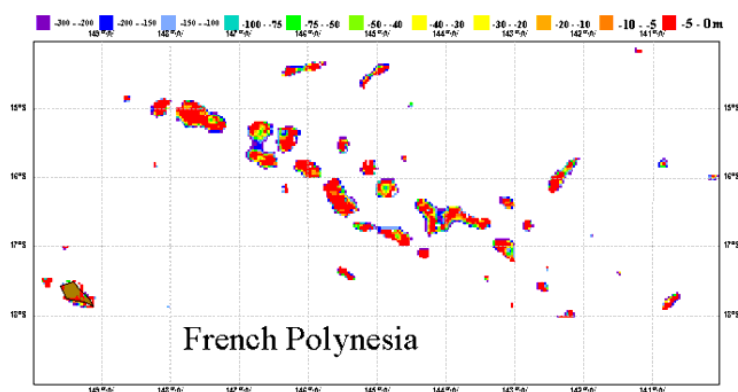
gone. It is therefore not surprising that, when model swell propagates across this area, very little attenuation is experienced (even with the model shallow water physics switched on).

Based on a similar idea as in Tolman (2003) and Hardy *et al.* (2001), we have modified the wave propagation scheme to limit the amount of wave energy that can be advected through these sub grid bathymetric features. The WAM model uses a simple first order upwind scheme that requires the knowledge of the wave spectral flux entering a given grid box in the upwind direction. These incoming fluxes are specified by the product of the wave spectral component and the corresponding mean group velocity perpendicular to the upwind grid box facet. However, in reality, if small islands or shallow water features are present, only part of incoming energy will reach the central grid point. With the availability of a finer resolution topographic data set such as ETOPO2, it is possible to estimate how much obstruction these features would produce.

For each model grid point, the 2-minute data are analysed line by line in all four cardinal directions from the model grid point up to the neighbouring grid points. If land or shallow water features are present, then the proportion of how much energy would have propagated from the neighbouring points to the grid point along each line is reduced accordingly. Land and very shallow features are entirely blocking the flux along the respective line, provided deeper data points on both sides surround them (in order to be an obstruction and not a coastline). On the other hand, points, which are shallow enough to affect the incoming waves but deep enough that they do not block the waves, are only reducing the flux in proportion to the total number of points in a line. How relatively shallow the water is depends on the frequency (wavelength) of the spectral component under consideration. Very shallow features are defined such that their respective depth is less than $0.1/k$, where k is the deep water wave number ($\omega^2 = gk$) of the incoming waves. If waves are not entirely obstructed by the small bathymetric features, they are however assumed to be partially blocked if the depth is of the order $2/k$ or less and the mean grid point depth is at least 10 times larger than that threshold.

The total obstruction for each upwind flux is then obtained by summing over all lines that are intersecting the corresponding grid box facet. High frequency waves are less affected by the bathymetry than low frequency components. Thus, at each grid point there is a transmission factor for each discretised frequency bin corresponding to all four cardinal directions. Fig. 5.7 shows how much energy is allowed to propagate towards the north for the first frequency bin of the model (wavelength 1360 m) for the same area as in Fig. 5.5. These long waves will indeed be quite attenuated as they cross the Archipelago. On the other hands, the short waves should be a lot less affected by the unresolved bathymetry. Fig. 5.8 displays the corresponding transmission coefficient for the very short waves in the model (wavelength 6 m). The impact of the unresolved bathymetry is indeed much reduced.

The net benefit of using this new parametrization was illustrated in Bidlot and Janssen (2003) and in the e-suite for Cy28r1. With CY45R1 (June 2018), we upgraded the bathymetry by switching to ETOPO1.

Figure 5.5 *ETOPO2 bathymetry obtained from the National Geophysical Data Center (only sea points shallower than 300 m are shown).*
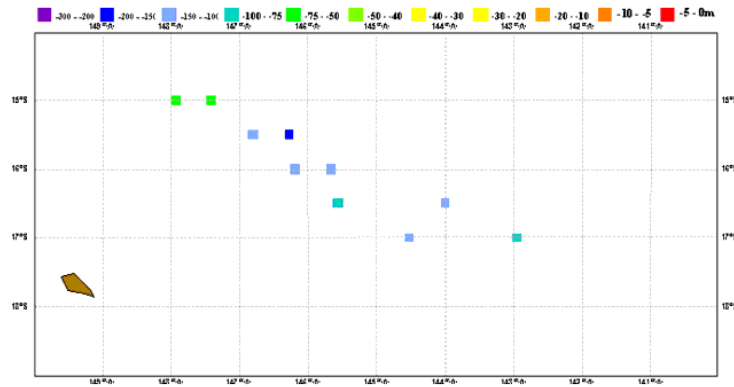
Figure 5.6 *WAM bathymetry (only sea points shallower than 300 m are shown) for the 55 km grid.*
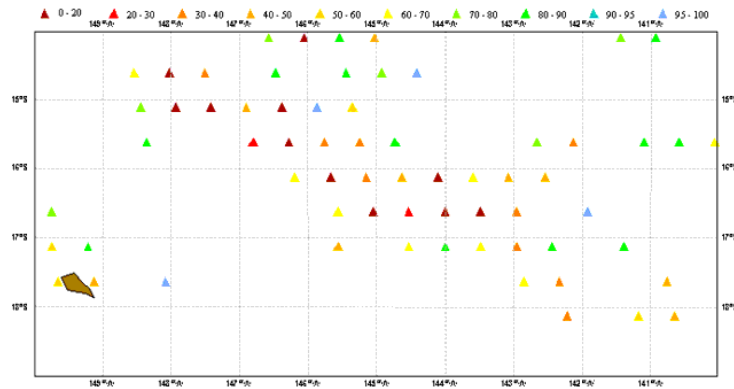

Figure 5.7 *Percentage of the wave energy that is allowed to propagate northwards for the lowest frequency bin (0.035 Hz).*
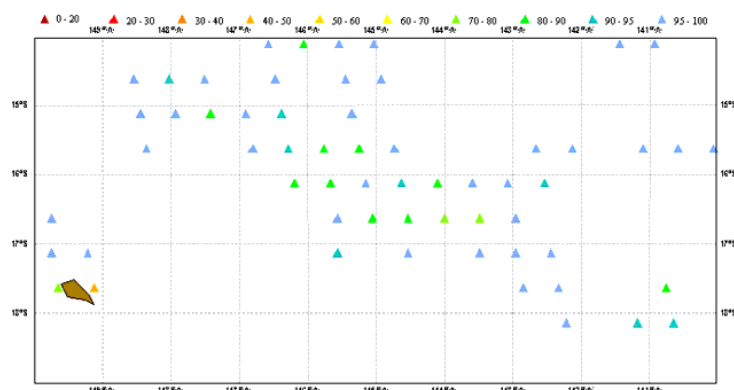

Figure 5.8 *Percentage of the wave energy that is allowed to propagate northwards for the highest frequency bin (0.55 Hz).*

Chapter 6

WAM model software package

Table of contents

The WAM model development was finished in the early 1990s. Since then there has been continuous effort at ECMWF to streamline the software in areas such as input-output (IO), archiving, vectorization and to adapt the code to the new massive parallel (vector) machines. Nevertheless, many of the original features of the WAM model have been retained. These are described below, followed by a description of the additional features that have been introduced at ECMWF.

6.1   INTRODUCTION

The original WAM model software that has been developed over a period of seven years (1985–1992) is fairly general. Spectral resolution and spatial resolution are flexible and the model can be run globally or regionally with open and closed boundaries. Open boundaries are important in case one wishes to use results from a coarse resolution run as boundary conditions for a fine mesh, limited area run. Options such as shallow water, depth refraction or current refraction may be chosen. In this section we shall briefly describe the wave model software with emphasis on flexibility and universality. Before doing this, we shall first discuss some design choices.

The model was developed with an important application in mind, namely for predicting operationally waves over the whole globe. With a modest spatial resolution of $3°$ (resulting in approximately 4000 grid points) and 25 frequencies and 12 directions, it follows that about 1.2 million equations have to be solved. Since the most expensive part of the numerical code, the nonlinear source term, cannot be vectorized, vectorization is achieved over the grid points, which are placed in the innermost loop. In order to make this loop as long as possible, a mapping from the two-dimensional spherical grid to a one-dimensional array is performed. If there are no limitations to the amount of internal memory of the computer, the most efficient procedure is to convert the entire global grid to a single one-dimensional array. In practice, however, there may be restrictions on the amount of memory to be used. For example, in the early days of the WAM model development, the model was tested on a Cray 1S with an internal memory of only 750,000 words. Clearly, the full model grid would not fit into this small memory. It was, therefore, decided to split up the globe in blocks of $NIBLO$ grid points. Typically, $NIBLO = 512$. The blocks are set up in such a way that the north and south boundaries are either land or open ocean, whereas the east and west boundaries are land, periodic (this occurs, for instance, in the southern ocean), or open ocean (for nesting). In order to allow waves to propagate across the north or south boundaries of a block, the blocks overlap by a number of latitudes, depending on the propagation scheme. Since we have chosen a first order upwinding scheme, which involves only two neighbouring grid points, the number of overlapping latitudes is two. The computations are done from the last but one southerly latitude to the last but one most northerly latitude (see also Fig. 6.1 and Günther *et al.* (1991)). Although loading only one block at a time circumvents the problem of the limited memory, the drawback of this approach is that extensive IO operations are needed. After performing the computations on block IG, the results have to be written to disc and the results of the previous time step of block $IG + 1$ have to be read before the

computations on block $IG + 1$ may be started. To avoid waiting for IO, an IO scheme is used that allows for simultaneously writing results of block $IG - 1$, reading results of the previous time step of block $IG + 1$, while performing calculations on block IG. The block structure combined with this IO scheme yields a very efficient and flexible wave model code. With the preprocessing program PREPROC one may lay out a block structure according to one's own choice.
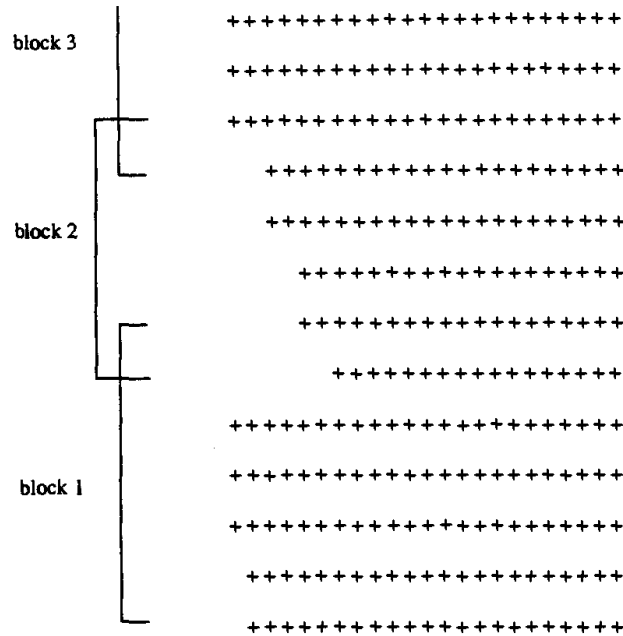

Figure 6.1 *Structure of the model grid.*

The later generation of computers, such as the CRAY-YMP, allowed the whole globe to be loaded into the core of the computer, hence a one block structure may be chosen. This is, however, not always the optimal choice when high resolution applications are considered and/or when the wave model is coupled to another model, for example an atmospheric model or a storm-surge model.

Later generation of computers are based on the concept of massive parallel computing. In this context it is important to distinguish between memory shared and memory distributed machines. Machines such as the CRAY-YMP and the CRAY-C90 are examples of shared memory machines. By using Macrotasking it was relatively straightforward to develop a version of the WAM model that utilised more processors in an efficient way. Note that there are limits to the number of processors to be used, because each processor requires a sufficient amount of work. Therefore, a low-resolution version of the WAM model, such as the 1.5 degree model, could only perform efficiently on about 4 processors, while the high resolution, 55 km, version ran still efficiently on 16 processors.

The present generation of computers either are memory distributed machines or have memory distribution over nodes while per node the processors share the memory. In general, a memory distributed machine requires a different approach which is described in the next subsection.

6.2 MASSIVE PARALLEL COMPUTING

6.2.1 Overview

Memory distributed machines such as the Fujitsu vpp series require the introduction of message passing between processors (known as processing elements (PEs)). Therefore, one PE can send a message which is received by one or more other PEs. In its very basic implementation, the message is nothing more than a one-dimensional array of a given type containing values that are needed by the other PE(s) plus the necessary information about the sender and receiver. For a successful message exchange both send and receive should be completed.

Message passing in the ECMWF version of the WAM model was introduced in 1996 based on the message passing library MPELIB. This newly developed code can also run on non-distributed memory machines and on a single PE.

When running in parallel it is important to have an even distribution of work over the PEs in order to avoid load unbalance. In the case of the WAM model it comes down to splitting the global computation domain into regions of equal size, keeping in mind that information is only locally known on each PE and can only be exchanged with the other PEs via message passing (which is a slower process than computing).

In the present setting the number of processors is determined at run time. Once the message passing program starts simultaneously on all assigned PEs, the parallel environment and the message passing protocol is initialised. Also, the total number of PEs is determined as well as the logical PE on which the code is run. This initialisation procedure is done in CHIEF, or any other start up main program which calls the WAM model.

Once the total number of PEs is known, MPDECOMP is called to set up an even decomposition of the total grid into one sub domain per PE. Since the global grid is mapped onto a one-dimensional sea point array following increasing latitude lines, the sub domains are chosen to be consecutive segments of the full sea point array (cf. Fig. 6.2).
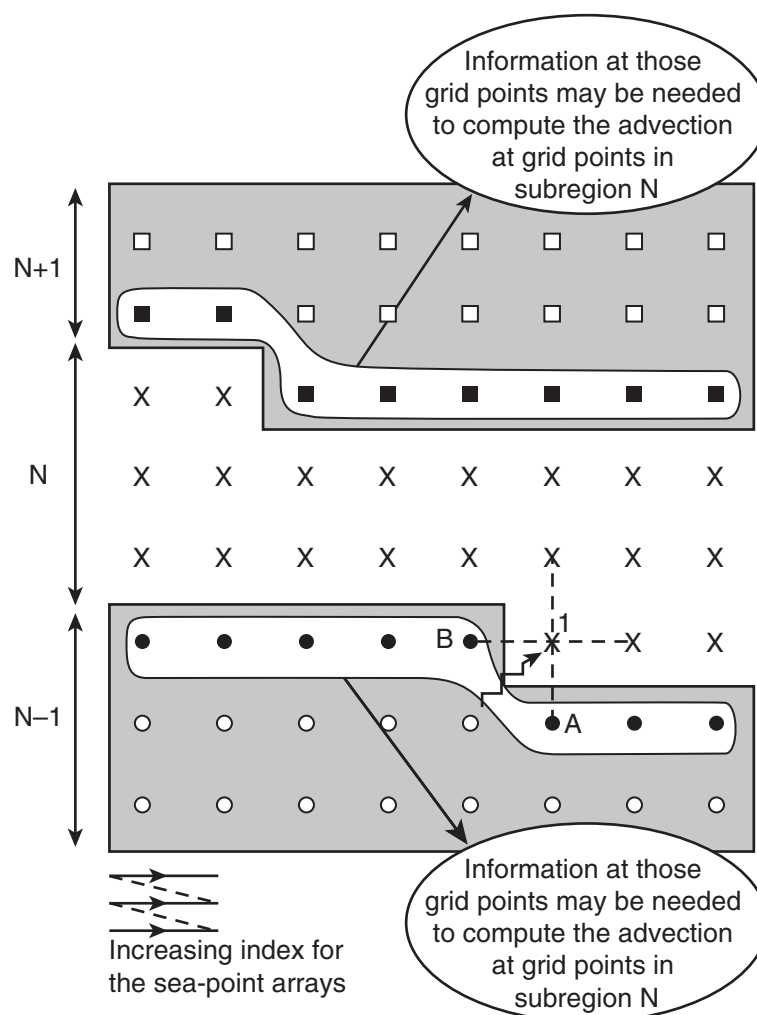

Figure 6.2 *Domain decomposition.*

The length of each segment is determined by the requirement that the work is distributed in an even manner over the given number of PEs. Thus, each PE will only perform the integration of the source functions of the

energy balance equation of one subdomain. However, the upwind scheme which solves the advection term, uses neighbouring grid points in the two-dimensional grid that might belong to another subdomain. The necessary information from the other PEs needed to evaluate the spatial derivatives of the energy flux are obtained through message passing. Here, the message is constructed using the geometrical rules displayed in Fig. 6.2, and is similar in spirit as the method that was developed for the multi-block version of the WAM model. An important difference is, however, that the domain composition is done at run time, allowing more flexibility.

6.2.2 New model decomposition for massive parallel architecture

Originally, the parallelisation of WAM was conceived for a relatively small number of processors (PEs) by keeping the number of neighbouring PEs to a minimum (see above). The actual computations in WAM are only performed for sea points. Therefore, the globe cannot be subdivided in squarish areas wrapping around the whole earth. However, it is rather straightforward to distribute the sea points in latitudinal bands, each containing the same number of points (±1) as can be seen in Fig. 6.3. It was assumed that the number of points on each PE would always be much larger than the number of points on each latitude. Hence, each PE had at most to communicate with the PE responsible of the area just above and with the PE responsible of the area just below because WAM advection scheme is only first order. However, as the number of PEs increases, the size of the message does not decrease, as information along whole latitude still needs to be exchanged (Fig. 6.4). Furthermore, if the number of PEs becomes too high, a PE will have to share information with more than two neighbouring PEs since the PE will only be responsible for a fraction of latitude. This latter fact was not taken into account at the time.

Figure 6.3 *1-D decomposition of the WAM model 0.5×0.5 irregular lat-long grid for 8 processors. The different colour lines indicate grid points sharing information with neighbouring PEs.*
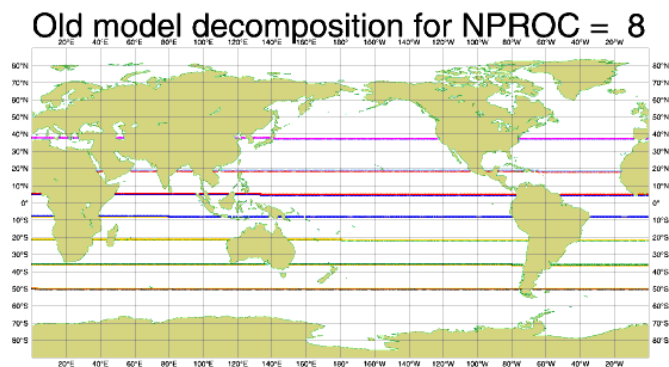

Figure 6.4 *1-D decomposition of the WAM model 0.5×0.5 irregular lat-long grid for 8 processors. The different colour lines indicate grid points sharing information with neighbouring PEs.*
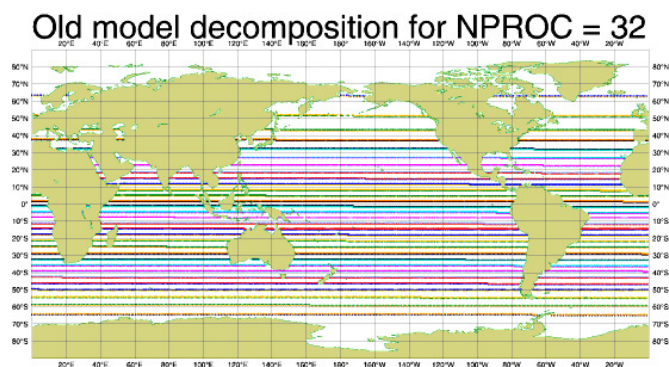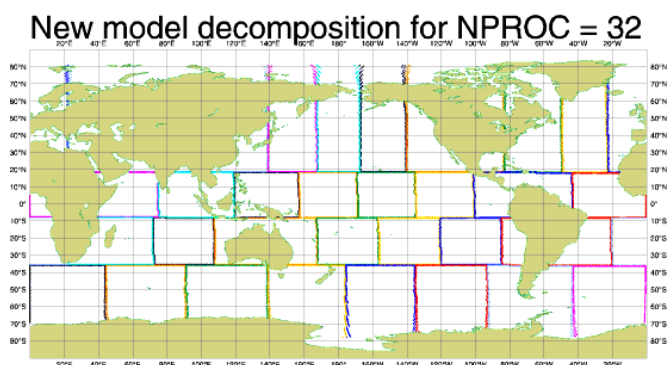
A new decomposition of the computation grid has been introduced to run the wave model on a large number of processors. It is referred to as the 2-D decomposition because the sea points are grouped in a squarish area on each processor as displayed in Fig. 6.5, as opposed to the previous 1-D decomposition where the grid points for each PE are gathered in a latitudinal band (Fig. 6.4). The choice between 1-D or 2-D decomposition is controlled by a namelist variable. Note that the assumption in the 1-D decomposition that each PE at most communicates with 2 PEs has been removed, therefore the 1-D decomposition also works when WAM is run on a large number of PEs. The perimeter of the area containing all the points on a given PE will however not decrease since the area collapses into all grid points.

When computing the 2-D decomposition, the domain is subdivided into as many sub-areas as there are PEs (NPR) in such a way that each one will contain the same number of sea points (± 1). The model grid is first divided into NY latitudinal bands. This is referred to as the first 1D-decomposition identical to the decomposition, which was used before. The second decomposition (2D) relies on a similar procedure to split each latitudinal band into sub-areas of equal number of sea points. To achieve that, the scheme finds $NYCUT$ such that there are NX sub-areas in the first $NYCUT$ latitudinal bands (starting from the southern boundary) and $NX - 1$ sub-areas in the remaining $NY - NYCUT$ bands such that

$$NPR = NYCUT \times NX + (NY - NYCUT) \times (NX - 1) \tag{6.1}$$

NX, NY, $NYCUT$ are determined by making the sub-areas as square as possible by assuming that the global extend of the domain is twice as long in the longitudinal direction than in the latitudinal direction (i.e. $NX = 2 \times NY$). Note also that in the case of the irregular lat-lon grid (as presented in the figures), the number of grid points per latitude decreases pole wards, hence the elongated appearance of the areas nearer to the poles. An example for 32 PEs is shown in Fig. 6.5 and for 512 PEs in Fig. 6.6.

This new decomposition is used both in the forward model and in the data assimilation. For the assimilation of altimeter data, the number of data per PE is limited to what is actually needed by the grid points of that PE.

Figure 6.5 *2-D decomposition of the WAM model 0.5×0.5 irregular lat-long grid for 32 processors. The different colour lines indicate grid points sharing information with neighbouring PEs.*

This completes our discussion regarding the design of the WAM model. The remainder of this chapter is devoted to the model system. A more detailed description of this may be found in the manual Wamodel cycle 4 by Günther *et al.* (1991).

The model system consists of three parts.

(i)   Pre-processing programs.
(ii) Processing programs.
(iii) Post-processing programs.

The original WAM model is designed to run as a module of a more general system or as a stand-alone program. The pre-processing programs generate the model grid, bathymetry-dependent dispersion relation, etc. Post-processing programs are provided for archiving and for further analysis of the model output.
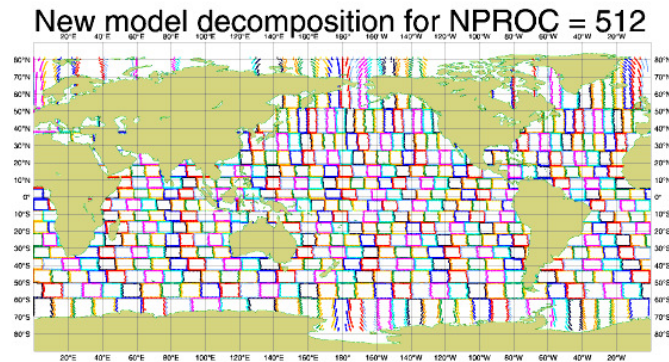
Figure 6.6 *2-D decomposition of the WAM model* 0.5×0.5 *irregular lat-long grid for 512 processors. The different colour lines indicate grid points sharing information with neighbouring PEs.*

6.3 PRE-PROCESSING PROGRAMS

Two pre-processing programs are provided.

(i) PREPROC
(ii) PRESET

The program PREPROC generates all time-independent information for the wave model. Starting from a regional or global topographic data set the model grid is created in the form required for the model. The standard model grid is a latitude-longitude grid, which may be regular or irregular, but Cartesian grids can also be chosen. Frequency, angular and group velocity arrays are generated. If the current refraction option is activated, PREPROC expects a current data set and interpolates the data onto the model grid. A number of model constants and matrices, such as the surface stress as a function of wind speed and wave-induced stress, are pre-computed and stored together with the model grid, frequency and angular information and the currents in two output files. If nested grids are generated, the information for the output, input and interpolation of boundary spectra are presented and stored in separate files for the coarse and fine mesh models.

PRESET generates an initial wave field for a wave model cold start in the event that no appropriate initial conditions are available. Controlled by the user input of PRESET, either the same initial JONSWAP spectrum is used at all ocean grid points, or the initial spectra are computed from local initial winds, according to fetch laws with a $\cos^2$ directional distribution.

6.4 PROCESSING PROGRAMS

There are two processing programs.

(i) CHIEF
(ii) BOUINT

The program BOUINT is used for nested grids. It interpolates, in time and space, the output spectra from a coarse grid model run onto the fine grid along the boundaries of the coarse and fine grids.

CHIEF is the shell program of the stand-alone version of the the wave model which calls the subroutine version WAVEMDL of the wave model. All time-dependent variables and user-defined parameters are set, the wind fields are transformed to the wave model grid, and the transport equation is integrated over a chosen period. The program uses the output files of PREPROC as set-up files and the files generated by PRESET or a previous model run as initial values. A wind input file has to be provided by the user. All additional information must be defined in the user input file. The model can be integrated with independently chosen propagation, source term and wind time steps, under the restriction that all time step ratios must be an integer, or the inverse of an integer.

A number of model options and parameters may be selected by the user in the program input. The following model options are implemented.

(i)   Cartesian or spherical propagation.
(ii) Deep or shallow water.
(iii) With or without depth refraction or with depth and current refraction.
(iv) Nested grids.
(v)   Time interpolation of winds, or no time interpolation.
(vi) Model output at regular intervals, or through a list.
(vii) Printer and/or file output of selected parameters.

All run-time-dependent files are fetched dynamically and follow a fixed file name convention. The user has control over directory names and paths through the model input. If selected, model results are saved in four files. These files contain the following.

(i)   Gridded output fields of significant wave height, mean wave direction, mean frequency, friction velocity, wave direction, peak frequency, drag coefficient and normalized wave-induced stress.
(ii) Gridded output field of swell parameters such as wave height, swell direction, mean wind-wave direction and mean swell frequency.
(iii) Spectra at selected grid points.
(iv) Swell spectra at selected grid points.

A comprehensive view of the program CHIEF, which is clearly the most important part of the model system, is given in the flow chart of Fig. 6.7. We need not discuss details here and only highlight the main points. The subroutine INITMDL is only called once. It reads the necessary input generated by PREPROC and PRESET (or by a previous model run) and sets up the necessary information for the model run. PREWIND deals with reading of the winds provided by the user and the transformation to the wave model grid. If required, time interpolation is performed. Furthermore, the subroutine WAMODEL integrates the energy balance equation. The physics of the wave model is contained in the subroutines PROPAGS and IMPLSCH which are called in a loop over the blocks of the wave model grid. PROPAGS deals with propagation and refraction, whereas IMPLSCH performs the implicit integration in time of the source terms S_{in} (SINPUT), S_{nl} (SNONLIN), S_{ds} (SDISSIP) and S_{bot} (SBOTTOM). The remaining subroutines in WAMODEL are related to the generation of output files or restart files. Finally, the subroutine WAMASSI assimilates Altimeter wave height data according the optimum interpolation method described in Chapter 4. The quality control and the correction of the data is performed by the subroutine GRFIELD, while the increments according to OI method are determined in OIFIELD use the subroutine ANALYSE. Using scaling laws of swell and wind-wave generation the wave spectra and the surface winds are updated in UPDATE.

As an example of the capabilities of ECWAM, Fig. 6.8 shows the area of St. Andrew Bay, in North West Florida, where wind and waves were observed from a buoy as it drifted out to the Gulf of Mexico. The bathymetry at a scale of the order 100m is also shown. ECWAM was setup with this bathymetry on a 0.001 degree grid, and forced with the observed winds from the buoy. The buoy was deployed at dawn, as the morning winds were picking up (Hwang and Wang (2004)). The resulting wave height after one hour is shown in Fig. 6.9 as well as the wave heights along the trajectory of the buoy. Compared to the buoy observations, the agreement with the model hindcasts is quite satisfactory.
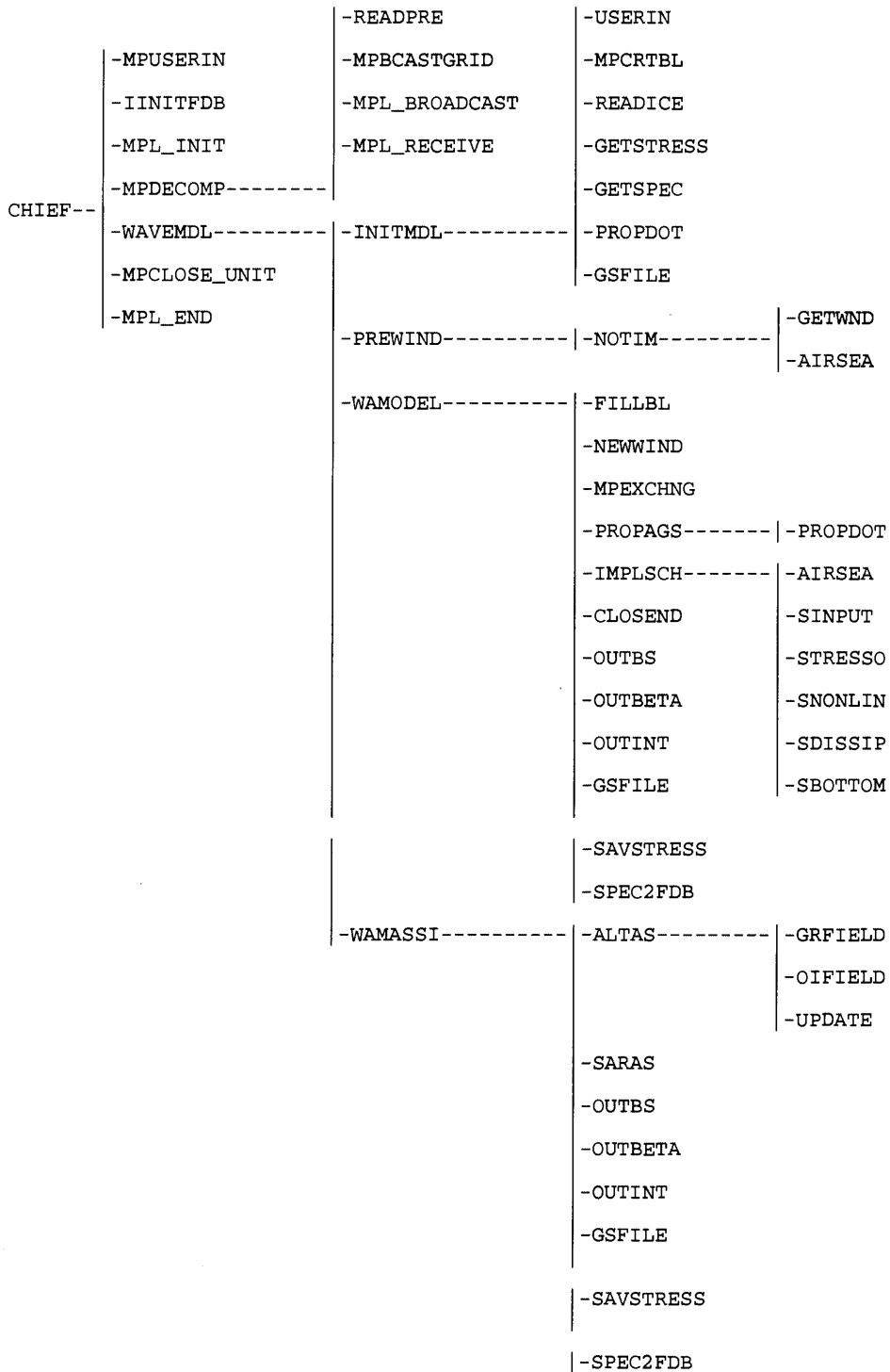
```
                                   -READPRE           -USERIN

                     -MPUSERIN     -MPBCASTGRID       -MPCRTBL

                     -IINITFDB     -MPL_BROADCAST     -READICE

                     -MPL_INIT     -MPL_RECEIVE       -GETSTRESS

                     -MPDECOMP--------|                -GETSPEC
         CHIEF--
                     -WAVEMDL---------|-INITMDL----------|-PROPDOT

                     -MPCLOSE_UNIT                      -GSFILE

                     -MPL_END
                                                                    -GETWND
                                   -PREWIND----------|-NOTIM---------|
                                                                    -AIRSEA

                                   -WAMODEL----------|-FILLBL

                                                      -NEWWIND

                                                      -MPEXCHNG

                                                      -PROPAGS-------|-PROPDOT

                                                      -IMPLSCH-------|-AIRSEA

                                                      -CLOSEND        -SINPUT

                                                      -OUTBS          -STRESSO

                                                      -OUTBETA        -SNONLIN

                                                      -OUTINT         -SDISSIP

                                                      -GSFILE         -SBOTTOM


                                                      -SAVSTRESS

                                                      -SPEC2FDB

                                   -WAMASSI----------|-ALTAS---------|-GRFIELD

                                                                     -OIFIELD

                                                                     -UPDATE

                                                      -SARAS

                                                      -OUTBS

                                                      -OUTBETA

                                                      -OUTINT

                                                      -GSFILE


                                                      -SAVSTRESS

                                                      -SPEC2FDB
```

Figure 6.7 *Flow chart of program* CHIEF.

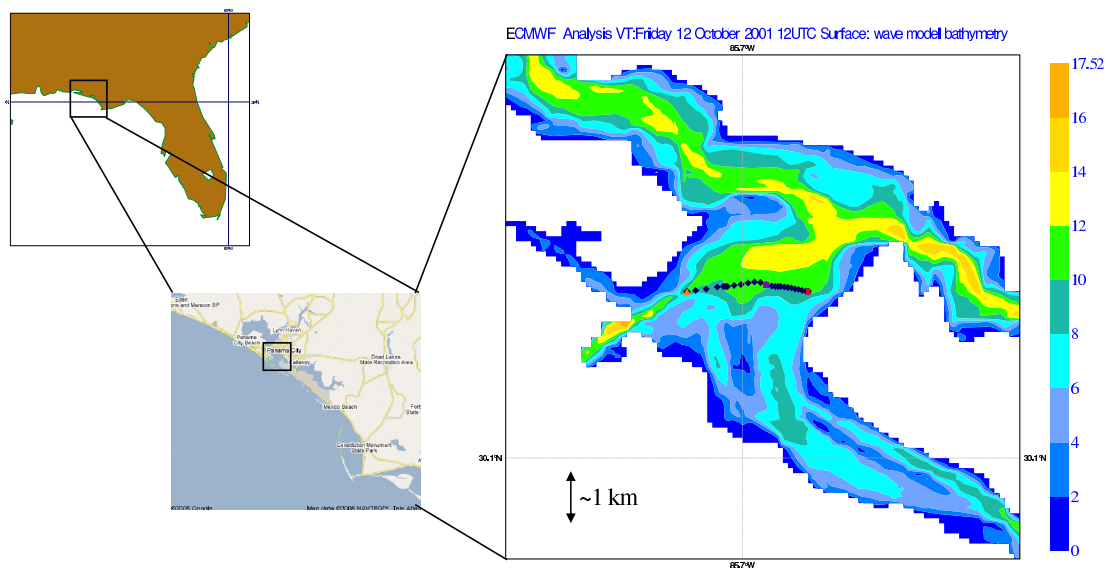## Very small scale example: St. Andrew Bay, Florida

Figure 6.8 *St. Andrew Bay bathymetry and trajectory of the drifting buoy where wind and waves were observed.*
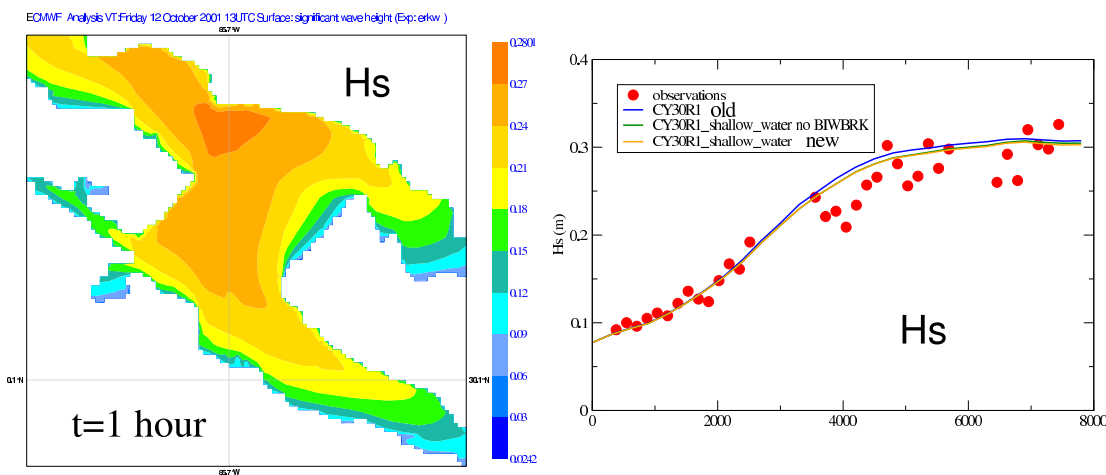
St. Andrew Bay

Figure 6.9 *Simulated significant wave height in St. Andrew Bay at 1300 UTC on 12 October 12 (left panel) (one hour from the start of the run). Temporal evolution (in seconds) of significant wave height along the trajectory of the drifting buoy (right panel). The observations are shown with the red dots and the solids lines are the model simulations with the old Snl (blue line), the new Snl without depth induced wave breaking (green) and with it (orange).*

Chapter 7

Wind wave interaction at ECMWF

In this chapter we briefly describe how wave forecasts are validated and the way we apply wave forecasting at ECMWF.

An important task of any weather centre is the verification of the forecast. We routinely verify analysed and forecast wave products against buoy data, and forecast wave height against the analysis. An example of forecast validation over the northern and the southern hemisphere is given in Fig. 7.1. A more detailed discussion of the quality of the ECMWF wave forecast is given by Janssen et al. (1997, 2000). Furthermore, we have been validating extensively the quality of wave products from Altimeter and SAR from ERS1/2 and will do so from ENVISAT which will be launched in the middle of 2001. An account of this work may be found in Hansen and Günther (1992), Janssen et al. (1997), Janssen (2000) and Janssen (2004). More recent figures can be found online at the wave verification page

Following the work of Janssen (1982, 1989, 1991) on the feedback of ocean waves on the airflow we have made a dedicated effort towards an integrated forecasting system for our geosphere. Ultimately, it is expected to have a model consisting of the atmosphere and the oceans where the ocean waves are the agent that transfer energy and momentum across the interface in accordance with the energy balance equation. This role of the ocean waves is illustrated in Fig. 3.6 and Fig. 3.7. On the one hand ocean waves receive momentum and energy from the atmosphere through wind input (hence they control to a large extent the drag of airflow over the oceans), while on the other hand, through wave breaking, the ocean waves transfer energy and momentum to the ocean, thereby feeding the turbulent and large scale motions of the oceans. Ocean waves are in general not in an equilibrium state determined by a balance of the three source functions, because advection and unsteadiness are important as well. Typically, of the amount of energy gained by wind about 90% is lost locally to the ocean by wave breaking, while the remaining 10% is either advected away or is spent in local growth.

Presently, we have taken the first step by coupling the IFS atmospheric model with the WAM model in a two-way interaction mode. This coupled model provides the ten-day weather and wave forecast since the 29 June 1998. Here, every coupling time step the surface winds are passed through the WAVEMDL interface towards the wave model, while the Charnock parameter as determined by the sea state (cf. equation (3.12)) is given to the atmospheric model and is used to estimate the slowing down of the surface winds during the next coupling time step. An overview of results is given by Janssen et al. (2001) who show that the introduction of two-way interaction gives improvements in the prediction of surface winds and waves. As a next step ECMWF is developing a coupled atmosphere, ocean-wave, ocean-circulation model. A first version of this coupled model is already used in the Centre's seasonal forecasting and monthly forecasting suites.

Since December 1992 ECMWF is providing estimates of forecast error by running an ensemble prediction system. With the introduction of the coupled wind-wave prediction scheme in June 1998, ensemble wave products became available as well. This new product may provide useful information on the uncertainty in the sea state prediction (Saetra and Bidlot, 2002, 2004), which could be applied among other things to ship routes (Hoffschildt et al., 1999; Saetra, 2004).

As described in Chapter 3, the coupling between the IFS and WAM was extended to include air density and gustiness effects on the wave growth. This change became operational in April 2002 (Cy25r1). Finally, the flexibility of the coupling interface between the two models was further extended to provide WAM with 10m neutral winds instead of the usual 10m winds since WAM cycle 4 was derived in term of friction velocity with the neutral logarithmic profile. This latest change was part of Cy28r1, implemented in operations in March 2004.
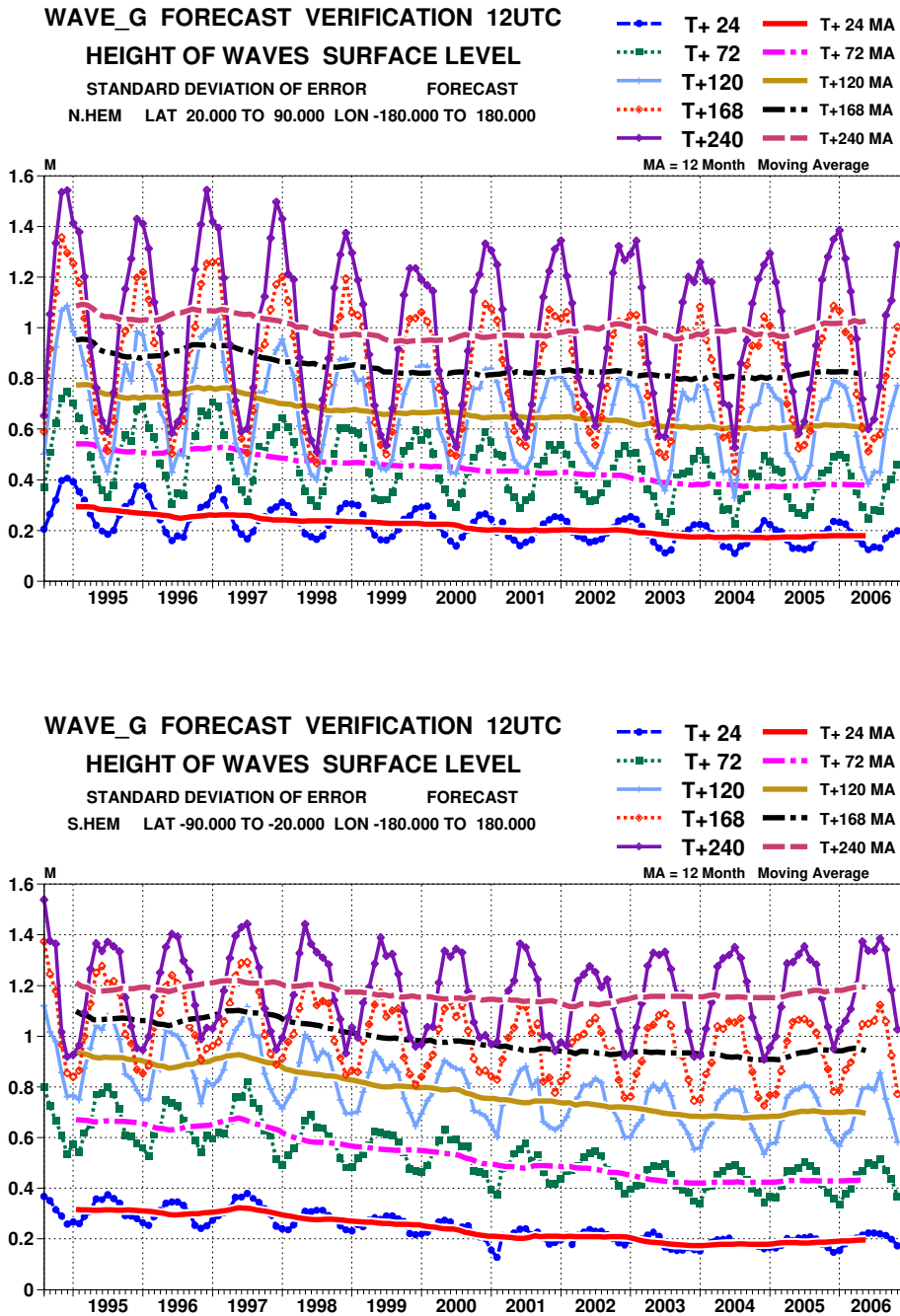
Figure 7.1 *Standard deviation of wave height error of day 1, 3, 5, 7 and day 10 wave forecasts. Here, the wave forecasts are validated against the wave analyses, and the period is August 1994 until November 2006.*

Chapter 8

Extreme wave forecasting

This section contains the different versions of the extreme wave forecasting system The most recent one was implemented with CY46R1 (June 2019) (see below).

Table of contents

8.1 SYSTEM BEFORE CY41R1

This chapter will be updated with the updates to the freak wave warning system once **?** is published.

In this chapter we shall briefly discuss how the sea state as described by the two-dimensional wave spectrum may provide information on the occurrence of extreme waves. The information that can be extracted is necessarily of a probablistic nature as in the context of operational wave forecasting there is no knowledge of the phases of the waves at the location and time of interest.

8.1.1 Determination of the surface elevation pdf

The parameters that have been described so far all provide information on the average properties of the sea state. In recent years there has been a considerable effort in order to understand extreme events such as freak waves. An individual wave is regarded as a freak wave when its height is larger than twice the significant wave height. Clearly, in order to be able to describe such extreme events, knowledge on the statistical properties of the sea surface is required. Janssen (2003) has presented a general framework that relates the shape of the probability distribution function (pdf) of the surface elevation to the mean sea state as described by the two-dimensional frequency spectrum. Under normal circumstances, the surface elevation pdf has approximately a Gaussian shape, but in the exceptional circumstances that the waves are sufficiently nonlinear and that the wave spectrum is narrow in **both** frequency and direction considerable deviations from Normality may occur, signalling increased probability for freak waves.

The deviations from Normality are measured in terms of the kurtosis C_4 of the surface elevation pdf. With η the surface elevation we use as kurtosis definition

$$C_4 = \frac{\langle \eta^4 \rangle}{3\langle \eta^2 \rangle^2} - 1 \tag{8.1}$$

According to the theory of wave-wave interactions the kurtosis is related to the frequency spectrum $E(\omega, \theta)$ by

$$C_4 = \frac{4g}{m_0^2} \mathcal{P} \int d\omega_1 d\omega_2 d\omega_3 d\theta_1 d\theta_2 d\theta_3 T_{1,2,3,4} \sqrt{\frac{\omega_4}{\omega_1 \omega_2 \omega_3}} \frac{E_1 E_2 E_3}{\Delta \omega} \tag{8.2}$$

where

$$\omega_4 = \Omega(\mathbf{k}_4) = \sqrt{g|\mathbf{k}_1 + \mathbf{k}_2 - \mathbf{k}_3|} \tag{8.3}$$

while $\Delta\omega = \omega_1 + \omega_2 - \omega_3 - \omega_4$, and $T_{1,2,3,4}$ is a complicated, homogeneous function of the four wave numbers $\mathbf{k}_1, \mathbf{k}_2, \mathbf{k}_3, \mathbf{k}_4 = \mathbf{k}_1 + \mathbf{k}_2 - \mathbf{k}_3$ (the last condition expresses the four-wave resonance condition in wavenumber space). In addition, the angular frequency $\omega(\mathbf{k})$ obeys the dispersion relation $\omega(\mathbf{k}) = \sqrt{gk}$, with k the magnitude of the wavenumber vector $\mathbf{k}$. Finally, the symbol $\mathcal{P}$ denotes the principle value of the integral. The integrand contains a singularity in wave number space at $\Delta\omega = 0$, and the principle value integral simply means that one makes in the integration contour a cut of size 2ϵ around the singularity in a symmetrical fashion, and the limit $\epsilon \to 0$ is taken afterwards.

For operational implementation the expression for the kurtosis, as derived in (8.2) is far too involved, and clearly some simplification is desirable. Freak wave events most likely only occur for narrow band wave trains. This corresponds to situations where both the frequency and angular distribution of the waves are narrow. In the narrow-band approximation it is possible to simplify and evaluate the six-dimensional integral. In the previous operational system, the dependence on angular width was ignored, resulting in an expression for the kurtosis which depends on the square of the BFI. However, from experimental evidence (Waseda, 2006) and numerical simulations (Onorato and Mori, private communication 2006), it is known that kurtosis also depends in a sensitive manner on the angular width. Therefore, an extension of the kurtosis calculation has been obtained, and the sensitive dependence on the angular width is confirmed.

The general result for the kurtosis and its relation to the wave spectrum was originally derived for deep-water waves, but Janssen and Onorato (2007) have shown how to extend it to shallow water. For narrow-band spectra, it is then straightforward to parametrize the stabilizing effects of shallow water.

Before we start with a detailed calculation of the kurtosis of the sea surface and its dependence on the wave spectrum, we briefly mention the starting point of ocean waves dynamics, which is the Hamiltonian formulation of the nonlinear water wave equations. Next, assuming that the waves are weakly nonlinear and applying a *canonical* transformation which removes most of the contributions by non-resonant interactions, one arrives at the well-known Zakharov equation (Zakharov, 1968) for the free wave part of the action variable. The properties of the Zakharov equation have been studied in great detail by, for example, D. R. Crawford and Yuen (1981) for deep-water waves and by Janssen and Onorato (2007) for shallow-water waves. It describes all the known properties of weakly nonlinear waves in deep and shallow water and is therefore a good starting point for further analysis.

Based on the above theoretical development it should be clear that the expression of the kurtosis of the pdf of the surface elevation consists of two additive contributions. The first one was derived by Janssen (2003) and reflects the effects of resonant and non-resonant four-wave interactions, while the second contribution stems from the canonical transformation and reflects the contribution from asymmetries in the shape of the waves. However, the contribution of the canonical transformation gives a very lengthy expression of several pages and only for narrow band wave trains its form is known explicitly.

Based on results from numerical simulations of the Nonlinear Schrödinger equation, which follows from the narrow-band limit of the Zakharov equation, Mori and Onorato found the following fit for the maximum of the kurtosis

$$C_4^{dyn} = \frac{0.031}{\delta_\theta} \times \frac{\pi}{3\sqrt{3}} BFI^2, \tag{8.4}$$

where the Benjamin-Feir Index BFI is given by

$$BFI = \frac{\epsilon \sqrt{2}}{\delta_\omega}. \tag{8.5}$$

with ϵ the integral steepness parameter, $\epsilon = k_0\sqrt{m_0}$, k_0 the peak wave number, m_0 the zero moment of the spectrum and δ_ω the relative width of the frequency spectrum. Therefore, finite directional width δ_θ is seen to give a considerable reduction in kurtosis C_4^{dyn}. If we include the contribution from the shape of the waves, the total kurtosis becomes now

$$C_4 = C_4^{dyn} + \alpha\epsilon^2. \tag{8.6}$$

where for deep-water $\alpha = 6$.

This result holds for deep-water waves. The extension to shallow water is achieved by means of a redefinition of the Benjamin-Feir Index.[1] Recall (see Janssen (2003)) that this dimensionless parameter just expresses the balance between nonlinearity and dispersion. For the general, shallow water case this gives a new parameter which is called B_S. It is defined as (Janssen and Onorato, 2007)

$$B_S^2 = -BFI^2 \times \left(\frac{v_g}{c_0}\right)^2 \frac{gX_{nl}}{k\omega_0\omega_0''}, \tag{8.7}$$

where the relevant symbols are defined in (3.47) to (3.51).

The extension of the kurtosis calculation towards shallow water is now simply achieved by replacing in (8.4) BFI^2 by B_S^2. Note that in the deep-water limit it can readily be shown that the second part of the expression for B_S^2 becomes -1, therefore in this limit B_S^2 reduces to the usual definition for the BFI (compare with (8.5)). Studying now the dependence of B_S^2 on depth it is seen that for decreasing dimensionless depth k_0D the square of the Benjamin-Feir index is slowly decreasing until around $k_0D = 1.363$ when there is a rapid transition from positive to negative values. Hence for $k_0D < 1.363$ the kurtosis may become negative which implies that there are less extreme events than the norm, while in the opposite case there are more frequent extreme events.

The estimation of the Benjamin-Feir Index requires knowledge of the significant steepness ϵ and the spectral width δ_ω in frequency space. In addition, an estimate of the directional width δ_θ is required as well. In Cy33r1, it was decided to fit the one-dimensional frequency and directional spectra with a parabola thus giving sharp estimates for δ_ω and δ_θ. In fitting the parabola also a sharper estimate of the peak period T_p may be provided as up to now the peak period did correspond to the maximum of the one-dimensional frequency spectrum so T_p could only assume discrete values because of the discretization of the wave spectrum in frequency space.

8.1.2 Maximum wave height and period.

Here, we would like to introduce a simple measure for extreme sea states. It is common to define as a freak wave a wave whose height is at least twice the significant wave height. This is a very discrete and singular approach, which is in practice not easy to verify. Nevertheless, we would like to be able to quantify extreme sea states and to be able to validate them against observations in a meaningful manner. This led us to consider the concept of maximum wave height, a concept which is well-known in engineering practice. For example, Stansell (2005)) uses the ratio of maximum wave height and significant wave height as a useful indicator for the occurrence of freak waves. Typically, this ratio is of the order 1.5-2 but he reported cases with a ratio as large as 3. It should be realized, as also pointed out extensively by Mori and Janssen (2006), that the maximum waveheight H_{max} not only depends on the shape of the probability distribution function of the sea surface, but also on the number of waves at hand. Consider now a time series of significant wave height of length T involving a number of N waves. A good estimate of the maximum wave height is the expectation value for maximum wave height denoted by $\langle H_{max}\rangle$. As an extension of Goda's work for Gaussian sea states, we will determine $\langle H_{max}\rangle$ for a pdf with finite kurtosis and we will compare the result with observations of maximum wave height from buoys. The agreement is good, and therefore we have introduced this measure for maximum wave height into the operational ECMWF wave forecasting system.

In order to obtain an expression for the expectation value of maximum wave height the work of Mori and Janssen (2006) is followed closely. One may then proceed as follows

- Start from the pdf of surface elevation η, which is the well-known Gram-Charlier expansion, i.e. pdf depends on skewness and kurtosis, which are assumed to be small.

---

[1] Also the parameter α needs adjustment for the shallow water case. However, this depth-dependence has not been introduced yet operationally as it was only recently obtained by Janssen (2008). So in Cy33r1 α has the value 6.

- Obtain the pdf of 'wave height' defined as twice the envelope. Here the envelope ρ follows implicitly by writing the surface elevation signal as

$$\eta = \rho \cos \phi$$

  with ϕ the local phase of the wave train. Local wave height is then defined as $H = 2\rho$ and the wave height distribution in terms of wave height normalized with the significant wave height becomes:

$$p(H) = 4H \exp(-2H^2)\left[1 + C_4 A_H(H)\right] \tag{8.8}$$

  where

$$A_H(H) = 2H^4 - 4H^2 + 1$$

  Note that because of symmetries the pdf of H does not contain skewness.

- The maximum wave height distribution is obtained by simply writing down the probability that for given number of waves the maximum wave height has a certain chosen value. The maximum wave height distribution $p_m(H_{max})$ becomes

$$p_m(H_{max}) = N\left[1 - P(H_{max})\right]^{N-1} p(H_{max})$$

  where, with $B_H(H) = 2H^2\left(H^2 - 1\right)$,

$$P(H) = \int_H^\infty \mathrm{d}h\, p(h) = \exp(-2H^2)\left(1 + C_4 B_H(H)\right)$$

  is the exceedence probability of wave height, N is the number of waves, and $p(H_{max})$ follows from Eq. (8.8). In the continuum limit this becomes

$$p_m(H_{max}) = Np(H_{max}) \times \exp\left[-NP(H_{max})\right]$$

  Notice that the maximum wave height distribution involves a double exponential function.

- The expectation value of maximum wave height follows from

$$\langle H_{max} \rangle = \int_0^\infty \mathrm{d}H_{max}\, H_{max}\, p_m(H_{max}) \tag{8.9}$$

  Notice that $H_{max} = F[C_4(BFI, \delta_\theta), N]$, where $N = T_D/T_p$ with T_p the peak period and T_D the duration of the timeseries.

The integral in (8.9) may be evaluated in an approximate fashion for large N and small C_4. The main result becomes

$$\langle H_{max} \rangle = \sqrt{\langle z \rangle}, \tag{8.10}$$
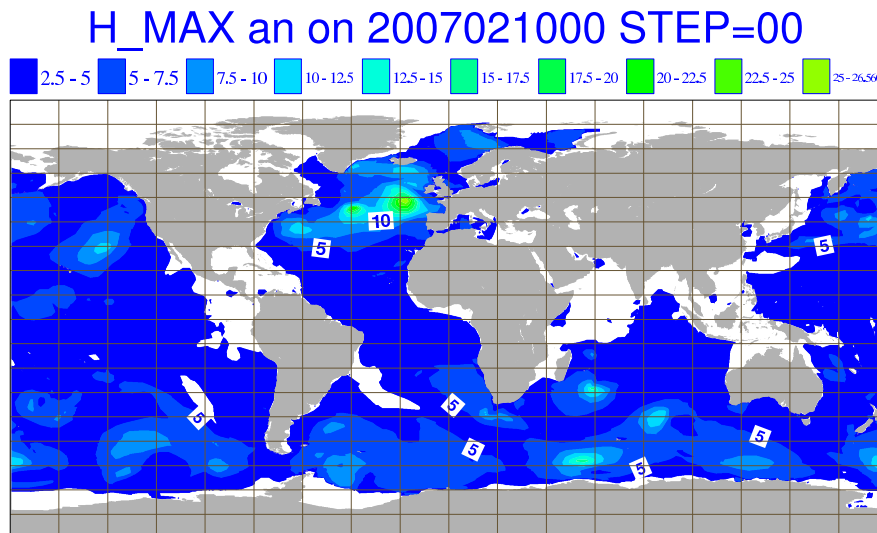
where

$$\langle z \rangle = \hat{z}_0 + \frac{\gamma}{2} + \frac{1}{2} \log\left[1 + C_4\left\{2\hat{z}_0(\hat{z}_0 - 1) - \gamma(1 - 2\hat{z}_0) - \frac{1}{2}(\gamma^2 + \frac{\pi^2}{6})\right\}\right], \tag{8.11}$$

with $\hat{z}_0 = \frac{1}{2}\log N$ and $\gamma = 0.5772$ is Euler's constant.

Fig. 8.3 shows an example of a maximum wave height map for a big storm in the North Atlantic that occurred on 10 February 2007. Here, the maximum wave height refers to time series with a duration T_D of 20 minutes and the number of waves N follows from the relation $N = T_D/T_p$. The maximum of significant wave height in the North Atlantic was 15.9 m at that time while the extreme value in maximum wave height is found to be 26.5 m. Notice, however, the dependence of the estimate of the maximum wave height on the number of waves in the time series of duration T_D. Although according to (8.10) it only depends on the logarithm of N, nevertheless for $T_D = 3$ hours the maximum wave height will increase on average by about 20% giving an extreme value of 31.6 m.

Figure 8.1 *Map of analyzed maximum wave height for 10 February 2007.*

It is clear that for operational applications a choice for the length of the timeseries needs to be made. Buoy time series are typically 20–30 minutes long so initially it was thought that, in order to validate the model results against buoy data, it would make sense to take this period as the length of the time series. However, for practical application a timescale related to the changes in the synoptic conditions seems more appropriate. This would mean a much longer duration of say 3 hours. A compromise was found by choosing a duration of 3 hrs, while for validation purposes we collected 6 consecutive hourly buoy observations making up an observed duration of 2–3 hours.[2] The observed maximum wave height is then the maximum of the 6 consecutive maximum wave height observations. First results of a comparison of modelled and observed maximum wave height are shown in Fig. 8.4. For a first comparison the agreement between modelled and observed maximum wave height is impressive. The relative positive bias is about 7% while the scatter index is about 19%. For comparison the scatter index for significant wave height for the same set of buoys and period is about 13%. We were puzzled about this impressive agreement, because for starters we are actually comparing apples and pears, since the model value is an expectation while the buoy value is instantaneous. This puzzle was solved when it was realized that the pdf of maximum wave height is fairly narrow. For linear waves its width σ is approximately

$$\frac{\sigma}{\langle H_{max} \rangle} \simeq \frac{\pi}{2\sqrt{6} \left(\log N + \frac{1}{2}\gamma \right)}. \tag{8.12}$$

Clearly, the longer the length of the time series the sharper the estimate of maximum wave height becomes. For a 3 hour duration and a peak period of 10 s one finds $\sigma/\langle H_{max} \rangle \simeq 0.08$, therefore the maximum wave height distribution is indeed fairly narrow.

In closing this Section, we give the corresponding maximum period, which is the average period for given maximum wave height. So far we have only done work on the case of linear waves, so this still requires extension into the nonlinear regime. The period is estimated using the joint pdf of normalized envelope (c.f. (Longuet-Higgins, 1983)),
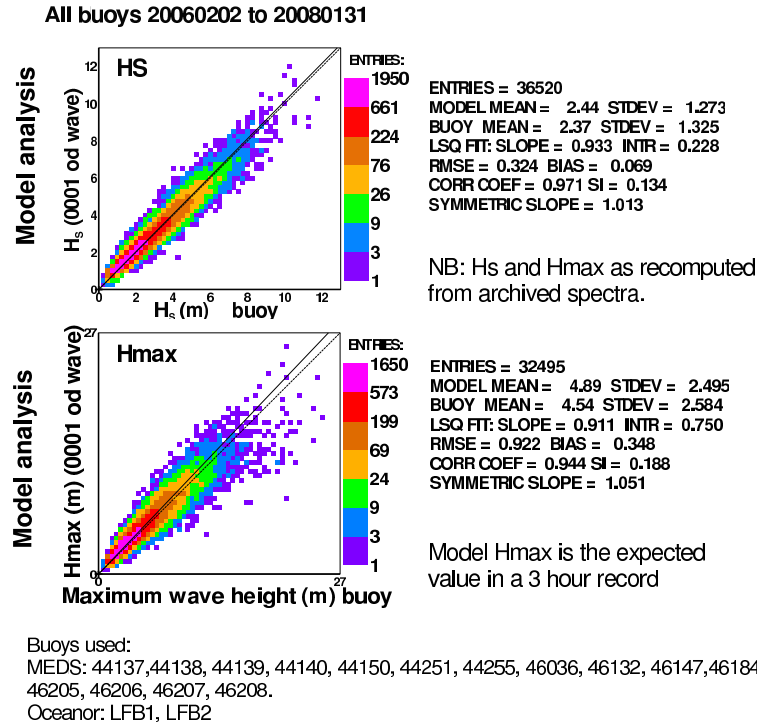
$$R = \frac{\rho}{\sqrt{2m_0}},$$

and normalized period

$$T = \frac{\tau}{\bar{\tau}},$$

---

[2]Note that the difference between a duration of 2 or 3 hours only gives a difference of 3% in maximum wave height, so this difference will be disregarded for the moment.

Figure 8.2 *Validation of analyzed maximum wave against observed maximum wave height from a number of buoys that report maximum wave height (the buoy list is shown as well). Period is February 2006 until January 2008.*

where the period $\tau = 2\pi/\omega = -2\pi/\dot{\phi}$, and the mean period $\overline{\tau} = 2\pi m_0/m_1$. This joint pdf reads

$$p(R, T) = \frac{2}{\nu\pi^{1/2}}\frac{R^2}{T^2}\exp\left\{-R^2\left[1 + \frac{1}{\nu^2}\left(1 - \frac{1}{T}\right)^2\right]\right\},$$

where ν is the width parameter as introduced by Longuet-Higgins (1983),

$$\nu = (m_0 m_2/m_1^2 - 1)^{1/2}.$$

For given normalized envelope height, wave period follows from the conditional distribution of wave periods $p(T|R) = p(R, T)/p(R)$. One finds

$$p(T|R) = \frac{R}{\nu\pi^{1/2}T^2}\exp\left[-\frac{R^2}{\nu^2}\left(1 - \frac{1}{T}\right)^2\right],$$

The expectation value of the period then becomes

$$\langle T \rangle = \frac{R}{\nu\pi^{1/2}}\int_{-\infty}^{\infty}\frac{\mathrm{d}T}{T}\exp\left[-\frac{R^2}{\nu^2}\left(1 - \frac{1}{T}\right)^2\right].$$

Introducing the parameter $\Delta = \nu/R$ the above integral may be evaluated for small Δ in an approximate fashion. One finds

$$\langle T \rangle = 1 + \frac{1}{2}\Delta^2 + \frac{3}{4}\Delta^4 + ...,$$

and the maximum period then follows from $\tau_{max} = \overline{\tau}\langle T \rangle$ and $\rho = H_{max}/2$.

8.2 SYSTEM SINCE CY41R1 BUT BEFORE CY46R1

This chapter should be updated with the updates to the freak wave warning system as described in Janssen (2015b).

8.3 SYSTEM SINCE CY46R1 (JUNE 2019)

Based on shallow-water parametrizations of envelope skewness and kurtosis of the sea state, an improved version of the ECMWF Freak Wave warning system has been developed. Although in Janssen (2017) a detailed discussion of the parametrization work has been given we briefly summarize the results here, and introduce a new parametrization of dynamic kurtosis developed by A.E.M. and Janssen (2019). Preoperational results regarding e.g. maximum wave height and its prbability density function or the dependence of the extreme statistics on the on wave age, which is a measure of the sea state development, are presented.

8.3.1 Introduction.

Here I report the latest work on the operational implementation of a new version of the Freak Wave warning system. The scientific brackground is discussed in detail in Janssen (2017). Here, we present a slightly simpler version, which only uses two measures of the relative frequency width, one called δ_ω which is related directly to the generation of sidebands by the Benjamin-Feir instability while and one called ν which estimates the damping of the Benjamin-Feir instability by the incoherent part of the wave spectrum.

8.3.2 Definition of some important parameters.

The parametrisations for bound skewness and kurtosis and the free-wave kurtosis have been guided by known results for a narrow-band wave train (see e.g. Janssen (2017)). Nevertheless the wave spectrum is normally fairly broad-banded and its effect will be incorporated by introducing a characteristic wave number $\bar{k}$ and a measure for angular width and two measures for relative frequency width.

It is noted that it is important to choose as wavenumber a characteristic wavenumber that reflects that the wave spectrum is broad-banded. As a first guess I tried to choose a characteristic wavenumber $\bar{k}$ that follows from the inverse of the dispersion relation $a\bar{\omega} = \omega(\bar{k}, h)$, where $\bar{\omega} = m_0/m_{-1}$ and a is a tuning parameter. Results for skewness and kurtosis are very sensitive to the choice of this tuning parameter. In the end I settled for the choice $a = 0.89$ which, for deep-water waves, implies that the characteristic wavenumber $\bar{k}$ is larger by about 20% when compared to the peak wavenumber k_p. Thus, in the formulae for skewness and kurtosis, for example, the peak wave number k_0 which occurs in the known narrow-band results for these statistical parameters is replaced by $\bar{k}$, while, to be consistent, this is also done for all wave number dependent factors in the dynamic kurtosis parametrisation.

It is by now well-known that the severity of the sea state is connected to the coherency of the sea state. A narrow-band wave train which has small frequency width and even smaller angular width is prone to be unstable to sideband perturbations and therefore has the potential to generate freak waves. For this reason angular width and relative frequency width of the spectrum need to be defined. In addition, freak waves are more likely to be generated when the sea state is sufficiently nonlinear.

An important parameter that measures nonlinearity is the significant steepness ϵ which is defined as,

$$\epsilon = \bar{k}\sqrt{m_0}, \tag{8.13}$$

where instead of the peak wavenumber we use $\bar{k}$ and m_0 is the zeroth moment of the wave spectrum. In general, the moments are defined as

$$m_n = \int \mathrm{d}f \, f^n E(f), \; n = -1, 0, 1, 2 \tag{8.14}$$

with $E(f)$ the frequency spectrum, and typically we need the moments for $n = -1, 0, 1, 2$.

The coherency of the sea state is measured by angular width and relative frequency width. Here, the angular width is determined using frequency averaged moments

$$\overline{m}_0 = \int_{\omega_p - \Delta\omega}^{\omega_p + \Delta\omega} \mathrm{d}\omega \int \mathrm{d}\theta F(\omega, \theta), \; \overline{m}_1 = \int_{\omega_p - \Delta\omega}^{\omega_p + \Delta\omega} \mathrm{d}\omega \int \mathrm{d}\theta \cos(\theta - \overline{\theta}) F(\omega, \theta), \tag{8.15}$$

where $\Delta\omega = \omega/2$, and the measure of angular width becomes

$$\delta_\theta = \sqrt{2\,(1-R_1)},\ R_1 = \overline{m}_1/\overline{m}_0 \tag{8.16}$$

Furthermore, the damping of the Benjamin-Feir instability is determined by the broad-band aspects of the frequency spectrum. To this end we use the relative frequency width given by a measure introduced by Longuet-Higgins (1983),

$$\nu_\omega = (m_0 m_2/m_1^2 - 1)^{1/2} \tag{8.17}$$

where m_n are the moments of the frequency spectrum. In the Section on free waves we will use another measure of relative frequency width, called δ_ω, which is related to Goda's peakedness parameter Q_p. This measure emphasizes the peak region of the spectrum, which is thought to play an important role in the development of the Benjamin-Feir Instability.

8.3.3   Statistical Parameters for Freak Wave detection.

Following Janssen (2014) the time series analysis is based on properties of the envelope wave height. In this reference, it is shown that this method gives an accurate estimation of the joint p.d.f. of wave height and period for linear waves and that it is possible to extend the approach into the weakly nonlinear regime. Of course, such an approach has certain limitations, for example the envelope method cannot make a distinction between a wall of water and a hole in the sea, but it certainly can indicate that something extreme will happen.

Janssen (2014) has obtained the following envelope wave height distribution for a weakly nonlinear sea state. With h the envelope wave height normalized with the significant wave height, the envelope wave height p.d.f. reads

$$p(h) = 4he^{-2h^2}\left\{1 + C_4\left(2h^4 - 4h^2 + 1\right) + C_3^2\left(4h^6 - 18h^4 + 18h^2 - 3\right)\right\}. \tag{8.18}$$

where the parameters C_4 and C_3^2 are obtained from knowledge of the two-dimensional wave spectrum and are related to the kurtosis and skewness of the sea state. Here,

$$C_4 = \frac{\kappa_4}{8}, \tag{8.19}$$

and the envelope kurtosis κ_4 is given by

$$\kappa_4 = \kappa_{40} + 2\kappa_{22} + \kappa_{04} \tag{8.20}$$

while

$$C_3^2 = \frac{\kappa_3^2}{72},\ \kappa_3^2 = 5(k_{30}^2 + \kappa_{03}^2) + 9(\kappa_{21}^2 + \kappa_{12}^2) + 6(\kappa_{30}\kappa_{12} + \kappa_{03}\kappa_{21}) \tag{8.21}$$

The κ's refer to a number of cumulants of the joint distribution of the surface elevation $\eta = \rho\cos\theta$ and its Hilbert transform $\zeta = \rho\sin\theta$. In addition, it is noted that both free and bound waves may contribute to the cumulants.

8.3.4   Bound Waves.

The general expressions for skewness and kurtosis parameters are given in Janssen (2017). The parametrizations for C_3 and C_4 have been obtained in this reference as well, and are based on explicit expressions for the case of a narrow-band wave train. Here we use a slightly different version:

$$C_3^{bound} = 2.24m_0^{1/2}\left(\alpha + 0.9\Delta\right),$$

$$C_4^{bound} = 7.42m_0\left\{\gamma + \alpha^2 + (\alpha + \Delta)^2\right\}, \tag{8.22}$$

where m_0 is zeroth moment of the frequency spectrum. The wavenumber and depth dependent parameters α, γ and Δ are functions of the characteristic wave number, say $k_0 = \bar{k}$, and depth h. They read

$$\Delta = -\frac{k_0}{4}\frac{c_S^2}{c_S^2 - v_g^2}\left[\frac{2(1 - T_0^2)}{T_0} + \frac{1}{x}\right] + \frac{k_0^2\kappa_1}{2\omega_0\mu_1}\frac{\delta_\theta^2}{\delta_\theta^2 + \alpha_\omega\nu_\omega^2},$$

$$\alpha = \frac{k_0}{4T_0^3}\left(3 - T_0^2\right), \beta = \frac{3k_0^2}{64T_0^6}\left[8 + \left(1 - T_0^2\right)^3\right], \gamma = -\frac{1}{2}\alpha^2, \tag{8.23}$$

where $x = k_0 h$, $T_0 = \tanh x$, $c_S^2 = gh$, $v_g = \partial\omega/\partial k$, and $\omega_0 = (gk_0T_0)^{1/2}$. The second contribution to the mean sea level term Δ is new and is calculated in Appendix B of Janssen (2017). This additional contribution illustrates nicely that the narrow-band limit of the mean sea level is not unique as it depends on the order in which the limit of vanishing frequency width ν_ω and angular width δ_θ is taken.

8.3.5 Free Waves.

The parametrization of the dynamic part of the kurtosis has been guided by a result, which is strictly speaking only valid for Gaussian spectra in the narrow-band approximation and gives an estimate of the maximum of dynamic kurtosis. Rather then the maximum value to estimate the severity of the sea state, I will use its average value over a time span of about 300 wave periods. I have tried to stay as close as possible to the narrow-band result, and I paid particular attention to the replacement of the definitions of the Benjamin-Feir Index and the ratio of the square of directional width and frequency width to appropriate forms for broad-banded spectra.

After some extensive trial and error the following results are obtained: Introducing the Benjamin-Feir Index BFI and the parameter R which measures the importance of directional width over frequency width, the dynamic kurtosis factor is given by

$$C_4^{dyn} = J(R)BFI^2, \tag{8.24}$$

where the form of the the factor $J(R)$ is based on a mathematical analysis given in A.E.M. and Janssen (2019) regarding the behaviour of the exact narrow-band result around $R = 0$ and $R = 1$. It reads

$$J(R) \approx \frac{\pi\gamma}{3\sqrt{3}}\left(1 - \alpha\sqrt{R} + \beta R + +\delta R^2\right), \ 0 < R < 1, \tag{8.25}$$

where $\alpha = 4\sqrt{3}/\pi$ and $\beta = (1/3 + 2\sqrt{3}/\pi)$, and δ is chosen such that $J(R)$ at $R = 1$ satisfies the exact result that $J(R)$ vanishes. This gives the condition $1 - \alpha + \beta + \delta = 0$ from which $\delta = 2\sqrt{3}/\pi - 4/3 = -0.2307$. The parameter γ in (8.25) equals 1, but in the parametrization of the exact results of Janssen (2017) a better fit was found for $\gamma = 0.9$. The expression for $J(R)$ for $R > 1$ follows from the condition $J(R) = -J(1/R)/R$.

In the narrow-band approximation most of the wave energy is concentrated around the carrier wave number k_0, so that the wave spectrum has a small relative frequency width $\delta_\omega = \sigma_\omega/\omega_0$ and a small angular width δ_θ. For surface gravity waves on water of finite depth h the dispersion relation for the carrier reads

$$\omega_0 = \sqrt{gk_0T_0}, \ T_0 = \tanh x, \ x = k_0 h, \tag{8.26}$$

while the first and second derivative become

$$v_g = \omega_0' = \frac{1}{2}c_0\left\{1 + \frac{2x}{\sinh 2x}\right\}, \ c_0 = \frac{\omega_0}{k_0}, \tag{8.27}$$

and

$$\omega_0'' = -\frac{g}{4\omega_0 k_0 T_0} \times \Omega'', \tag{8.28}$$

with

$$\Omega'' = \left\{T_0 - x\left(1 - T_0^2\right)\right\}^2 + 4x^2 T_0^2\left(1 - T_0^2\right). \tag{8.29}$$

Note that for any value of the depth h the second derivative is always negative. Finally, the narrow-band limit of the nonlinear interaction coefficient is given by

$$X_{nl} = T_{0,0,0,0}/k_0^3 = \frac{9T_0^4 - 10T_0^2 + 9}{8T_0^3} - \frac{1}{x}\left\{\frac{(2v_g - c_0/2)^2}{c_S^2 - v_g^2} + 1\right\} + \frac{\kappa_1\nu_1}{\mu_1 k_0^3}\frac{\delta_\theta^2}{\delta_\theta^2 + \alpha_\omega\nu_\omega^2} \tag{8.30}$$

with κ_1, ν_1 and $\mu_1 = c_S^2$ wavenumber and depth dependent coefficients given in Appendix B of Janssen (2017), $c_S = \sqrt{gh}$ the shallow water wave velocity and

$$\alpha_\omega = \frac{c_0^2}{v_g^2}\left(1 - \frac{v_g^2}{c_S^2}\right).$$

The interaction coefficient consists of three terms. The first two terms are well-known (see e.g. Whitham, 1974) as the first term is connected with the nonlinear dispersion relation for surface gravity waves, while the second term is due to effects of wave-induced current caused by one-dimensional, longitudinal modulations. These two terms are of definite sign so they may cancel each other, which, in fact, happens for $x = k_0 h = 1.363$. The third term is new and is connected to the wave-induced current caused by two-dimensional modulations. It also has a definite sign and tends to reduce the dimensionless depth where the nonlinear interaction coefficient vanishes. A complete derivation of this new term and some discussion is presented in Janssen (2017). Hence, for intermediate water depth waves the nonlinear interactions are, because waves are two-dimensional, still expected to play a relatively important role.

In the narrow-band approximation, the evolution of the kurtosis is determined by two dimensionless parameters. The first one is the shallow water extension of the Benjamin-Feir Index. Introducing the wave steepness ϵ, while δ_ω is the relative frequency width, the Benjamin-Feir Index BFI is defined as

$$BFI^2 = \frac{8\epsilon^2}{\delta_\omega^2} \times \left(\frac{v_g}{c_0}\right)^2 \times \frac{T_0}{\Omega''} \times X_{nl} \tag{8.31}$$

Note that in the deep-water limit one recovers the usual expression for the Benjamin-Feir Index, as $\lim_{k_0 h \to \infty} BFI^2 = 2\epsilon^2/\delta_\omega^2$. The relative frequency width is obtained from Goda's peakedness factor Q_p defined as

$$Q_p = \frac{2}{m_0^2} \int_{\mathcal{D}} \mathrm{d}\omega\, \omega E^2(\omega), \tag{8.32}$$

with $E(\omega)$ the angular frequency spectrum and the integration domain $\mathcal{D}$ consists of all frequencies for which $E(\omega) > 0.4\, E(\omega_p)$ (Janssen and Bouws (1986)). The relative angular frequency width δ_ω then follows from

$$\delta_\omega = \frac{1}{Q_p \sqrt{\pi}}. \tag{8.33}$$

This definition of width emphasizes the peak region of the wave spectrum, which is thought to control the Benjamin-Feir instability.

The second dimensionless parameter measures the importance of directional width δ_θ with respect the frequency width ν_ω. In deep water it is defined as $R = \delta_\theta^2/2\nu_\omega^2$ while in general one has
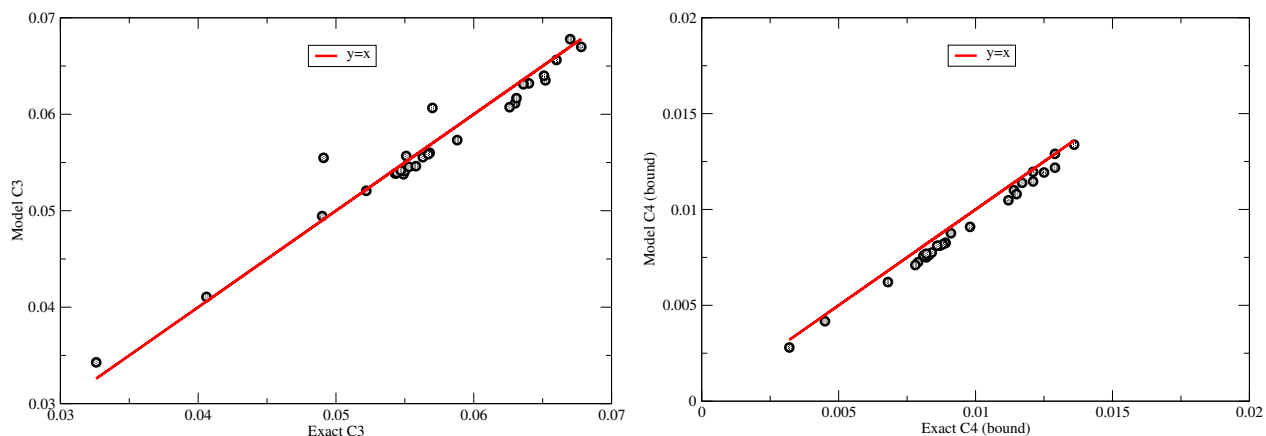
$$R = 4\frac{\delta_\theta^2}{\nu_\omega^2} \times \left(\frac{v_g}{c_0}\right)^3 \times \frac{T_0^2}{\Omega''} \tag{8.34}$$

It is important to note that the damping of the Benjamin-Feir instability is caused by the broad-band aspects of the wave spectrum, hence the relative frequency width is given by ν_ω, defined in Eq. (8.17).
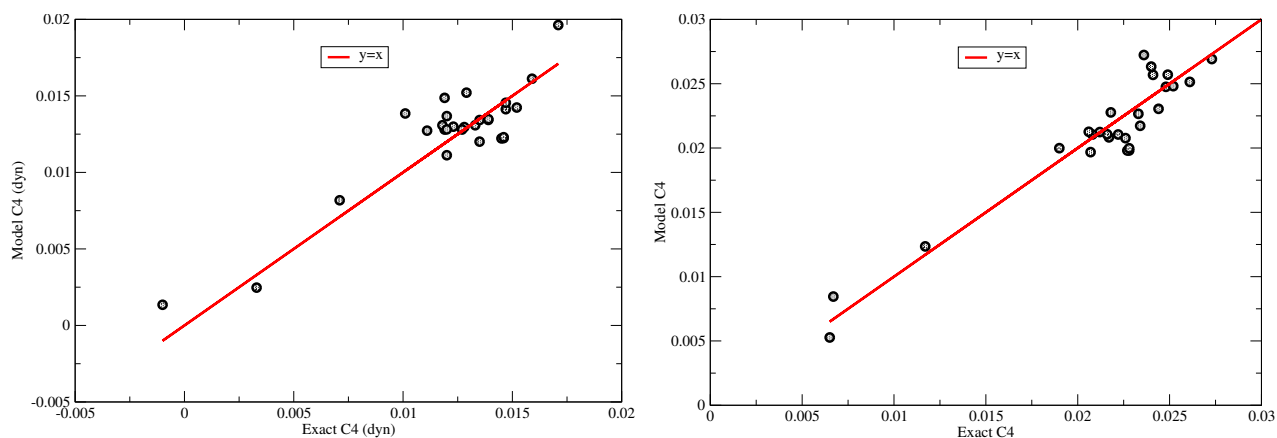
8.3.6 Verification against exact results.

Since, compared to Janssen (2017), I have slightly modified the parametrisations for skewness and bound and dynamic kurtosis I have repeated the comparison with exact computations from the Draupner and Andrea cases. These are shown in the Fig. 8.3 for skewness and bound kurtosis while results for dynamic kurtosis are shown in Fig. 8.4.

Quantitatively, the agreement, shown in Fig. 8.3, is impressive as follows from a linear fit of parametrized results against exact computations which gives correlations of more than 98%. Nevertheless, it is noted that the scatterplot of the skewness factor shows two modest outliers which correspond to the broad angular distribution cases of the Andrea storm.

Figure 8.3 *The left panel shows the comparison of parametrized skewness factor C_3^{bound} against exact computation from the Draupner and Andrea events, while the right panel shows the comparison for the kurtosis factor C_4^{bound}.*

Figure 8.4 *The left panel shows the comparison of parametrized dynamic kurtosis factor C_4^{dyn} against exact computations using spectra from the Draupner and Andrea events, while the right panel shows the comparison for the total kurtosis factor C_4.*

A comparison of the results obtained from the dynamic kurtosis parametrization and the exact computations using spectra from the Draupner and Andrea events is shown in the left panel of Fig. 8.4. There is a fair agreement but, clearly, compared to for example the bound-wave kurtosis, the agreement is not as good. Fortunately, the probability calculations only involve the total kurtosis, and as shown in the right panel of Fig. 8.4, this shows a better agreement with correlations of 96%. This is an improvement over the correlation found in Janssen (2017), which was 91%.

8.3.7 Maximum wave height distribution.

The probability distribution function $p(h)$ as given in Eq. (8.18) has a restricted validity in the sense that it underestimates the true p.d.f. for large envelope wave height in the range $h > 2.5$. In fact, nowadays there is ample evidence that the pdf of envelope wave height has an exponential tail. In Janssen (2017) it is suggested to remedy this problem by introducing an exponential tail. This is most conveniently done for the exceedance probability of wave energy $E = 2h^2$. This can immediately be obtained from the envelope wave height p.d.f. by integration from E to infinity. The result is

$$P(E) = e^{-E} \left[1 + C_4 A(E) + C_3^2 B(E) \right] , \qquad (8.35)$$

where

$$A(E) = \frac{1}{2}E(E - 2), \ B(E) = \frac{1}{2}E(E^2 - 6E + 6). \qquad (8.36)$$

It is suggested to replace $P(E)$ by an empirical formula found by A. *et al.* (2009) for nonlinear optical cavities, which also applies equally well in other nonlinear optics applications. The simple empirical form reads

$$P(E) = \int_E^\infty \mathrm{d}x\, p(x) = e^{-z}, \; z = -\alpha + \sqrt{\alpha^2 + \beta E}, \tag{8.37}$$

where (see Janssen (2017)) $\beta = 2(\alpha + 1)$ as for zero energy the c.d.f. should equal 1, so that for matching purposes one only needs to determine the parameter α.

This simple form has some interesting properties. First of all, the condition $P(E = 0) = 1$ is automatically satisfied so that the underlying pdf $p(E)$ is normalized to 1. Second, for small E Taylor expansion of z gives $z = \beta E/(2\alpha)$ hence

$$\lim_{E \to 0} P(E) = e^{-\frac{\beta}{2\alpha} E}, \tag{8.38}$$

while for large E one finds

$$\lim_{E \to \infty} P(E) = e^{-\sqrt{\beta E}}. \tag{8.39}$$

Realizing that $E = 2h^2$ this means that in terms of envelope wave height we have for small E a Gaussian distribution while for large E the distribution is exponential.

A relation for α is now obtained by matching the empirical c.d.f. (8.37) with the theoretical one, given in Eq. (8.18), which is denoted by P_{th}. The fitting constant α then follows from the condition that at the edge of the range of validity, taken as $E_b = 10$ (corresponding to $h = 2.2$), the empirical CDF equals the theoretical one, i.e. $P(E_b) = P_{th}(E_b)$. This gives for α,

$$\alpha = \frac{f_b^2 - 2E_b}{2(E_b + f_b)}, \; f_b = \log P_{th}(E_b). \tag{8.40}$$

where f_b is the logarithm of the theoretical c.d.f. at the boundary given by $E = E_b$. In this manner a connection between skewness and kurtosis of the sea state, via f_b, and the fitting parameters of the empirical CDF has been established. For relatively small values of C_4 and C_3 this matching procedure works well, as reported in Janssen (2015a).

The c.d.f. (8.37) is therefore found to be quite accurate in estimating probabilities of extreme sea states and in providing an estimate of the expected maximum wave height. Defining the expectation value of maximum emvelope wave height as

$$\langle H_{max} \rangle = \sqrt{\frac{1}{2} \langle E_{max} \rangle}, \tag{8.41}$$

then, according to Janssen (2017), the expectation value of wave energy follows from iterating the relation

$$\langle E_{max} \rangle = \frac{1}{\beta} \left[G_2 - 2G_1 \left(\alpha + \log N \right) + \log N \left(2\alpha + \log N \right) \right], \tag{8.42}$$

where $N = N_{slc} \sqrt{\langle E_{max} \rangle / 2}$, as the number of events N depends on the expectation value of E_{max}. Note that N_{slc} is a measure of the number of wave groups in a timeseries of length T_L. It is defined as

$$N_{slc} = 2\nu\bar{\omega}T_L / \sqrt{2\pi} \tag{8.43}$$

where $\bar{\omega} = m_1/m_0$ is a mean angular frequency while $\nu = (m_0 m_2/m_1^2 - 1)^{1/2}$ is a measure of the width of the frequency spectrum as introduced by Longuet-Higgins (1983) .

The symbols G_n, $n = 1, 2$ in (8.42) denote integrals involving exponentials and logarithms. These are related to the Gamma function $\Gamma(1 + z)$ and its derivatives,

$$\Gamma(1 + z) = \int_0^\infty t^z e^{-t} \mathrm{d}t = \int_0^\infty e^{z \log t} e^{-t} \mathrm{d}t,$$

and therefore

$$G_n = \left. \frac{\mathrm{d}^n}{\mathrm{d}z^n} \Gamma \right|_{z=0} = \int_0^{\infty} \log^n t \, e^{-t} \mathrm{d}t, n = 1, 2, 3, ...$$

It may be shown that $G_1 = \Gamma'(1) = -\gamma$, while $G_2 = \Gamma''(1) = \gamma^2 + \pi^2/6$, where $\gamma = 0.5772$ is Euler's constant.

Although (8.42) is an implicit equation for the expectation value of maximum wave energy, it is straightforward to solve it by iteration. In practice, this iteration scheme converges very quickly, only 5 iteration are needed at the most.

Finally, it should be emphasized that the expression (8.42) is very elegant, and, compared to previous work (Janssen (2015b)), it is much simpler. This is, of course, because of the use of the stretched exponential for the 'parent' distribution for envelope wave height. In addition, it should be noted that for a Gaussian sea state, which is achieved by taking the limit of $\alpha \to \infty$ (while realizing that $\beta = 2(\alpha + 1)$) the expression for maximum wave energy simply becomes

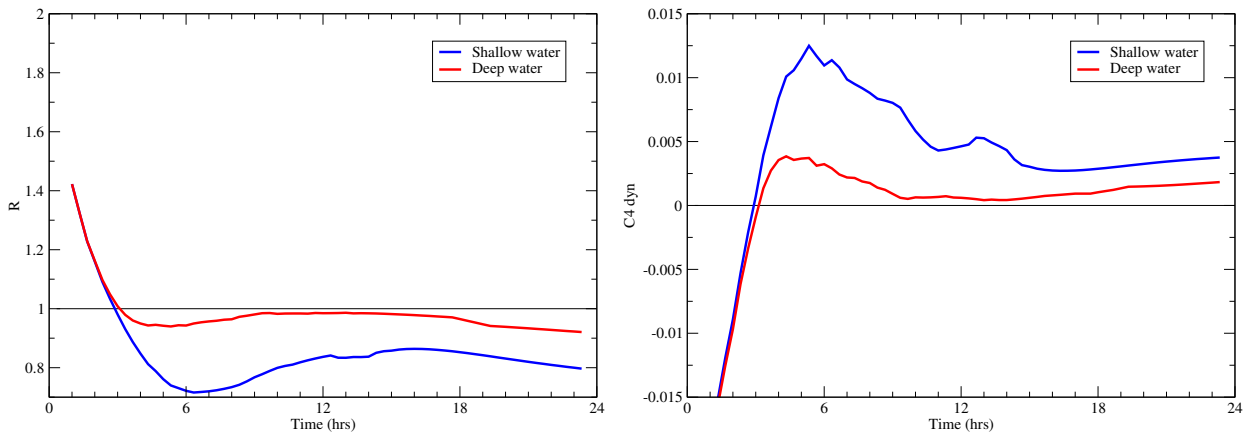$$\langle E_{max} \rangle = \gamma + \log N.$$

8.3.8 Pre-operational results.

The final step I have taken is to check results of the here obtained parametrizations for skewness and kurtosis in the context of the ECWAM wave prediction system. Firstly, I have studied results from a single grid-point wave model in deep and shallow water which illustrates the sensitive dependence of the dynamic kurtosis on the normalized directional width R. Secondly, I have obtained statistical results using forecast ECWAM spectra from one synoptic time and I have studied relations such as the dependence of skewness and kurtosis on the wave age parameter c_p/U_{10} and the dependence of the normalized maximum envelope wave height on the Benjamin-Feir Index and the dimensionless directional width R.
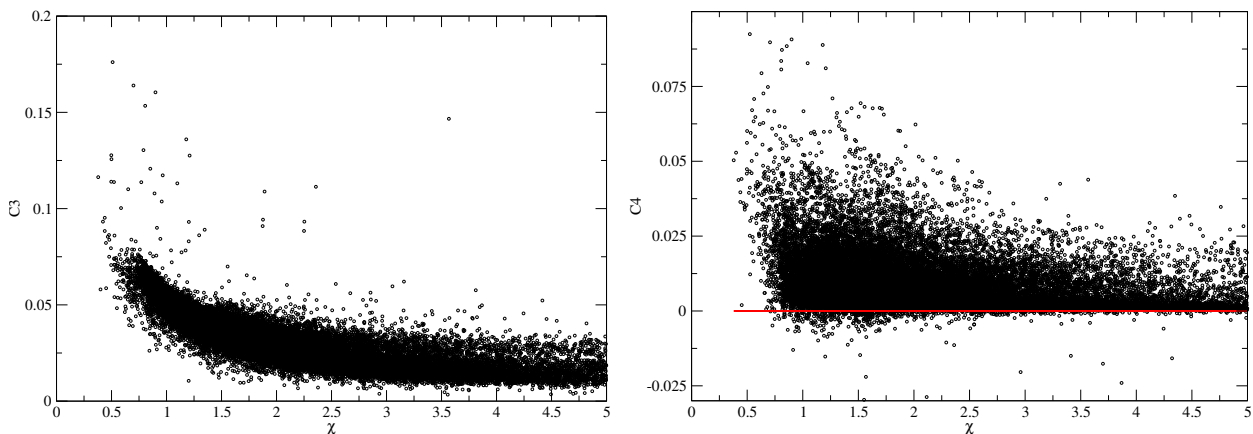
8.3.9 Single gridpoint Results.

The parametrization of the dynamic kurtosis is given in Eqns. (8.22) and (8.24). It shows that dynamic kurtosis depends on the square of the Benjamin-Feir Index BFI appropriately defined by including shallow water effects. In addition, it shows that dynamic kurtosis reduces when, compared to the frequency width, the directional width of the 2D wave spectrum increases, where the effect of directional width is measured by the dimensionless directional width R. Suppose that initially the wave spectrum has a narrow directional distribution such that $R < \alpha = 1$. Then, the nonlinear interactions will broaden the directional spectrum in such a way that R increases and hence the dynamic kurtosis decreases until for large time an 'equilibrium' condition is obtained for which the dynamic kurtosis vanishes. Therefore, large deviations from the Gaussian equilibrium, and hence large values of kurtosis, are only expected for relatively short times.

In order to illustrate the sensitive dependence of results from dynamic kurtosis on the dimensionless width R, I have run the one-gridpoint version of the WAM model for deep-water and shallow water (with depth of 40 m). The windspeed was constant and had the value of 18.45 m/s. The wave spectrum was discretized in the same manner as the operational ECWAM model and therefore consisted of 36 frequencies and 36 directions. As initial condition a JONSWAP spectrum was chosen with a cos-square directional distribution. The directional distribution is so broad that dimensionless directional width is larger than the threshold value $\alpha = 1$, hence dynamic kurtosis is initially negative. In Fig. 8.5, two results are shown from this experiment, namely a comparison of the evolution in time of the dimensionless angular width of the spectrum for the deep and the shallow water case and the consequent evolution of the dynamic kurtosis. It is noted that shallow water effects may play an important role in the formation of freak waves as in deep-water the dynamic kurtosis is negative, or almost vanishes resulting in a small focussing of the weakly nonlinear wave train, while in shallow water the wave train experiences significant focussing because the dynamic kurtosis is positive after time equals 3 hours. Inspecting the time evolution of the normalized width R it should be clear that this different behaviour in deep and shallow water is connected to the findings in Section 3 of Janssen (2017) that shallow water spectra are, compared to deep water, more narrow. This has, according to the left panel of Fig. 8.5 important consequences because for deep water R is always larger than or close to the threshold value of R, while in shallow water R gets really below the threshold value, giving significant focussing.

Figure 8.5 *Left Panel: Comparison of time-evolution of normalized width parameter R for deep and shallow water. The threshold value of $\alpha = 1$ is indicated as well. Right panel: Comparison of time-evolution of dynamic kurtosis for deep and shallow water.*
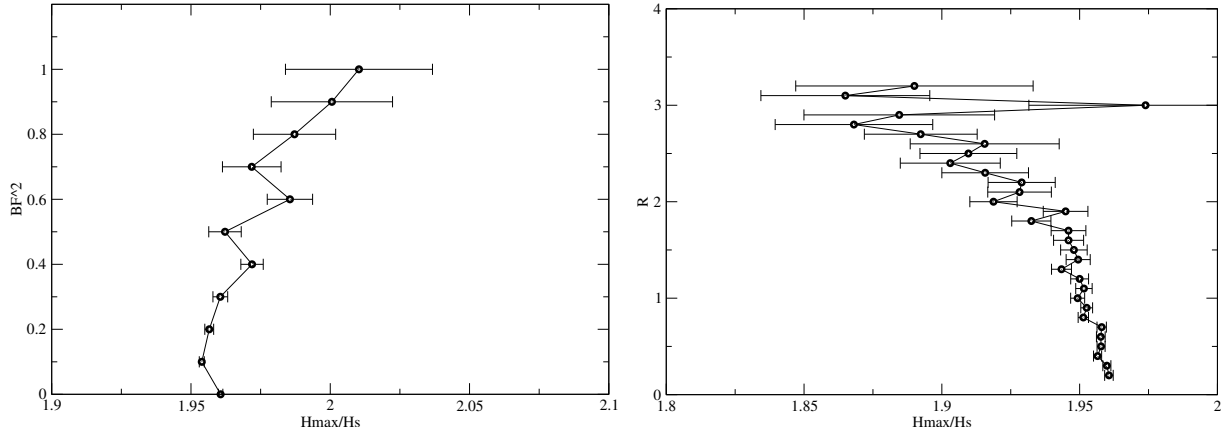
8.3.10 A Synoptic Example.

Figure 8.6 *Skewness factor C_3 (left panel) and kurtosis factor C_4 (right panel) versus wave age parameter $\chi = c_p/U_{10}$. Note that there are many occasions where the directional wave spectrum is so broad that kurtosis is slightly negative.*

As a final illustration of the properties of the new version of the freak wave warning system results of a single forecast, namely the analysis of the 15th of January 2018 at 12 hrs, will be briefly discussed.

A number of integral parameters such as significant wave height and several versions of mean period were retrieved which allowed the determination of the moments m_{-1}, m_0, m_1, m_2 needed for the specification of the spectral frequency width parameters. In addition, parameters such as the Benjamin-Feir Index and the angular width were retrieved, enabling the determination of the skewness and kurtosis at every gridpoint and also the determination of the expectation value of maximum envelope wave height.

In Fig. 8.6, results for skewness and kurtosis from a one-degree retrieval are plotted as function of a parameter measuring the stage of development of the sea state, namely the wave age $\chi = c_p/U_{10}$. For young waves, with $\chi < 1$ the envelope skewness C_3 reaches values of 0.1 which corresponds to a surface elevation skewness which is three times larger. The behaviour of the kurtosis parameter C_4 which is the sum of bound-wave kurtosis and dynamic kurtosis is somewhat more complex. Although the bound-wave part of kurtosis is always positive, dynamic kurtosis may become negative, which occurs for spectra with a broad directional distribution. As a consequence, in number of cases (2% or more) kurtosis turns out to be negative, giving compared to the Gaussian sea state a reduced risk of the occurence of freak waves. On the other hand, for narrow directional spectra, kurtosis is positive, reaching values of up to 0.1, resulting in an enhanced risk for freak waves. Note

Figure 8.7 *Left Panel: Dependence of expectation value of normalized maximum wave height on the square of the Benjamin-Feir Index (left panel) and on normalized directional width R (right panel). The error bars give the width of the maximum wave height distribution at the BFI^2 or R value of interest*

that these large values of kurtosis are caused by the dynamic part of kurtosis. If one would disregard the dynamic part in the kurtosis calculation than kurtosis would always be positive but would reach at most values of 0.02.

In the next plot, Fig. 8.7, I concentrate on the expectation value of maximum envelope wave height for a 20 min. time series and I study its dependence on parameters such as the square of the Benjamin-Feir Index, BFI^2, and the dimensionless directional width R. These relations are obtained by collecting maximum envelope wave height data as function of a discretized version of the independent parameter and by plotting the bin-average. In agreement with expectations and with results of Burgers *et al.* (2008), based on observations of normalized maximum wave height obtained from AUK platform in the central North Sea, the expectation value of maximum envelope wave height is seen to increase with increasing Benjamin-Feir Index. On the other hand, maximum wave height is seen to decrease, as expected, with increasing dimensionless directional width.

Furthermore, in Janssen and Bidlot (2009) a detailed comparison between observed and modelled distribution of maximum envelope wave height has been made. As argued by these authors, a way to simulate the observed maximum wave height distribution is to start from the theoretical pdf of maximum wave height, the explicit form of which is given in Janssen (2017), i.e.

$$p_{max}(h) = \frac{\mathrm{d}\mathcal{G}}{\mathrm{d}h} \exp(\mathcal{G}), \tag{8.44}$$
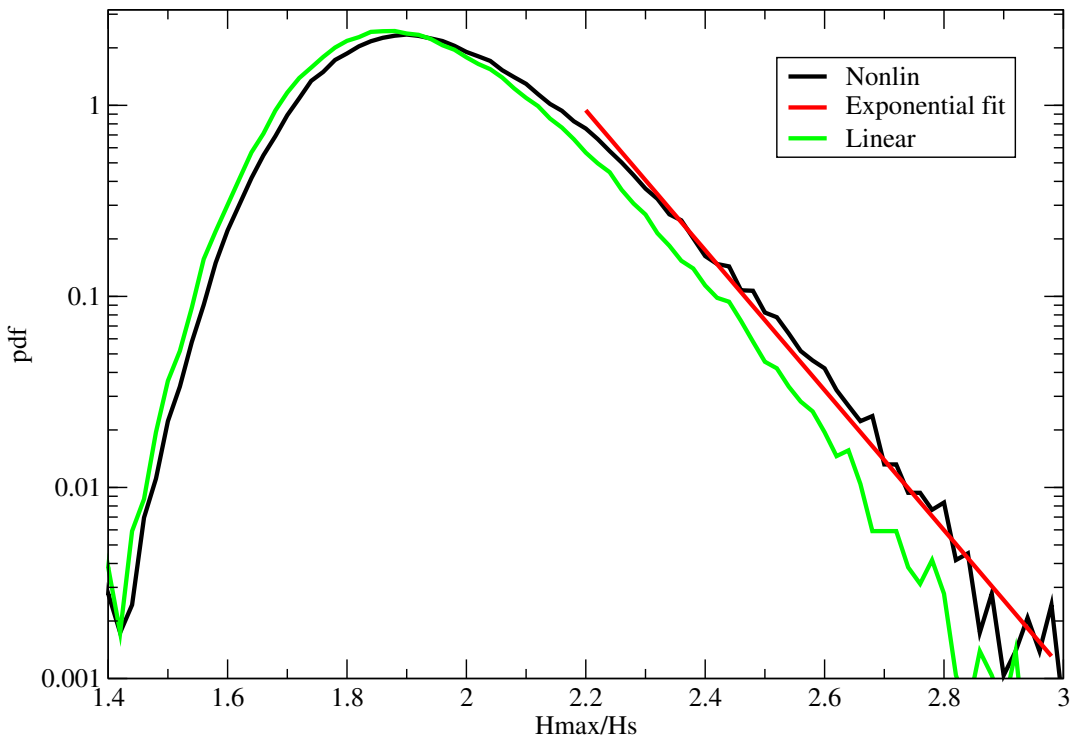
where $\mathcal{G}$ involves the stretched exponential

$$\mathcal{G} = -N \exp(-z), \ z = -\alpha + \sqrt{\alpha^2 + \beta E}. \tag{8.45}$$

and, in keeping with Naess' approach, the number of degrees of freedom depends on the reference level, i.e.

$$N = N_{slc} \left(\frac{E}{2}\right)^{1/2} \tag{8.46}$$

where N_{slc} is given by (8.43). Finally, the parameters α and β follow from matching the stretched exponential distribution with the weakly nonlinear c.d.f. of (8.18) so that the fitting parameters depend on skewness and kurtosis of the envelope time series.

One then generates from this pdf for given number of waves N_{slc} and given skewness C_3 and kurtosis C_4 a random draw of maximum wave height. The usual procedure for this is that one obtains a random draw of maximum envelope wave height from the condition that the cumulative distribution is a random number between 0 and 1. The resulting modelled distribution function is plotted in Fig. 8.8. It is remarked that the tail of the maximum wave height distribution is basically the number of degrees of freedom N (see (8.46)) times the envelope wave height pdf (8.37). Therefore, for large values of maximum envelope wave height the

Figure 8.8 *Global maximum wave height distribution obtained by a random draw of H_{max} for given number of waves and given skewness and kurtosis. Including skewness and kurtosis shows that the tail of the distribution is exponential. The distribution according linear theory is shown as well.*

distribution function is an exponential. As can been seen from the present fit, the simulated maximum wave height distribution closely follows the exponential fit, which on a logarithmic plot is a straight line. In order to illustrate effects of nonlinearity, also simulated maximum wave height distribution without nonlinear effects is shown, and clearly, nonlinear effects are seen to play an important role for the extreme events.

Finally, the present approach has been based on an analysis of time series using the envelope. This differs from the usual method whereby one considers wave height or crest height. In these latter approaches an extreme event is called a freak if wave height is larger than 2.2 times the significant wave height or, alternatively, if the crest height is larger than 1.25 times the significant wave height. In my opinion, the envelope waveheight follows closely the crest of the waves and therefore, in the context of the envelope approach, I would call an extreme event a 'freak' if the maximum envelope wave height is 2.5 times the significant wave height $H_S = 4\sqrt{m_0}$ with m_0 the zeroth moment of the wave spectrum. Adopting this definition of a freak wave it is therefore of interest to determine the probability that maximum normalized envelope wave height is larger than 2.5. Based on the Global distribution shown in Fig. 8.8, this probability is according to linear theory about 4.6×10^{-3} while according to nonlinear theory, this probability is a factor of 2. larger, namely 9.5×10^{-3}.

8.3.11 Conclusions.

A brief overview has been given of a shallow water version of ECMWF's freak wave warning system, which hopefully will be introduced in the near future.

Although 10 years ago I thought that in shallow water nonlinear focussing would play a relatively small role (Janssen and Onorato (2007)), a more detailed analysis, given by Janssen (2017), has shown that indeed for one-dimensional propagation the Benjamin-Feir Instability disappears for $k_0 h < 1.363$. However, ocean waves are two-dimensional, and in two dimensions the Benjamin Feir Instability and the resulting nonlinear focussing do exist. In addition, a number of numerical simulations with e.g. the ECWAM model, suggest that wave spectra are more narrow-banded in shallow water, giving an additional scope for nonlinear focusing.

Finally, in the context of coupled modelling it would now be of interest to introduce ocean currents in the wave forecasting system, which might lead to additional freak wave events.

Chapter 9

Second-order spectrum

Table of contents

**** Note that it was discovered too late that the second order correction was switched off in cycle CY45R1 (June 2018). It is anticipated that it will be switched back on with CY46R1 for all parameters that are determined from spectral moments (see Chapter 10).

Although ocean wave forecasting is mainly about the evolution of the free surface gravity waves, higher order effects such as the generation of second-harmonics and the generation of infra-gravity waves, may be important as well. This is, in particular, the case when waves propagate towards the beach where they shoal, hence their amplitude increases and wavelength decreases resulting in steeper waves. The pronounced nonlinearity gives rise to significant nonlinear triad interactions which result in a dramatic change of the shape of the waves from symmetric to asymmetric and also cause significant deviations from Gaussian statistics. As will be discussed here even for deep water waves second-order corrections affect the higher order moments and therefore it make sense to introduce these corrections in the operational version of the ECMWF wave model ECWAM.

9.1   THEORETICAL BACKGROUND

Surface gravity waves are usually described in the context of the potential flow of an ideal fluid. It was Zakharov (1968), who discovered that the resulting nonlinear evolution equations can be obtained from a Hamiltonian, which is the total energy E of the fluid, while the appropriate canonical variables are the surface elevation $\eta(\mathbf{x}, t)$ and the value ψ of the potential ϕ at the surface, $\psi(\mathbf{x}, t) = \phi(\mathbf{x}, z = \eta, t))$.

For small wave steepness the potential inside the fluid may be expressed in an approximate manner in terms of the canonical variables and as a result the Hamiltonian can be expressed as a series expansion in terms of the action variable $A(\mathbf{k}, t)$ (which is related to the Fourier transform of the canonical variables). The second order term corresponds then to linear theory, while the third and fourth order terms represent effects of three and four wave interactions. Excluding effects of capillarity, it is well-known that the dispersion relation for surface gravity waves does not allow resonant three wave interactions, while it only allows one particular kind of resonant four-wave interaction, namely there is only four-wave resonance for waves that satisfy the condition

$$\mathbf{k}_1 + \mathbf{k}_2 = \mathbf{k}_3 + \mathbf{k}_4, \ \omega_1 + \omega_2 = \omega_3 + \omega_4. \tag{9.1}$$

Note that in principle other types of four-wave interactions may exist such as $\mathbf{k}_1 - \mathbf{k}_2 = \mathbf{k}_3 + \mathbf{k}_4$ and , $\mathbf{k}_1 + \mathbf{k}_2 = -\mathbf{k}_3 - \mathbf{k}_4$ (with corresponding conditions for the frequencies), but surface gravity waves cannot satisfy these alternative resonance conditions. As a consequence there exists a non-singular canonical transformation of the type

$$A = A(a, a^*) \tag{9.2}$$

that allows to eliminate the third-order terms and the non-resonant fourth-order terms from the Hamiltonian. In terms of the new action variable $a(\mathbf{k}, t)$ the Hamiltonian now only has quadratic and quartic terms and the Hamilton equation attains a relatively simple form and is known as the Zakharov equation. It reads

$$\frac{\partial a_1}{\partial t} + i\omega_1 a_1 = -i \int d\mathbf{k}_{2,3,4} T_{1,2,3,4} a_2^* a_3 a_4 \delta_{1+2-3-4}, \tag{9.3}$$

where $\omega(\mathbf{k})$ is given by the dispersion relation for surface gravity waves

$$\omega^2 = gk \tanh kD, \tag{9.4}$$

and the interaction coefficient $T_{1,2,3,4}$ which, in order to preserve the Hamiltonian property, enjoys the symmetry condition $T_{1,2,3,4} = T_{3,4,1,2}$, may be found in Janssen (2004).

In the Hamiltonian theory of surface gravity waves there is therefore a natural distinction between free waves, which obey the dispersion relation, and forced waves such as second harmonics, which do not satisfy the dispersion relation and which follow from the canonical transformation (9.2). The evolution of the free waves is determined by the Zakharov equation which describes how the free waves are affected by four-wave interactions. Now it turns out that there are two kinds of four-wave interactions. The first one is called a 'direct' interaction as it involves interaction between free waves, while the second type is called the 'virtual-state' interaction as a virtual state of bound waves is generated by two waves and this virtual state then decays into, in general, a different set of free waves. Hence, the interaction coefficient for four-wave interactions $T_{1,2,3,4}$ is determined by both bound waves and free waves. For narrow-band deep-water waves the direct interaction and the virtual state interaction have equal weight.

Once the solution to the Zakharov equation is known for a, one still needs to apply the canonical transformation to recover the actual action variable A, and hence the surface elevation. Although the difference between the two action variables is only of the order of the wave steepness, there are a number of applications where one is interested in the higher order effects. Examples are the high frequency (HF) radar (e.g. Wyatt, 2000) which basically measures aspects of the second-order spectrum, and the estimation of the sea state bias as seen by an Altimeter (Elfouhaily *et al.* (1999)).

For this reason Janssen (2009) studied some properties and consequences of the canonical transformation in the context of the statistical theory of weakly nonlinear ocean waves. In particular, the second moment $\langle \eta^2 \rangle$ and the associated wavenumber variance spectrum $F(\mathbf{k})$ and directional frequency spectrum $F(\Omega, \theta)$ was considered. The second-order corrections to the wave spectrum (called the second-order spectrum for short) were obtained by deriving a general expression for the wavenumber-frequency spectrum. The wave number spectrum and the frequency spectrum then follow from the marginal distribution laws. Some properties of these second-order spectra were discussed in detail, both for deep-water and for shallow water, but numerical results were only presented for the case of one-dimensional propagation.

It was found that the second-order wavenumber spectrum contains two groups of terms, namely terms which are fully nonlinear and they describe the generation of second harmonics and infra-gravity waves, and terms which are termed quasi-linear because they are proportional to the first-order spectrum. The quasi-linear terms are an example of a self-interaction and give a nonlinear correction to the energy of the free waves, whereas the fully nonlinear terms describes the amount of energy of the bound waves which do not satisfy the linear dispersion relation.

While the second-order wavenumber spectrum consists of two contributions, namely one contribution giving the effects of bound waves and one quasi-linear term, the second-order frequency spectrum has an additional term which, not surprisingly, is related to the Stokes frequency correction. In deep water the Stokes frequency correction has only a small impact on the spectral shape near the peak. However, second-order corrections do have an impact on the high-frequency tail of the spectrum. Taking as first-order spectrum a Phillips' spectrum which has an Ω^{-5} tail, it is found that from twice the peak frequency and onwards the sum of the first and second-order spectrum (called the total spectrum from now on) has approximately an Ω^{-4} shape. Hence, second-order corrections to the frequency spectrum are important and they mainly stem from the combined effects of the generation of bound waves and the quasi-linear self-interaction.

In shallow water, gravity waves are typically more nonlinear as the ratio of the amplitude of the second harmonic to the first harmonic rapidly increases with decreasing dimensionless depth. Therefore, compared to the first-order spectrum the second-order spectrum may give rise to considerable contributions, in particular in the frequency domain around twice the peak frequency and in the low-frequency range where forced infra-gravity waves are generated. In addition, for a dimensionless depth of $\mathcal{O}(1)$, the Stokes frequency correction is found to give a considerable down-shift of the peak of the frequency spectrum.

In ocean wave forecasting the main interest is in the evolution of the wave spectrum and the rate of change of the free wave spectrum is obtained from the Zakharov equation. For a Gaussian homogeneous sea state one

then finds that the free wave spectrum will evolve in time due to resonant four-wave interactions (Hasselmann (1962);Janssen (2004)). Apart from the free wave contributions there are also contributions by forced waves to the spectrum. With Ω the angular frequency and θ the wave propagation direction, the angular frequency-direction spectrum $F(\Omega, \theta)$ becomes

$$
\begin{aligned}
F(\Omega_1, \theta_1) \;=\; & E(\Omega_1, \theta_1) - \frac{\partial}{\partial \Omega_1} \left\{ E(\Omega_1, \theta_1) \int \mathrm{d}\Omega_2 \mathrm{d}\theta_2 \, \hat{T}_{1,2,2,1} E(\Omega_2, \theta_2) \right\} \\
& + \int_0^{\Omega_1} \mathrm{d}\Omega_2 \mathrm{d}\theta_2 \, E(\Omega_1 - \Omega_2, \theta_1) E(\Omega_2, \theta_2) \mathcal{A}^2_{1-2,2} \\
& + 2 \int_0^\infty \mathrm{d}\Omega_2 \mathrm{d}\theta_2 \, E(\Omega_1 + \Omega_2, \theta_1) E(\Omega_2, \theta_2) \mathcal{B}^2_{1+2,2} \\
& + 2 E(\Omega_1, \theta_1) \int \mathrm{d}\Omega_2 \mathrm{d}\theta_2 \, E(\Omega_2, \theta_2) \mathcal{C}_{1,1,2,2},
\end{aligned}
\tag{9.5}
$$

where $E(\Omega, \theta)$ is the free wave spectrum and $\hat{T}_{1,2,2,1} = T_{1,2,2,1}/f_1^2$. The term involving $\hat{T}$ gives the effect of the Stokes frequency correction on spectral shape. The interaction coefficients $\mathcal{A}$, $\mathcal{B}$ and $\mathcal{C}$ are connected to the coefficients of the canonical transformation. Details of the derivation are given in Janssen (2009).

The transfer coefficients $\mathcal{A}$ and $\mathcal{B}$ have a fairly straightforward physical interpretation, as $\mathcal{A}$ measures the strength of the generation of the sum of two waves, hence measures the strength of the generation of second harmonics, while $\mathcal{B}$ measures the generation of low-frequencies, and hence also the generation of the mean sea level induced by the presence of wave groups. The coefficient $\mathcal{C}$ measures the correction of the first order amplitude of the free waves by third-order nonlinearity.

A number of properties of the second-order spectrum have been studied in some detail by Janssen (2009). This reference also showed some numerical and analytical examples of the second order effects but these mainly concerned the case of one-dimensional propagation. Here, only some integral properties are mentioned. Integration of Eq. (9.5) over all frequencies and directions gives

$$
\langle \eta^2 \rangle = \int \mathrm{d}\Omega_1 \mathrm{d}\theta_1 F(\Omega_1, \theta_1) = \int \mathrm{d}\Omega_1 \mathrm{d}\theta_1 E_1 + \int \mathrm{d}\Omega_1 \mathrm{d}\theta_1 \mathrm{d}\Omega_2 \mathrm{d}\theta_2 \mathcal{T}_{1,2} E_1 E_2
\tag{9.6}
$$

where

$$
\mathcal{T}_{1,2} = \mathcal{A}^2_{1,2} + \mathcal{B}^2_{1,2} + 2\mathcal{C}_{1,1,2,2},
$$

while it is noted that the Stokes frequency correction does not contribute to the integral because it is a perfect derivative. Now $\mathcal{T}$ has the remarkable property that it is anti-symmetric: $\mathcal{T}_{1,2} = -\mathcal{T}_{2,1}$ and therefore the vanishing of the second integral in (9.6) follows at once. In other words, according to Janssen (2009) the second-order effects do not contribute to the wave variance. In contrast, other studies on second-order effects, such as performed by Tick (1959), Longuet-Higgins (1963) and Barrick and Weber (1977) show that second-order effects give a large, in fact diverging, contribution to the wave variance. The reason for this large discrepancy is that these earlier studies, as pointed out by Creamer et al. (1989), overlooked an important contribution to the second-order spectrum corresponding to the quasi-linear term of Eq. (9.5). Inclusion of the quasi-linear term exactly compensates for the contribution to the wave variance by the bound waves. However, it is emphasized that all other moments of the spectrum are affected by the presence of the bound waves.

9.2 NUMERICAL IMPLEMENTATION OF SECOND-ORDER CORRECTIONS.

In this § the numerical implementation of Eqn. (9.5) is described and results are shown for some simple free wave spectra in shallow water. The numerical implementation consists of two parts. First the numerical treatment of the interaction coefficients is given and second the numerical integration procedure is presented.

The detailed expressions for the interaction coefficients are given in Janssen (2009) and they are valid for arbitrary depth D. It should be clear that these interaction coefficients are very complicated and contain numerous apparent singularities. For example, a discussion on how to treat the singularities in $T_{1,2,3,4}$ is given
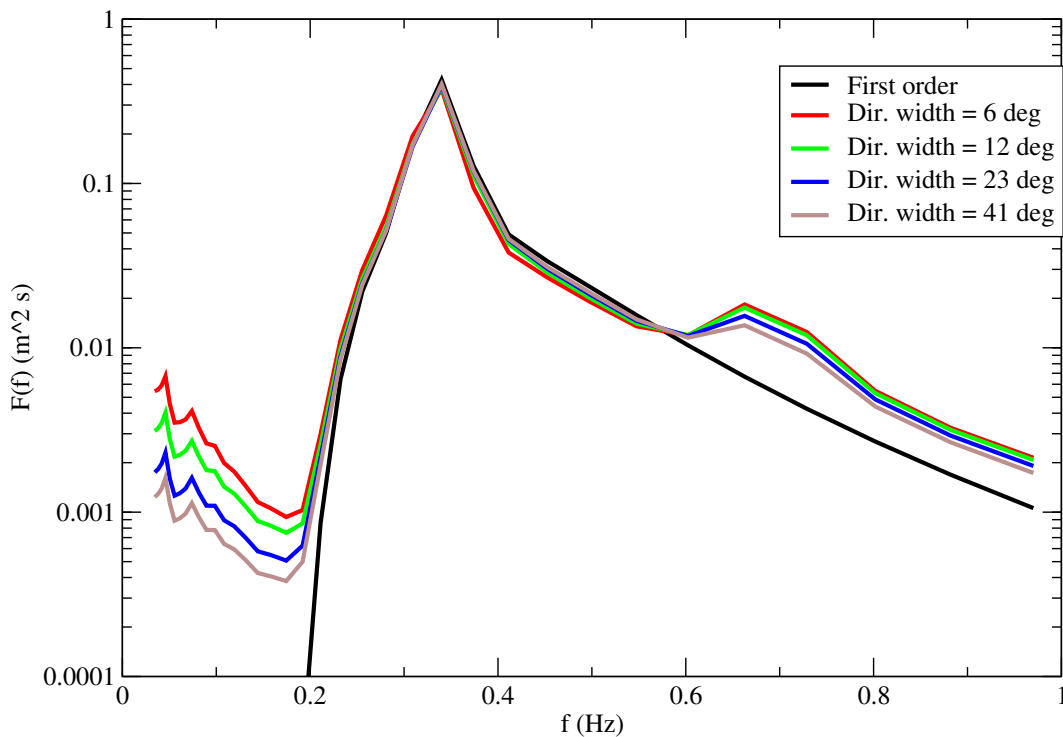
in Janssen and Onorato (2007). In all the other interaction coefficients the singularities have been removed as well and numerical results have been found to be in good agreement with analytical expressions for a number of special cases. Because these interaction coefficients are so involved it make sense to pre-calculate them for efficiency reasons. However, this could result in very big demands on memory requirements unless certain measures are being taken.

First, in present wave forecasting systems the depth variable D is discretized using a logarithmic scaling relation with gives high accuracy for shallow water. In the ECWAM model we use $D(N) = D_A D_D^{N-1}$, where for a global application typically $D_A = 5$, $D_D = 1.1$ and the maximum value of N, denoted by N_{depth}, is 74.

Second, although in general the interaction coefficients are, apart from depth D, a function of four variables k_1, k_2, θ_1 and θ_2, it should be mentioned that, without giving an explicit proof, the interaction coefficients are independent of the orientation of the grid in wavenumber space. This implies that apart from the dependence on the magnitude of the wave vectors (i.e. k_1 and k_2) they only depend on the difference angle $\theta_2 - \theta_1$. In order to estimate the size of the look-up tables for the interaction coefficients let us suppose that the spectrum has N_{ang} directions and N_{fre} frequencies, where wave numbers are connected with the frequencies through the dispersion relation (9.4). Therefore, the size of each look-up table becomes $N_{depth} N_{ang} N_{fre}^2$. As the present operational wave forecasting system has $N_{ang} = 36$ and $N_{fre} = 36$ this amounts to a size of 3.5 million numbers, a memory requirement which is feasible on present-day HPC systems. Thus the inter

N_{de}

Figure 9.1 *Variance spectra as function of frequency (Hz) for different values of the directional width, showing that the infra-gravity part of the spectrum is sensitive to the width of the spectrum. The depth is 1.7 m.*

The next step is to evaluate the integrals in (9.5). The integrals are replaced by summations using the Trapezoid rule with variable resolution in the frequency direction. Each spectral component then requires $N_{ang} N_{fre}$ operations, hence the calculation of each spectrum requires the square of this which is $N_{ang}^2 N_{fre}^2$

operations. In order to minimize a number of calculations in spectral space it is advantageous, at least for the ECMWF HPC system, to have the loop over the grid points as inner do-loop.

The software was validated extensively against the one-dimensional cases discussed by Janssen (2009). Here a number of two-dimensional cases in shallow water are presented using the operational configuration. In the angular direction a regular grid is used while the frequencies are on a logarithmic grid with a relative increment $\Delta f/f = 0.10$. The number of frequencies N_{fre} and directions N_{ang} is equal to 36, while the starting frequency f_0 equals $0.01 \times (1.1)^{13} \approx 0.034523$. Therefore, the two-dimensional spectrum is only known at discrete frequencies and directions given by

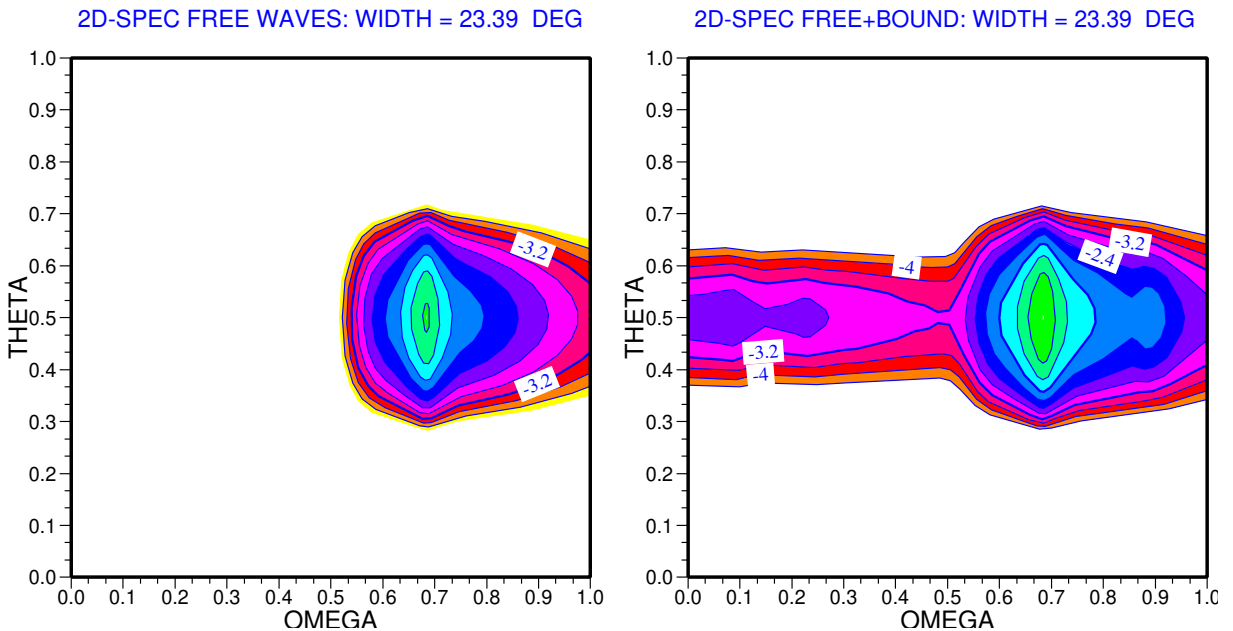$$f_m = f_0(1 + \Delta f/f)^{(m-1)}, \ 1 \le m \le N_{fre}$$
$$\theta_k = k\Delta\theta, \ \Delta\theta = 1/N_{ang}, \ 1 \le k \le N_{ang}$$

As first-order spectrum the product of a JONSWAP frequency spectrum $F(f)$ and a cosine angular distribution $D(\theta)$ is taken where θ is the wave propagation direction. The JONSWAP spectrum has peak angular frequency $\Omega_0 = 2.1$, Phillips parameter $\alpha_p = 0.015$ and overshoot parameter $\gamma = 7$, with frequency width $\sigma = 0.07$. The directional distribution was chosen to depend on $\cos\theta$ (with θ the wave propagation direction) in the following manner

$$D(\theta) = \frac{1}{N}\cos^{2m}\theta,$$

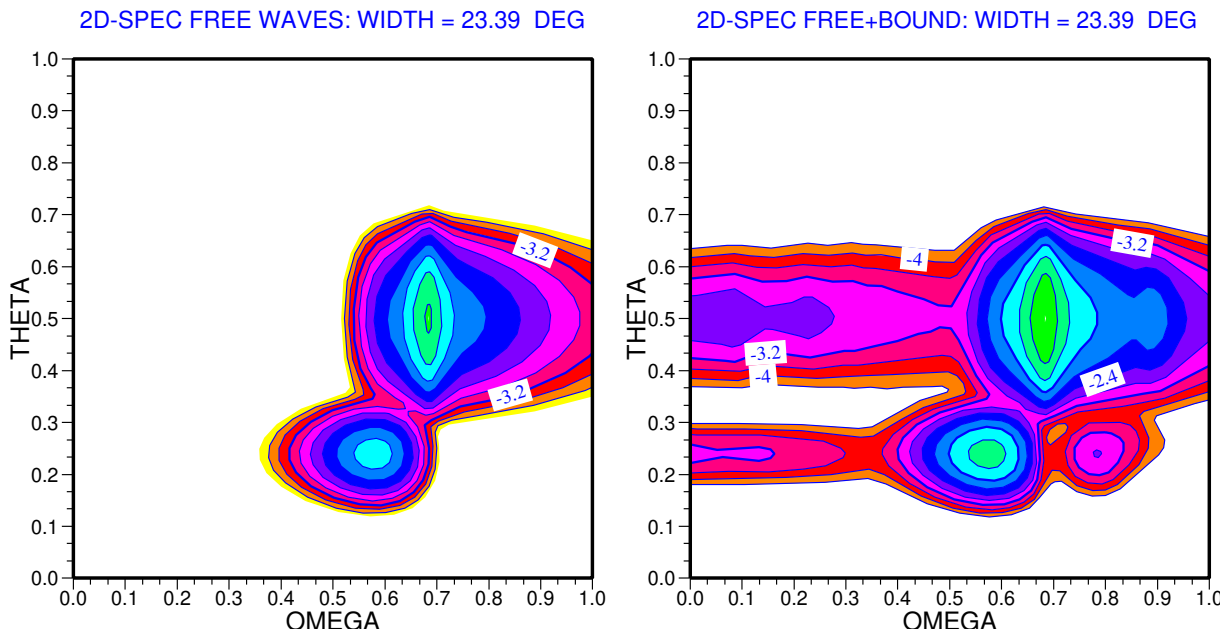where the normalisation factor $N = \pi(2m-1)!!/(2m)!!$. For the depth $D = 1.7$ m the dimensionless depth $k_0 D = 1.00$ at the peak of the spectrum indicating that shallow water effects are important for this case.

In order to illustrate the importance of the directional distribution Fig. 9.1 shows the sum of the free wave and second-order frequency spectrum for different directional width, ranging from a narrow swell to a broad windsea. The second-harmonic contribution to the spectrum is seen to depend to some extent on the directional width but clearly the level of the infra-gravity part of the spectrum depends in a sensitive manner on directional shape.

Figure 9.2 *Two-dimensional frequency-direction spectrum for a directional width of 24°. Plotted is $\log_{10} F(f, \theta)$ as function of normalised frequency number m/N_{fre} and directional number k/N_{ang}. The left panel shows the free-wave spectrum while the right panel shows the sum of the free-wave spectrum and the second-order spectrum.*

For one case, namely for a directional width of 23^0, the two-dimensional frequency direction spectrum is shown in Fig. 9.2. It is striking to see that the infra-gravity wave contribution seems to be much more narrow than the windsea spectrum, while it is also pointed out that the windsea peak is enhanced by the second-order effects.
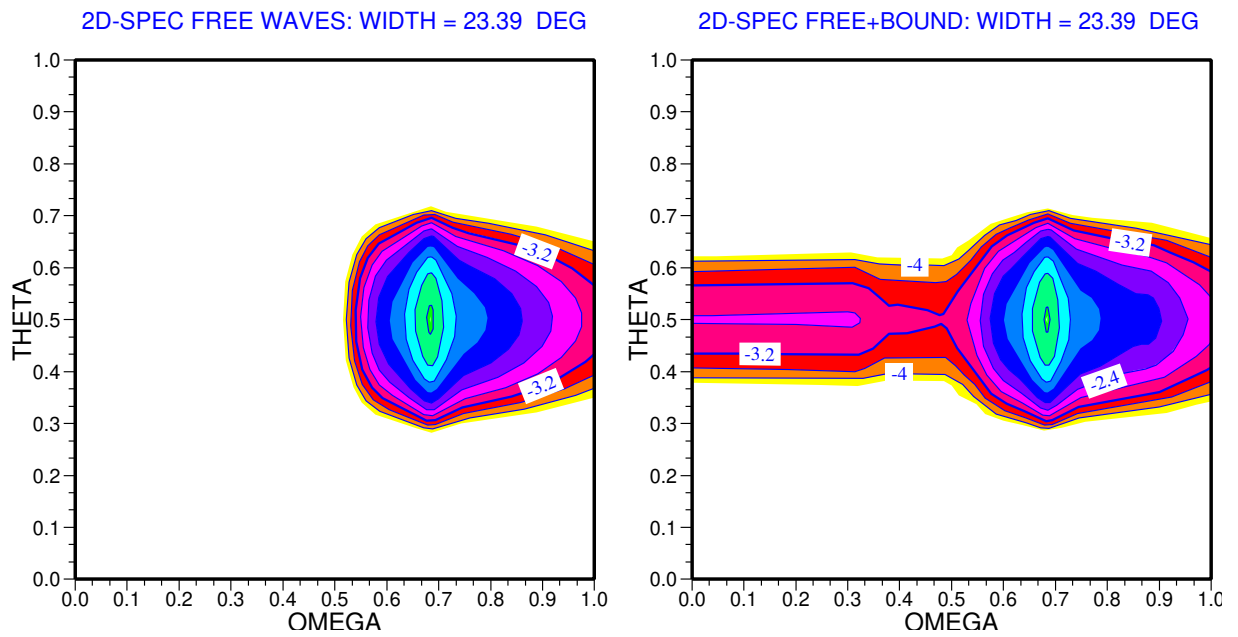

Figure 9.3 *Two-dimensional frequency-direction spectrum for a windsea with a width of 23° and a swell which travels at an angle of 90° with respect to the windsea.*

Thus far we have considered single peaked (windsea) spectra. The next interesting case is the one where there is a combination of windsea and swell. The windsea had the same parameters for the JONSWAP spectrum as before with a significant wave height of 72 cm while the swell spectrum had a Gaussian frequency spectrum, with a wave height of 25 cm and the same directional distribution as the windsea except that the directional width parameter was smaller by a factor of two, having a width of 12°. The swell travels at an angle of 90° with respect to the windsea and has an angular peak frequency of 1.5. The free wave spectrum and the sum of the free wave spectrum and the second-order spectrum are displayed for this case in Fig. 9.3. Considering the windsea and the swell part of the spectrum separately it is seen that the second-order corrections to the free wave parts have the expected shape. However, there is hardly any interaction between windsea and swell parts, i.e. the presence of swell hardly affects the shape of the windsea spectrum and vice versa. Regarding the windsea part this can immediately be verified by comparing Fig. 9.2 and Fig. 9.3. Presumably this is caused by the fact that in this case the two systems propagate at a really different angle of 90°. Indeed, it was checked that there was a stronger interaction between windsea and swell when the two systems were propagating in a similar direction, in particular when their energies were similar.

Finally, although the second-order corrections have been coded in an efficient manner, reaching speeds of the order of 2 Gflop, and although it is only called at output time, another optimisation was required in order to keep increases in computation times small, i.e. allowing an increase of cpu time by at most 5-6%. This was achieved by thinning the free wave spectrum in frequency and angular direction by a factor of two, and by calculating the second-order spectrum on the reduced grid only. An interpolation step was then performed to bring the required spectral information from the reduced to the full spectral grid.

This approach gives a speed-up of a factor of 16, but will inevitably result in loss of information. However, comparing Fig. 9.4, which shows the second-order spectrum calculated on the reduced grid, with Fig. 9.2 suggests that the loss of information is not too big. This was checked by comparing spectral moments obtained

Figure 9.4 *Two-dimensional frequency-direction spectrum for a windsea with a width of 23°, but now calculated on a reduced spectral grid (reduction factor = 2).*

from the full grid and the reduced grid, using an arbitrary archived free wave spectral global field, and the differences were found to be small.

Chapter 10

Wave model output parameters

Table of contents

10.1   INTRODUCTION

This document gives a short summary of the definition of ECMWF ocean wave model output parameters. Please refer to the official IFS documentation part VII for a full description of the wave model (http://www.ecmwf.int/en/forecasts/documentation-and-support/changes-ecmwf-model/ifs-documentation). The data are encoded in GRIB, edition 1. See table(10.1) for the full list of all available parameters

10.2   WAVE SPECTRA

There are two quantities that are actually computed at each grid point of the wave model, namely the two-dimensional (2-D) wave spectrum $F(f, \theta)$ and the total atmospheric surface stress τ_a for a given atmospheric forcing. In its continuous form, $F(f, \theta)$ describes how the wave energy is distributed as function of frequency f and propagation direction θ. In the numerical implementation of the wave model, F is discretised using $nfre$ frequencies and $nang$ directions. In the current analysis and deterministic forecast configuration $nfre = 36$ and $nang = 36$. Whenever possible, $F(f, \theta)$ is output and archived as parameter 251. It corresponds to the full description of the wave field at any grid point. It is however a very cumbersome quantity to plot as a

full field since it consists of $nfre \times nang$ values at each grid point. Nevertheless, it can plotted for specific locations. Figures 10.1 and 10.2 display the spectra at 6 different locations as indicated on Figure 10.3 (model bathymetry, parameter 219 is also shown). The two-dimensional wave spectrum is represented using a polar plot representation, where the radial coordinate represents frequency and the polar direction is the propagation direction of each wave component. The oceanographic convention is used, such that upwards indicates that waves are propagating to the North. The frequency spectrum, which indicates how wave energy is distributed in frequency, is obtained by integrating over all directions. From Figure 10.1, it clear that for many locations, the sea state is composed of many different wave systems.

10.3   INTEGRAL PARAMETERS DESCRIBING THE WAVE FIELD

In order to simplify the study of wave conditions, integral parameters are computed from some weighted integrals of $F(f, \theta)$ or its source terms. It is quite often customary to differentiate the wave components in the spectrum as windsea (or wind waves) and swell. Here, windsea is defined as those wave components that are still subject to wind forcing while the remaining part of the spectrum is termed swell, total swell if the full remaining part is considered as one entity or first, second or third swell partition when it is split into the 3 most energetic systems (see section on swell partitioning).

To a good approximation, spectral components are considered to be subject to forcing by the wind when

$$1.2 \times 28(u_*/c) \cos(\theta - \phi) > 1 \tag{10.1}$$

where u_* is the friction velocity ($u_*^2 = \frac{\tau_a}{\rho_{air}}$), ρ_{air} the surface air density, $c = c(f)$ is the phase speed as derived from the linear theory of waves and ϕ is the wind direction.

The integrated parameters are therefore also computed for windsea and swell by **only** integrating over the respective components of $F(f, \theta)$ that satisfies (10.1) or not (for windsea and total swell) or by integrating over the part of the spectrum that has been identified to belong to the first, second or third swell partition.

Let us define the moment of order n of F, m_n as the integral

$$m_n = \int \int \mathrm{d}f \mathrm{d}\theta \, f^n F(f, \theta) \tag{10.2}$$

and define the frequency spectrum $E(f)$ as

$$E(f) = \int \mathrm{d}\theta \, F(f, \theta) \tag{10.3}$$

The integrations are performed over all frequencies and directions or over a spectral sub-domain when the spectrum is split between windsea and swell or partitioned into main components. In the high-frequency range the usual Phillips spectral shape (f^{-5}) is used where the Phillips parameter is determined by the spectral level at the last discretised frequency bin. Then the relevant integral parameters are:

10.3.1   Significant Wave Height

By definition, the significant wave height H_s is defined as

$$H_s = 4\sqrt{m_0} \tag{10.4}$$

Hence the definition of parameters 229. As an example, Figure 10.4 shows the significant wave height, mean wave direction and energy mean wave period corresponding to the synoptic situation as shown in Figure 10.5.

When the spectrum is split between windsea and total swell using (10.1), the respective significant wave height can be obtained, hence 234, 237 (Figure 10.10). If the total swell spectrum is partitioned into its 3 main components, the integrals over the respective domain yield 121, 124, 127 (see below). A simpler approach into the detection of low frequency waves is to integrate the spectrum only for all spectral components with frequency below 0.1 Hz (i.e. with periods above 10s) and to convert this into a corresponding significant wave height for all waves components with period above 10 seconds, H_{10}, hence parameter 120. It is quite common to plot the square of ratio of H_{10} to H_s (namely the ratio of the wave energy of all waves with periods larger

than 10s to the total wave energy) as shown in Figure 10.6. With the introduction of CY43R1 (November 2016), the concept of H_{10} was further extended by only considering waves within a given period band (10-12, 12-14, 14-17, 17-21, 21-25, 25-10 sec.), hence parameters 114 to 119. Figure 10.7 shows T+180 forecast for significant wave height for all waves (coloured contours) and the corresponding new parameter, the significant wave height for all waves with periods between 21 and 25 seconds (colour shadings). Even though the highest significant wave heights are still confined to the storm location, in the Atlantic south of Iceland, long waves from that storm, as depicted by this new parameter, are already affecting coastlines from Iberia to South Greenland.

10.3.2 Mean Periods

The mean period T_{m-1} is based on the moment of order -1, that is

$$T_{m-1} = m_{-1}/m_0 \tag{10.5}$$

Hence the definition of parameters 232, 236, 239, and the partitioned 123, 126, 129.

T_{m-1} is also commonly known as the energy mean wave period. Together with H_s, it can be used to determine the wave energy flux per unit of wave-crest length in deep water, also known as the wave power per unit of wave-crest length P (see 10.3.6)

In order to look at different aspects of the wave field, other moments can be used to define a mean period.

Periods can be based on the first moment T_{m1} given by

$$T_{m1} = m_0/m_1 \tag{10.6}$$

Hence the definition of parameters 220, 223, and 226. T_{m1} is essentially the reciprocal of the mean frequency. It can be used to estimate the magnitude of Stokes drift transport in deep water (see Stokes drift) and periods based on the second moment T_{m2} given by

$$T_{m2} = \sqrt{m_0/m_2} \tag{10.7}$$

Hence the definition of parameters 221, 224, and 227. T_{m2} is also known as the zero-crossing mean wave period as it corresponds to the mean period that is determined from observations of the sea surface elevation using the zero-crossing method.

10.3.3 Peak Period

The peak period is defined only for the total sea. It is defined as the reciprocal of the peak frequency. It is obtained from a parabolic fit around the discretised maximum of two-dimensional wave spectrum, Hence parameter 231 (Figure 10.8).

10.3.4 Mean Wave Direction

By weighting $F(f,\theta)$, one can also define a mean direction $\langle\theta\rangle$ as

$$\langle\theta\rangle = \text{atan}(SF/CF) \tag{10.8}$$

where SF is the integral of $\sin(\theta)\,F(f,\theta)$ over f and θ and CF is the integral of $\cos(\theta)\,F(f,\theta)$ over f and θ. Hence the definition of parameters 230, 235, 238, and the partitioned 122, 125, 128. Note that in grib 1, the mean direction parameters are encoded using the meteorological convention (0 means from North, 90 from East).

10.3.5 Wave Directional Spread

Information on the directional distribution of the different wave components can be obtained from the mean directional spread σ_θ given by

$$\sigma_\theta = \sqrt{2(1 - M_1)} \tag{10.9}$$

where

For total sea:

$$M_1 = I_1/E_0 \qquad (10.10)$$

I_1 is the integral of $\cos(\theta - \langle\theta\rangle(f)) F(f, \theta)$ over f and θ, where $\langle\theta\rangle(f)$ is the mean direction at frequency f:

$$\langle\theta\rangle(f) = \mathrm{atan}(sf(f)/cf(f)) \qquad (10.11)$$

with $sf(f)$ the integral of $\sin(\theta) F(f, \theta)$ over θ only and $cf(f)$ is the integral of $\cos(\theta) F(f, \theta)$ over θ only. Hence the definition of parameter 222.

For wind waves and swell:

$$M_1 = I_p/E(f_p) \qquad (10.12)$$

I_p is the integral of $\cos(\theta - \langle\theta\rangle(f_p)) F(f_p, \theta)$ over θ only, f_p is the frequency at the spectral peak and $\langle\theta\rangle(f_p)$ is given by (10.11), where $F(f_p, \theta)$ is still split in all calculations using (10.1) (including in $E(f_p)$). Hence the definition of parameters 225, 228.

Note: As defined by (10.9), the mean directional spread σ_θ takes values between 0 and $\sqrt{2}$, where 0 corresponds to a uni-directional spectrum ($M_1 = 1$) and $\sqrt{2}$ to a uniform spectrum ($M_1 = 0$).

Figure 10.9 shows the directional spread for total sea, mean wave direction and zero-crossing mean wave period corresponding to the synoptic situation as shown in Figure 10.5. The plot highlights areas where the sea state is composed of different wave systems as shown in Figures 10.1 and 10.2.

10.3.6 Wave Energy Flux

Also known as the wave power per unit of wave-crest length P, the wave energy flux per unit of wave-crest length in deep water can be determined from T_{m-1} and H_s,

$$P = \frac{\rho_w g^2}{64\pi} T_{m-1} H_s^2 \qquad (10.13)$$

where ρ_w is the water density and g the acceleration due to gravity.

The wave energy flux is formally a vector, which is found by integrating the flux of each spectral components:

$$\mathbf{P} = \rho_w g \int_0^{2\pi} \int_0^\infty d\omega d\theta\, \mathbf{v}_g F(\omega, \theta), \qquad (10.14)$$

where $\mathbf{v}_g$ is the group velocity of the waves. In deep water, the magnitude of (10.14) can be shown to be equivalent to (10.13) Since CY43R1 (November 2016), (10.14) is computed, and the magnitude and the mean direction are output to produce parameter 112 and 113. The energy flux mean direction is encoded using the meteorological convention.

10.3.7 Spectral Partitioning

Traditionally, the wave model has separated the 2D-spectrum into a windsea and a total swell part (see above). Figure 10.10 shows the windsea and total swell significant wave height and mean wave direction corresponding to the synoptic situation as shown in Figure 10.5. However, in many instances, the swell part might actually be made up of different swell systems. Comparing the wave spectra in Figures 10.1 and 10.2 with the simple decomposition shown in Figure 10.10, it is clear that for many locations, the total swell is made up of more that one distinct wave system.

We have adapted and optimized the spectral partitioning algorithm of Hanson and Phillips (2001) to decompose the **SWELL** spectrum into swell systems. It uses the fact that the spectra are model spectra for which a high frequency tail has been imposed and it excludes from the search the windsea part (the original partitioning method decomposes the full two-dimensional spectrum). The three most energetic swell systems are retained (for most cases, up to 3 swell partitions was found to be enough) and the spectral variance contained in the other partitions (if any) is redistributed proportionally to the spectral variance of the three selected partitions. Because it is only the swell spectrum that is partitioned, some spectral components can end up being unassigned

to any swell partitions, their variance should be assigned to the windsea if they are in the wind directional sector, but it is currently **NOT** done because the old definition of the windsea and the total swell was not modified, otherwise they are redistributed proportionally to the spectral variance of the three selected partitions.

Based on the partitioned spectrum, the corresponding significant wave height (10.4), mean wave direction (10.8), and mean frequency (10.5) are computed.

So, by construct, the 2D-spectrum is decomposed into windsea (using the old definition) and up to three swell partitions, each described by significant wave height, mean wave period and mean direction. Figure 10.11 shows how the partitioning has decomposed the spectra. Compared to Figure 10.10, it can be seen that the new partitioning scheme gives a better representation of the full 2-D spectra as given in Figures 10.1 and 10.2. Note that the swell partitions are labelled first, second and third based on their respective wave height. Therefore, there isn't any guarantee of spatial coherence (first might be from one system at one location and another one at the neighbouring location). It is **ONLY** by taking the windsea and the 3 partitioned swell systems that one can reconstruct the main feature of the 2D-spectrum! This is obviously an approximation as the true sea state is only entirely described by the 2-D spectrum.

10.3.8   Mean Square Slope

An integrated parameter which can be related to the average slope of the waves is the mean square slope which is only defined for the total sea as the integral of $k^2 F(f, \theta)$ over f and θ, where k is the wave number as given by the linear dispersion relation. Hence parameter 244 (Figure 10.12).

10.4 FORCING FIELDS

10.4.1 10 m Neutral Wind Speed

Due to different spatial grids, the forcing 10m neutral winds are interpolated to the wave model grid. Furthermore, in case of analysed fields, the radar altimeter data assimilation scheme is such that it produces increments for wave heights but also for wind speeds. Hence, the wind speed which is actually seen by the wave model (U_{10}) is different than the 10 m neutral wind speed provided by the atmospheric model.

By definition, the air-side friction velocity u_* is related to the norm of the atmospheric surface stress $\|\boldsymbol{\tau_a}\|$

$$\|\boldsymbol{\tau_a}\| = \sqrt{\tau_x^2 + \tau_y^2} = \rho_{air} u_*^2 \tag{10.15}$$

where ρ_{air} is the surface air density, and (τ_x, τ_y) are the x- and y-components of the atmospheric surface stress.

Hence,

$$u_* = \frac{\left[\tau_x^2 + \tau_y^2\right]^{\frac{1}{4}}}{\sqrt{\rho_{air}}} \tag{10.16}$$

The norm of the vertical neutral wind profile (U_z, V_z) is defined as

$$\|\mathbf{U}(z)\| = \frac{u_*}{\kappa} \ln\left(\frac{z}{z_0}\right) \tag{10.17}$$

where κ is the von Kármán constant, and z_0 the surface roughness length scale for momentum.

τ_x, τ_y, z_0 are prognostic variables in the IFS, whereas the surface air density ρ_{air} can be determined from values of pressure, temperature and humidity at the lowest model level (see 10.22).

By definition, the neutral winds are in the direction of the surface stress, namely

$$U_z = \|\mathbf{U}(z)\| \frac{\tau_x}{\|\boldsymbol{\tau_a}\|}, V_z = \|\mathbf{U}(z)\| \frac{\tau_y}{\|\boldsymbol{\tau_a}\|} \tag{10.18}$$

Using (10.16), with (10.17) and (10.15) yields

$$U_z = \frac{1}{\kappa} \frac{\frac{\tau_x}{\sqrt{\rho_{air}}}}{\left[\tau_x^2 + \tau_y^2\right]^{\frac{1}{4}}} \ln\left(\frac{z}{z_0}\right), V_z = \frac{1}{\kappa} \frac{\frac{\tau_y}{\sqrt{\rho_{air}}}}{\left[\tau_x^2 + \tau_y^2\right]^{\frac{1}{4}}} \ln\left(\frac{z}{z_0}\right) \tag{10.19}$$

This can be re-written as

$$U_z = \frac{1}{\kappa} \frac{\frac{\tau_x}{\rho_{air}}}{\left[\left(\frac{\tau_x}{\rho_{air}}\right)^2 + \left(\frac{\tau_y}{\rho_{air}}\right)^2\right]^{\frac{1}{4}}} \ln\left(\frac{z}{z_0}\right), V_z = \frac{1}{\kappa} \frac{\frac{\tau_y}{\rho_{air}}}{\left[\left(\frac{\tau_x}{\rho_{air}}\right)^2 + \left(\frac{\tau_y}{\rho_{air}}\right)^2\right]^{\frac{1}{4}}} \ln\left(\frac{z}{z_0}\right) \tag{10.20}$$

This last form is what is coded in the IFS.

At every coupling time, (10.20) is used for $z = 10m$ (U_{10}, V_{10}) with the updated values for τ_x, τ_y, z_0 and ρ_{air} to provide the neutral 10m wind that is used to force ECWAM. These components are interpolated onto the ECWAM grid and archived as wave model parameters as magnitude and direction (parameters 245 and 249) (Figure 10.5).

Over the ocean, z_0 is itself a function of the sea state (3.12). Because the IFS and ECWAM do not share the same grid, nor the same land-sea mask, there will be some values of τ_x, τ_y, z_0 and ρ_{air} that correspond to land values. For this reason, the contribution from the Turbulent Orographic Form Drag (TOFD) parametrisation is subtracted from the total value of the surface stress prior to applying (10.20) because it is intended to only be valid over land.

10.4.2 Drag Coefficient

In the wave model, the surface stress depends on the waves. This feature is archived via the drag coefficient C_d (parameter 233) which relates the surface stress to the square of the neutral wind speed, $u_*^2 = C_d \|\mathbf{U_{10}}\|^2$ (Figure 10.13). Note that currently, u_* is not archived as such and needs to be computed with the previous relation.

10.4.3 Free convective velocity scale and air density

Strictly speaking the free convective velocity (w_*) (parameter 208) and the air density (ρ_{air}) (parameter 209) are not wave model parameters, they are part of the atmospheric forcing. Nevertheless, they are archived on the same model grid as the wave model, and are only available over the oceans, as defined by the wave model land/sea mask. The free convection velocity scale w_* is used to parameterise the impact of wind gustiness on the wave growth which is also proportional to the ratio of air density to water density (currently assumed constant). See section 3.2.1 for more details

The free convection velocity scale w_* is computed using

$$w_* = u_* \left\{ \frac{1}{\kappa} \left(\frac{z_i}{-L} \right) \right\}^{1/3} \quad for \ L < 0 \quad and \quad w_* = 0 \quad for \ L >= 0 \tag{10.21}$$

where u_* is the friction velocity ($u_*^2 = \frac{\tau_a}{\rho_{air}}$), κ is the von Kármán constant, z_i is the height of the lowest inversion, L is the Monin-Obukhov length. The quantity z_i/L, which is a measure for the atmospheric stability, is readily available from the atmospheric model, and the surface air density ρ_{air} is given by

$$\rho_{air} = \frac{P}{RT_v} \tag{10.22}$$

where P is the atmospheric pressure, $R \simeq 287.04 \, \mathrm{J\,kg^{-1}\,K^{-1}}$ is a constant defined as $R = R_+/m_a$, with R_+ the universal gas constant ($R_+ \simeq 8314.36 \, \mathrm{J\,kmol^{-1}\,K^{-1}}$) and m_a is the molecular weight of the dry air ($\simeq 28.966 \, \mathrm{kg\,kmol^{-1}}$), and T_v is the virtual temperature. The virtual temperature can be related to the actual air temperature, T, and the specific humidity, q, by: $T_v \simeq (1 + 0.6078q)T$. To avoid using diagnostic variables, the pressure, the temperature and humidity at the lowest model level are now used.

Figure 10.14 shows a combined map of the different fields that make up the forcing to the ECMWF wave model (U_{10}, ρ_{air}, w_*) .

10.5   INTERACTION WITH THE OCEAN CIRCULATION

10.5.1   Stokes drift

The surface Stokes drift $\mathbf{u}_{st}$ is defined by the following integral expression

$$\mathbf{u}_{st} = \int df d\theta \frac{2gk}{\omega \tanh(2kD)} \mathbf{k} F(f, \theta) \tag{10.23}$$

The integration is performed over all frequencies and directions. In the high-frequency range the usual Phillips spectral shape is used where the Phillips parameter is determined by the spectral level at the last frequency bin, while it is tacitly assumed that these frequencies are so high that shallow water effects are unimportant. This defines parameters 215 and 216.

Figure 10.15 shows the ratio (in percentage) of the surface Stokes drift magnitude to the 10m wind speed (colour shading) and the actual surface Stokes drift (colour arrows) corresponding to the synoptic situation as shown in Figure 10.5 for wind. This ratio shows that the surface Stokes drift cannot easily be represented as a fixed ratio of the 10m wind speed.

10.5.2   Momentum and energy flux into ocean

In order to be able to give a realistic representation of the mixing processes in the surface layer of the ocean, a reliable estimate of energy and momentum fluxes to the ocean column is required. As energy and momentum flux depend on the spectral shape, the solution of the energy balance equation is required. It reads

$$\frac{\partial}{\partial t} F + \frac{\partial}{\partial \mathbf{x}} \cdot (\mathbf{v}_g F) = S_{in} + S_{nl} + S_{diss} + S_{bot}, \tag{10.24}$$

where $F = F(\omega, \theta)$ is the two-dimensional wave spectrum which gives the energy distribution of the ocean waves over angular frequency ω and propagation direction θ. Furthermore, $\mathbf{v}_g$ is the group velocity and on the right hand side there are four source terms. The first one, S_{in} describes the generation of ocean waves by wind and therefore represents the momentum and energy transfer from air to ocean waves. The third and fourth term describe the dissipation of waves by processes such as white-capping, large scale breaking eddy-induced damping and bottom friction, while the second term denotes nonlinear transfer by resonant four-wave interactions. The nonlinear transfer conserves total energy and momentum and is important in shaping the wave spectrum and in the spectrum down-shift towards lower frequencies (see Chapter 2 for more details).

Let us first define the momentum and energy flux. The total wave momentum $\mathbf{M}$ depends on the variance spectrum $F(\omega, \theta)$ and is defined as

$$\mathbf{M} = \rho_w g \int_0^{2\pi} \int_0^{\infty} d\omega d\theta \frac{\mathbf{k}}{\omega} F(\omega, \theta), \tag{10.25}$$

where ρ_w is the water density and g the acceleration due to gravity. The momentum fluxes to and from the wave field are given by the rate of change in time of wave momentum, and one may distinguish different momentum fluxes depending on the different physical processes. For example, making use of the energy balance equation (10.24) the wave-induced stress is given by

$$\boldsymbol{\tau}_{in} = \rho_w g \int_0^{2\pi} \int_0^{\infty} d\omega d\theta \frac{\mathbf{k}}{\omega} S_{in}(\omega, \theta), \tag{10.26}$$

while the dissipation stress is given by

$$\boldsymbol{\tau}_{diss} = \rho_w g \int_0^{2\pi} \int_0^{\infty} d\omega d\theta \frac{\mathbf{k}}{\omega} S_{diss}(\omega, \theta), \tag{10.27}$$

Similarly, the energy flux from wind to waves is defined by

$$\Phi_{in} = \rho_w g \int_0^{2\pi} \int_0^{\infty} d\omega d\theta \, S_{in}(\omega, \theta), \tag{10.28}$$

and the energy flux from waves to ocean, Φ_{diss}, is given by

$$\Phi_{diss} = \rho_w g \int_0^{2\pi} \int_0^{\infty} d\omega d\theta \, S_{diss}(\omega, \theta). \tag{10.29}$$

It is important to note that while the momentum fluxes are mainly determined by the high-frequency part of the wave spectrum, the energy flux is to some extent also determined by the low-frequency waves.

The prognostic frequency range is limited by practical considerations such as restrictions on computation time, but also by the consideration that the high-frequency part of the dissipation source function is not well-known. In the ECMWF wave model the high-frequency limit $\omega_c = 2\pi f_c$ is set as

$$f_c = \min\{f_{\max}, 2.5\langle f\rangle_{\text{windsea}}\} \tag{10.30}$$

Thus, the high-frequency extent of the prognostic region is scaled by the mean frequency $\langle f\rangle_{\text{windsea}}$ of the local windsea. A dynamic high-frequency cut-off, f_c, rather than a fixed cut-off at $f_{\max}$, corresponding to the last discretised frequency, is necessary to avoid excessive disparities in the response time scales within the spectrum.

In the diagnostic range, $\omega > \omega_c$, the wave spectrum is given by Phillips' ω^{-5} power law. For this to be the case, it is assumed that there is a balance between input, dissipation and the flux due to non linear wave interactions. In practice this means that all energy and momentum going into the high-frequency range of the spectrum, either by wind input or non-linear transfer, is dissipated, and is therefore directly transferred to the ocean column.

$$\int_0^{2\pi} \int_{\omega_c}^{\infty} d\omega d\theta \, \frac{\mathbf{k}}{\omega} \left(S_{in} + S_{diss} + S_{NL}\right) = 0, \tag{10.31}$$

and

$$\int_0^{2\pi} \int_{\omega_c}^{\infty} d\omega d\theta \, \left(S_{in} + S_{diss} + S_{NL}\right) = 0, \tag{10.32}$$

The momentum flux to the ocean column, denoted by $\boldsymbol{\tau}_{oc}$, is the sum of the flux transferred by turbulence across the air-sea interface which was not used to generate waves $\boldsymbol{\tau}_a - \boldsymbol{\tau}_{in}$ and the momentum flux transferred by the ocean waves due to wave breaking $\boldsymbol{\tau}_{diss}$.

As a consequence, $\boldsymbol{\tau}_{oc} = \boldsymbol{\tau}_a - \boldsymbol{\tau}_{in} - \boldsymbol{\tau}_{diss}$. Utilizing the assumed balance at the high-frequencies (10.31) (see also section 3.3) and the conservation of momentum for S_{NL} when integrated over all frequencies and directions, one finds

$$\boldsymbol{\tau}_{oc} = \boldsymbol{\tau}_a - \rho_w g \int_0^{2\pi} \int_0^{\omega_c} d\omega d\theta \, \frac{\mathbf{k}}{\omega} \left(S_{in} + S_{diss} + S_{NL}\right), \tag{10.33}$$

where $\boldsymbol{\tau}_a$ is the atmospheric stress, whose magnitude is given by $\tau_a = \rho_{air} u_*^2$, with u_* the air side friction velocity.

Ignoring the direct energy flux from air to ocean currents, because it is small, the energy flux to the ocean, denoted by Φ_{oc}, is therefore given by $-\Phi_{diss}$. Utilizing the assumed high-frequency balance (10.32) and the conservation of energy when S_{NL} is integrated over all frequencies and directions, one therefore obtains

$$\Phi_{oc} = \Phi_{in} - \rho_w g \int_0^{2\pi} \int_0^{\omega_c} d\omega d\theta \, \left(S_{in} + S_{diss} + S_{NL}\right), \tag{10.34}$$

where Φ_{in} is given by (10.28) and can be written as

$$\Phi_{in} = \rho_w g \int_0^{2\pi} \int_0^{\omega_c} d\omega d\theta \, S_{diss}, + \rho_w g \int_0^{2\pi} \int_{\omega_c}^{\infty} d\omega d\theta \, S_{in} \qquad (10.35)$$

The high frequency $(\omega > \omega_c)$ contribution to the energy flux

$$\Phi_{in_{hf}} = \rho_w g \int_0^{2\pi} \int_{\omega_c}^{\infty} d\omega d\theta \, S_{in} \qquad (10.36)$$

is parameterised following the same approach as for the kinematic wave induced stress (5.8)

$$\Phi_{in_{hf}} = \rho_a \frac{(2\pi)^4 f_c^5}{g} \, u_*^{\,2} \int_0^{2\pi} d\theta \, F(f_c, \theta)[\max\left(\cos(\theta - \phi), 0\right)]^2 \quad \frac{\beta_m}{\kappa^2} \int_{\omega_c}^{\infty} \frac{d\omega}{\omega^2} \mu_{hf} \ln^4(\mu_{hf}), \qquad (10.37)$$

In (10.37), the integral over directions can be evaluated using the prognostic part of the spectrum, whereas the second integral is only function of u_* and the Charnock parameter. It can therfore be tabulated beforehand. Note that the integration is bounded because $\mu_{hf} <= 1$

$$\Phi_{oc_{hf}} = \frac{\beta_m}{\kappa^2} \sqrt{\frac{z_0}{g}} \int_{Y_c}^1 \frac{dY}{Y^2} \mu_{hf} \ln^4(\mu_{hf}), \quad Y_c = \max\left(\omega_c, x_0 \frac{g}{u_*}\right) \sqrt{\frac{z_0}{g}} \qquad (10.38)$$

where for typical values of the Charnock parameter, $x_0 \sim 0.05$. Since CY45R1 (June 2018), it was found that it was as numerically efficient to compute the integral in (10.38) following the variable transformation $X = \ln(Y)$ and only a few discretised points using the Simpson integration method.

The archived energy fluxes are normalized by the product of the air density ρ_{air} and the cube of the friction velocity in the air (u_*). Hence the normalized energy flux into waves (parameter 211) is obtained from (10.35) divided by $\rho_{air} u_*^3$. Similarly the normalized energy flux into ocean (parameter 212) is obtained from normalizing (10.34).

The normalized stress into ocean (parameter 214) is derived from (10.33) by dividing it with the atmospheric stress $\tau_a = \rho_{air} u_*^2$.

Figure 10.16 shows both dimensional energy and momentum fluxes into the ocean.

10.6 FREAK WAVE PARAMETERS

The parameters that have been described so far all provide information on the average properties of the sea state. In recent years, there has been a considerable effort to understand extreme events such as freak waves. An individual wave is regarded as a freak wave when its height is larger than twice the significant wave height. Clearly, in order to be able to describe such extreme events, knowledge on the statistical properties of the sea surface is required. Recent work has presented a general framework that relates the shape of the probability distribution function of the surface elevation to the mean sea state as described by the two-dimensional frequency spectrum. Under normal circumstances, the surface elevation pdf has approximately a Gaussian shape, but in the exceptional circumstances that the waves are sufficiently nonlinear and that the wave spectrum is narrow in **both** frequency and direction, considerable deviations from Normality may occur, signalling increased probability for freak waves.

10.6.1 Kurtosis of the Sea Surface Elevation

The deviations from Normality are measured in terms of the kurtosis C_4 (parameter 252) of the surface elevation. The determination of this parameter from the wave spectrum is described in Chapter 8 of part VII of the IFS documentation. It has been revised a few times, the latest formulation is based on CY46R1 and it is shown that

$$C_4 = C_4^{dyn} + C_4^{bound} \tag{10.39}$$

where C_4^{dyn} is given by 8.24 and C_4^{bound} by 8.22

In the operational model, the kurtosis C_4 is restricted to the range $-0.25 < C_4 < 0.25$.

10.6.2 Benjamin-Feir Index

Note that the archived parameter (253) is the square of BFI as given by 8.31 The Benjamin-Feir Index is the ratio of the integral wave steepness ϵ and δ_ω the relative width of the frequency.

The relative width of the frequency spectrum is estimated by using Goda's peakedness factor Q_p (parameter 254) defined as

$$Q_p = \frac{2}{m_0^2} \int d\omega \, \omega E^2(\omega) \tag{10.40}$$

with $E(\omega)$ the angular frequency spectrum and the integration domain $\mathcal{D}$ consists of all frequencies for which $E(\omega) > 0.4 \, E(\omega_p)$ (Janssen and Bouws (1986)).

10.6.3 Skewness of the Sea Surface Elevation

Since CY40R3, the skewness of the surface elevation C_3 was introduced (parameter 207). This is in particular relevant for the contribution of bound waves to the deviations of statistics from Normality, as bound waves give rise to a considerable skewness. On the other hand, it should be noted that the skewness of free waves is very small and therefore for really extreme events the skewness correction to the wave height is not so important. However, on average, the bound waves will determine the statistics of waves and, therefore, in order to have an accurate description of the average conditions as well the skewness effect needs to be included.

$$C_3 = C_3^{bound} \tag{10.41}$$

and C_3^{bound} is given in by 8.22

In the operational model, the kurtosis C_3 is restricted to the range $0.0 < C_3 < 0.25$.

10.6.4 Maximum Single Wave Height

Finally, these deviations form Normality can be used to come up with an expression for the expectation value of the maximum wave height H_{max} (parameter 218).

$$H_{max} = \langle H_{max}\rangle H_s, \tag{10.42}$$

with H_s the significant wave height (10.4) and $\langle H_{max}\rangle$ is given by 8.41

Figure 10.17 shows the ratio of H_{max} to H_s corresponding to the synoptic situation as shown in Figure 10.5.

10.7 MISCELLANEOUS

10.7.1 Radar Altimeter Data

These parameters are only for diagnostics carried out at ECMWF.

Even though altimeter data are processed observations and thus not as such wave model results, their processing has required some information from the model.

Following a quality control procedure which discards all spurious data, the raw altimeter wave height data, which are available in a ± 3 hours time window, is collocated with the closest model grid point. The average value is computed for all grid points with at least two individual observations. The averaged data are then archived on the same grid as all wave model fields as parameter 246.

Before these gridded altimeter wave heights are presented to the wave model assimilation scheme, corrections are performed which depend on the type of Altimeter instrument. For example, however because of a known underestimation of significant wave height by the ERS-2 satellite, which is due to the inherent non Gaussian distribution of the sea surface elevation and the method how wave height is obtained from the waveform, a correction is derived from the model spectra which is applied to the altimeter data. Also data from the Altimeters on board of Envisat and Jason-1 are bias corrected. The correction is obtained from a comparison with buoy wave height data. The corrected data are used by the assimilation scheme and are archived as parameter 247.

The altimeter range observation is also affected by the non gaussianity of the sea surface elevation. The correction is a fraction of the observed wave height, where the fraction depends on the nonlinearity of the sea surface. This number is also collocated with the wave model grid and archived as parameter 248.
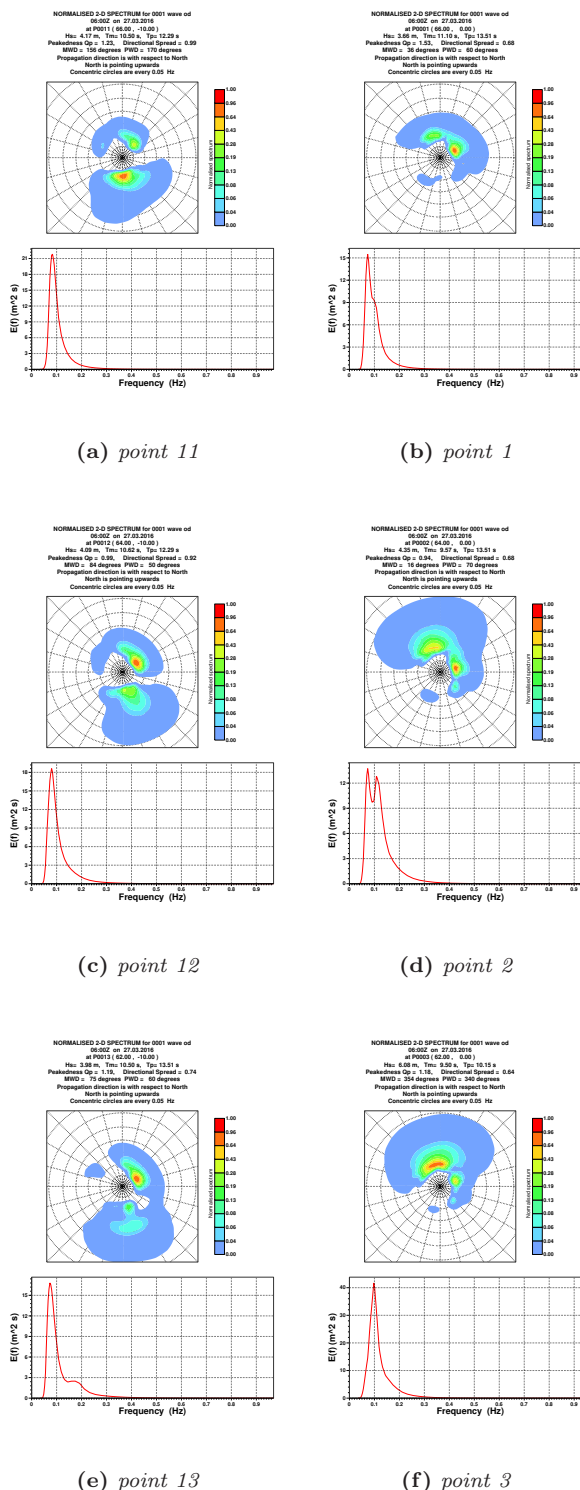
Table 10.1 *Archived parameters of the ECMWF wave forecasting system.*

Code Figure	Mars Abbrev.	Field	Units
140112	WEFXM	Wave Energy Flux magnitude	W/m
140113	WEFXD	Wave Energy Flux mean direction	°
140114	H1012	Significant wave height of all waves with period between 10 and 12 s	m
140115	H1214	Significant wave height of all waves with period between 12 and 14 s	m
140116	H1417	Significant wave height of all waves with period between 14 and 17 s	m
140117	H1721	Significant wave height of all waves with period between 17 and 21 s	m
140118	H2125	Significant wave height of all waves with period between 21 and 25 s	m
140119	H2530	Significant wave height of all waves with period between 25 and 30 s	m
140120	SH10	Significant wave height of all waves with period larger than 10s	m
140121	SWH1	Significant wave height of first swell partition	m
140122	MWD1	Mean wave direction of first swell partition	°
140123	MWP1	Mean wave period of first swell partition	s
140124	SWH2	Significant wave height of second swell partition	m
140125	MWD2	Mean wave direction of second swell partition	°
140126	MWP2	Mean wave period of second swell partition	s
140127	SWH3	Significant wave height of swell third partition	m
140128	MWD3	Mean wave direction of swell third partition	°
140129	MWP3	Mean wave period of swell third partition	s
140207	WSS	Wave Spectral Skewness	-
140208	WSTAR	Free convective velocity scale over the oceans	m/s
140209	RHOAO	Air density over the oceans	kg/m^3
140211	PHIAW	Normalized energy flux into waves	-
140212	PHIOC	Normalized energy flux into ocean	-
140214	TAUOC	Normalized stress into ocean	-
140215	UST	u-component of Stokes drift	m/s
140216	VST	v-component of Stokes drift	m/s
140217	TPM	Expected Period for H_{max}	s
140218	HMAX	Expected H_{max} over 3 hour period	m
140219	DPTH	Bathymetry as used by operational Wave Model	m
140220	MP1	Mean wave period from 1st moment	s
140221	MP2	Mean wave period from 2nd moment	s
140222	WDW	wave spectral directional width	-
140223	P1WW	Mean wave period from 1st moment of wind waves	s
140224	P2WW	Mean wave period from 2nd moment of wind waves	s
140225	DWWW	Wave spectral directional width of wind waves	-
140226	P1PS	Mean wave period from 1st moment of total swell	s
140227	P2PS	Mean wave period from 2nd moment of total swell	s
140228	DWPS	Wave spectral directional width of total swell	-
140229	SWH	Significant wave height	m
140230	MWD	Mean wave direction	°
140231	PP1D	Peak period of 1-D spectra	s
140232	MWP	Mean wave period	s
140233	CDWW	Coefficient of drag with waves	-
140234	SHWW	Significant height of wind waves (windsea)	m
140235	MDWW	Mean direction of wind waves (windsea)	°
140236	MPWW	Mean period of wind waves (windsea)	s
140237	SHPS	Significant height of total swell	m
140238	MDPS	Mean direction of total swell	°
140239	MPPS	Mean period of total swell	s
140244	MSQS	Mean square slope	-
140245	WIND	10 m neutral wind modified by wave model	m/s

Table 10.1 *Archived parameters of the ECMWF wave forecasting system.*

Code Figure	Mars Abbrev.	Field	Units
140246	AWH	Gridded altimeter wave height	m
140247	ACWH	Gridded corrected altimeter wave height	m
140248	ARRC	Gridded altimeter range relative correction	m
140249	DWI	10 m wind direction	$^\circ$
140251	2DFD	2-D wave spectra	m^2s/rad
140252	WSK	Kurtosis	-
140253	BFI	The square of the Benjamin-Feir Index	-
140254	WSP	Goda's Peakedness parameter	-

(a) *point 11*

(b) *point 1*

(c) *point 12*

(d) *point 2*

(e) *point 13*

(f) *point 3*

Figure 10.1 *Normalised 2d spectra (top of each panel) and frequency spectra (bottom of each panel) on 23 March 2016, 6 UTC, for locations shown in Figure 10.3. The 2-D spectra were normalised by their respective maximum value. The concentric circles in the polar plots are spaced every 0.05 Hz*
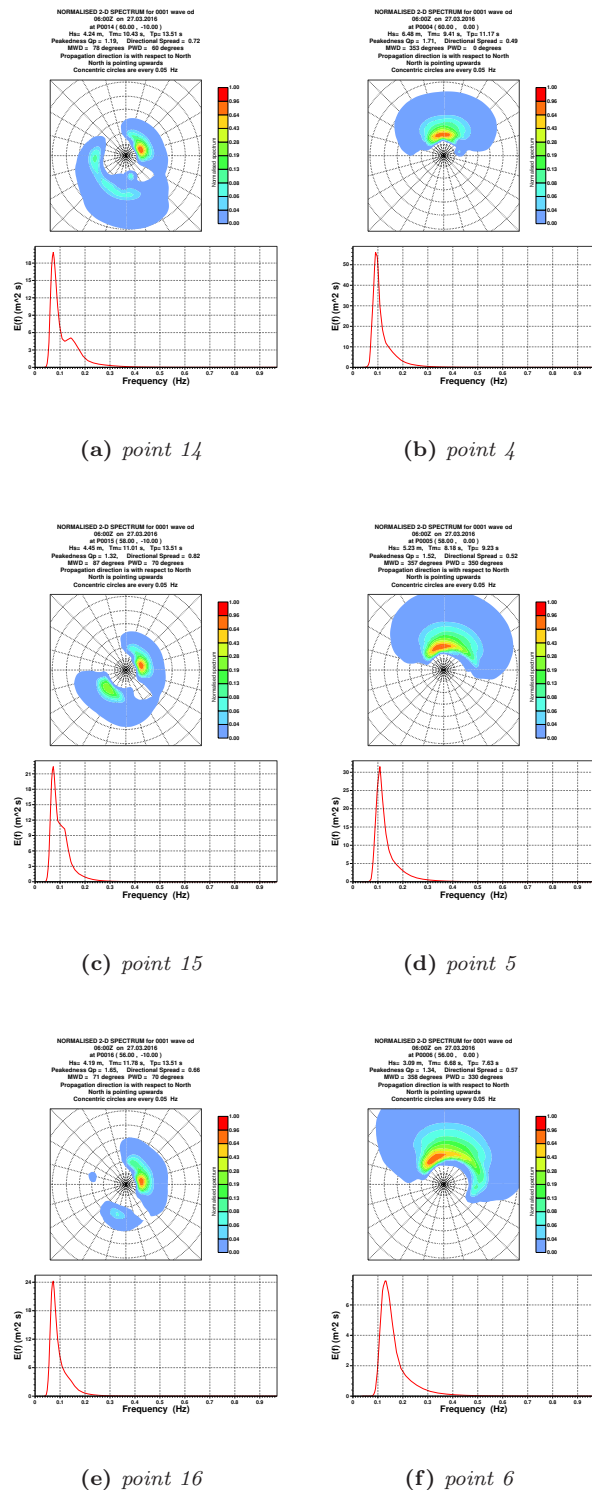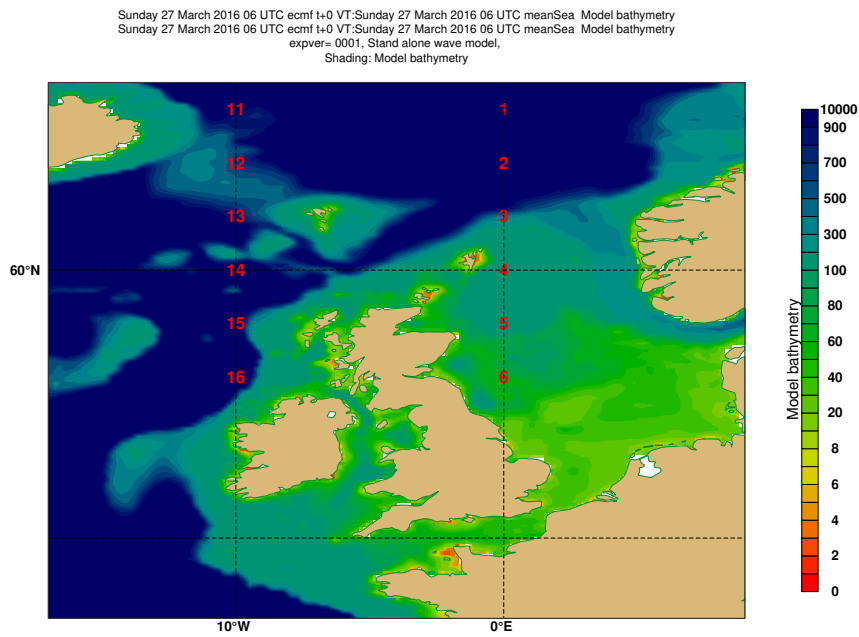
(a) *point 14*

(b) *point 4*

(c) *point 15*

(d) *point 5*

(e) *point 16*

(f) *point 6*

Figure 10.2 *Normalised 2d spectra (top of each panel) and frequency spectra (bottom of each panel) on 23 March 2016, 6 UTC, for locations shown in Figure 10.3. The 2-D spectra were normalised by their respective maximum value. The concentric circles in the polar plots are spaced every 0.05 Hz*

Sunday 27 March 2016 06 UTC ecmf t+0 VT:Sunday 27 March 2016 06 UTC meanSea Model bathymetry
Sunday 27 March 2016 06 UTC ecmf t+0 VT:Sunday 27 March 2016 06 UTC meanSea Model bathymetry
expver= 0001, Stand alone wave model,
Shading: Model bathymetry

Figure 10.3 *Model bathymetry (m) and locations for wave spectra (red numbers) in Figures 10.1 and 10.2.*

Sunday 27 March 2016 06 UTC ecmf t+0 VT:Sunday 27 March 2016 06 UTC meanSea Mean wave period/Mean wave direction
Sunday 27 March 2016 06 UTC ecmf t+0 VT:Sunday 27 March 2016 06 UTC meanSea Significant height of combined wind waves and swell
Sunday 27 March 2016 06 UTC ecmf t+0 VT:Sunday 27 March 2016 06 UTC meanSea Significant height of combined wind waves and swell
expver= 0001, Stand alone wave model,
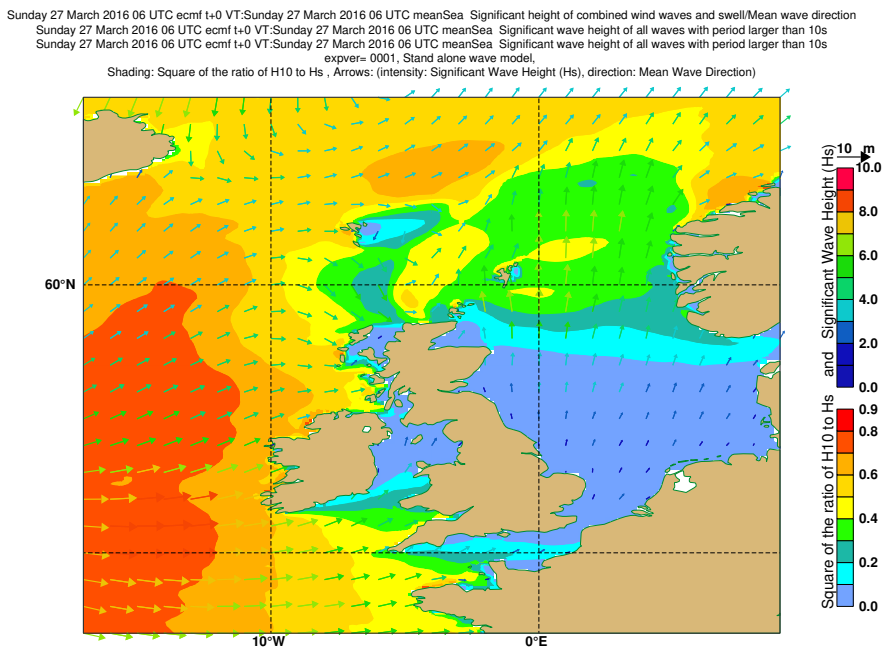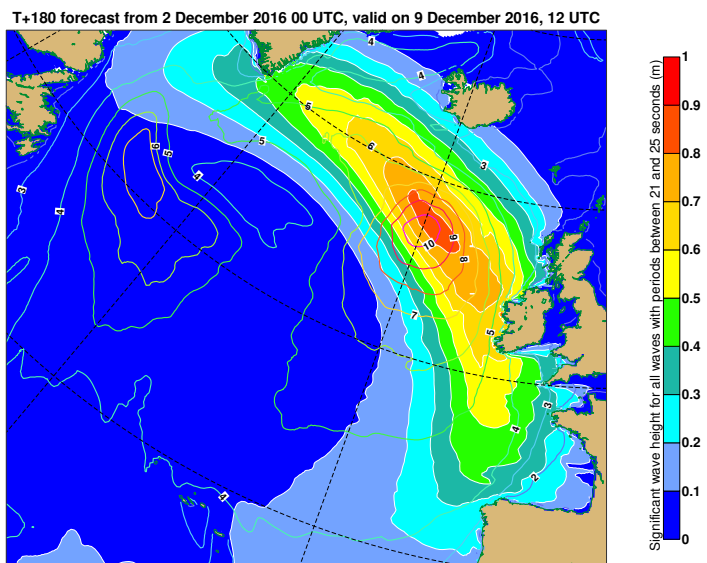Shading: Significant Wave Height, Arrows: (intensity:Mean Energy Wave Period, direction:Mean Wave direction)

Figure 10.4 *Significant wave height (H_s) (colour shading), Mean Wave Direction (arrow direction) and Mean Wave Period (T_{m-1}) (arrow length and colour) on 23 March 2016, 6 UTC.*
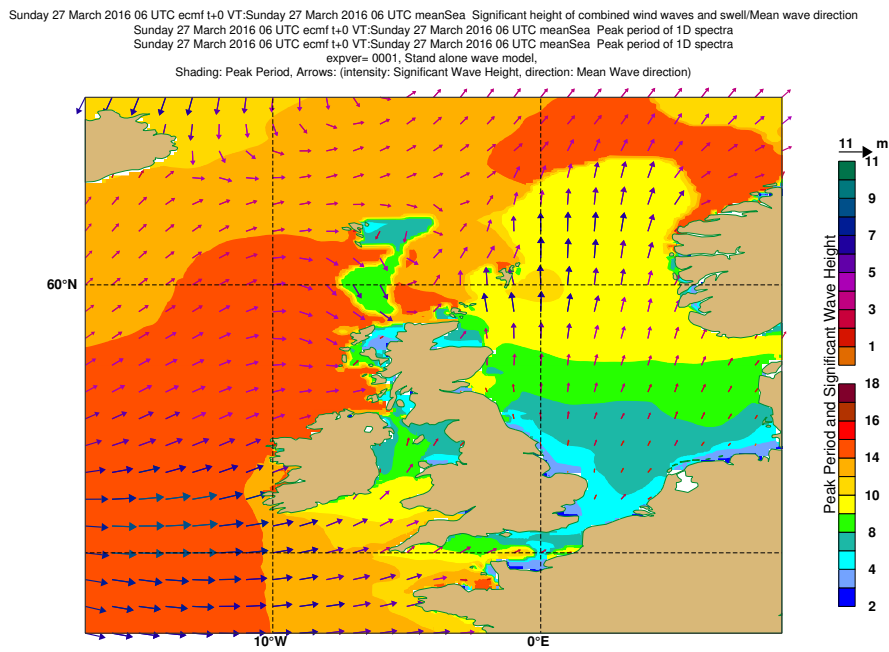
Figure 10.5 *10m neutral Wind Speed (colour shading, arrow length and grey scale), 10m Wind Direction (arrow direction) on 23 March 2016, 6 UTC.*

Figure 10.6 *Square of the ratio of H_{10} to H_s (colour shading), Significant Wave Height (H_s) (arrow length and colour) on 23 March 2016, 6 UTC.*

T+180 forecast from 2 December 2016 00 UTC, valid on 9 December 2016, 12 UTC
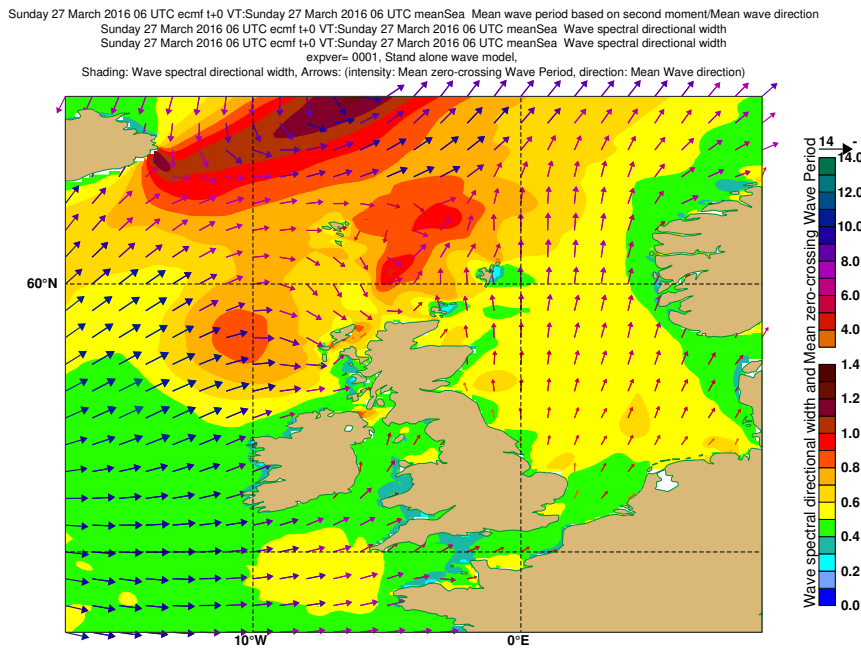

Figure 10.7 *Equivalent significant wave height of all waves with period between 21 and 25 seconds H_{2125} (colour shading), Significant Wave Height (H_s) (coloured contours) on 9 December 2016, 12 UTC.*
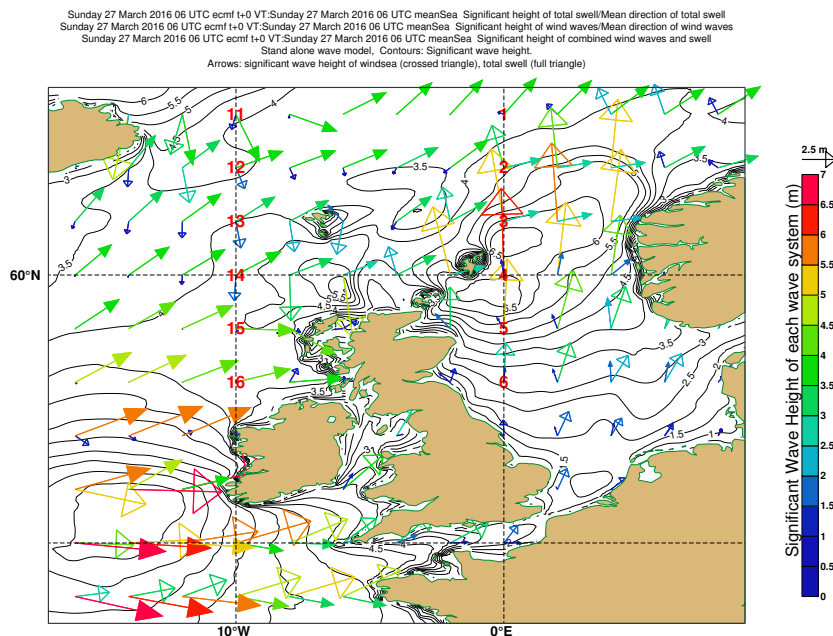
Sunday 27 March 2016 06 UTC ecmf t+0 VT:Sunday 27 March 2016 06 UTC meanSea Significant height of combined wind waves and swell/Mean wave direction
Sunday 27 March 2016 06 UTC ecmf t+0 VT:Sunday 27 March 2016 06 UTC meanSea Peak period of 1D spectra
Sunday 27 March 2016 06 UTC ecmf t+0 VT:Sunday 27 March 2016 06 UTC meanSea Peak period of 1D spectra
expver= 0001, Stand alone wave model,
Shading: Peak Period, Arrows: (intensity: Significant Wave Height, direction: Mean Wave direction)

Figure 10.8 *Peak Period (T_p) (colour shading), Mean Wave Direction (arrow direction) and Significant Wave Height (H_s) (arrow length and colour) on 23 March 2016, 6 UTC.*
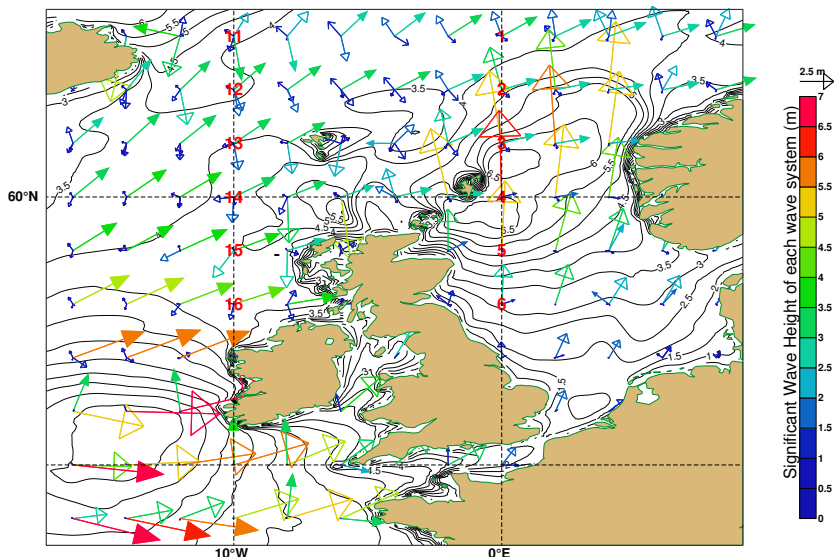
Sunday 27 March 2016 06 UTC ecmf t+0 VT:Sunday 27 March 2016 06 UTC meanSea Mean wave period based on second moment/Mean wave direction
Sunday 27 March 2016 06 UTC ecmf t+0 VT:Sunday 27 March 2016 06 UTC meanSea Wave spectral directional width
Sunday 27 March 2016 06 UTC ecmf t+0 VT:Sunday 27 March 2016 06 UTC meanSea Wave spectral directional width
expver= 0001, Stand alone wave model,
Shading: Wave spectral directional width, Arrows: (intensity: Mean zero-crossing Wave Period, direction: Mean Wave direction)

Figure 10.9 *Directional spread for total sea (colour shading), Mean Wave Direction (arrow direction) and Mean Wave Period (T_{m2}) (arrow length and colour) on 23 March 2016, 6 UTC.*

Sunday 27 March 2016 06 UTC ecmf t+0 VT:Sunday 27 March 2016 06 UTC meanSea Significant height of total swell/Mean direction of total swell
Sunday 27 March 2016 06 UTC ecmf t+0 VT:Sunday 27 March 2016 06 UTC meanSea Significant height of wind waves/Mean direction of wind waves
Sunday 27 March 2016 06 UTC ecmf t+0 VT:Sunday 27 March 2016 06 UTC meanSea Significant height of combined wind waves and swell
Stand alone wave model, Contours: Significant wave height.
Arrows: significant wave height of windsea (crossed triangle), total swell (full triangle)

Figure 10.10 *Windsea Significant Wave Height (arrow length and colour with open crossed triangle head), TOTAL swell Significant Wave Height (arrow length and colour with full triangle head), and significant wave height (black contours) on 23 March 2016, 6 UTC. The red numbers are the locations for wave spectra in Figures 10.1 and 10.2.*
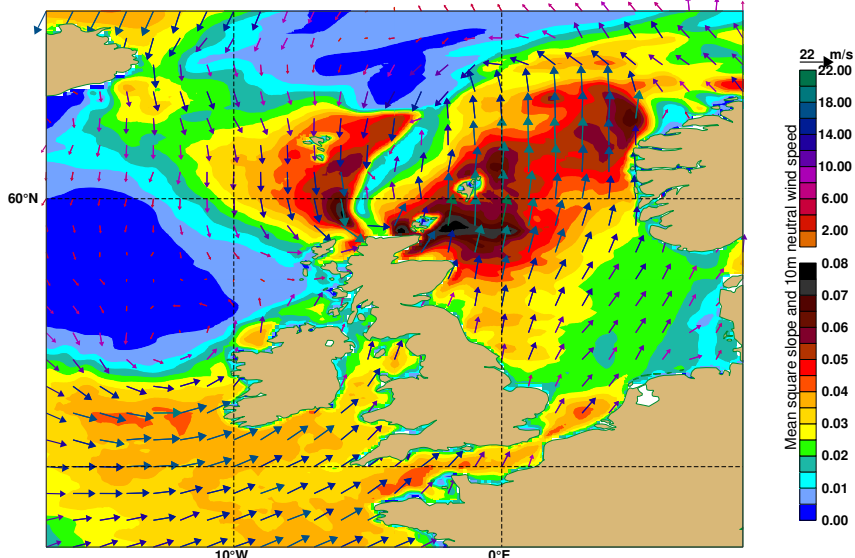
Figure 10.11 *Windsea Significant Wave Height (arrow length and colour with open crossed triangle head), Primary swell Significant Wave Height (arrow length and colour with full triangle head), Secondary swell Significant Wave Height (arrow length and colour with open triangle head), Tertiary swell Significant Wave Height (arrow length and colour with chevron head), and significant wave height (black contours) on 23 March 2016, 6 UTC. The red numbers are the locations for wave spectra in Figures 10.1 and 10.2.*

Figure 10.12 *Mean Square Slope (colour shading), 10m Wind (arrows) on 23 March 2016, 6 UTC.*
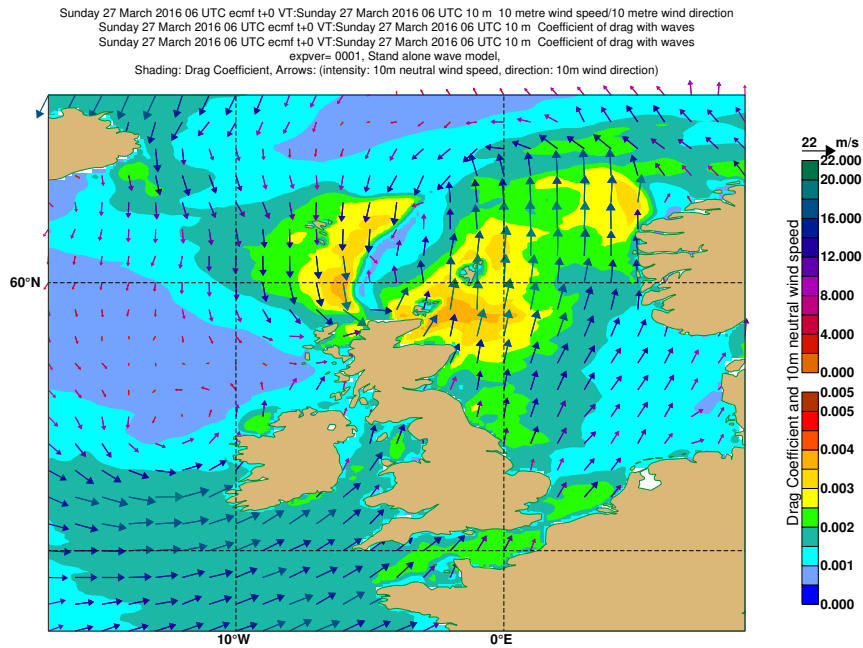
Figure 10.13 *Wave modified drag coefficient (C_d) (colour shading), and 10m neutral winds (arrows) on 23 March 2016, 6 UTC.*
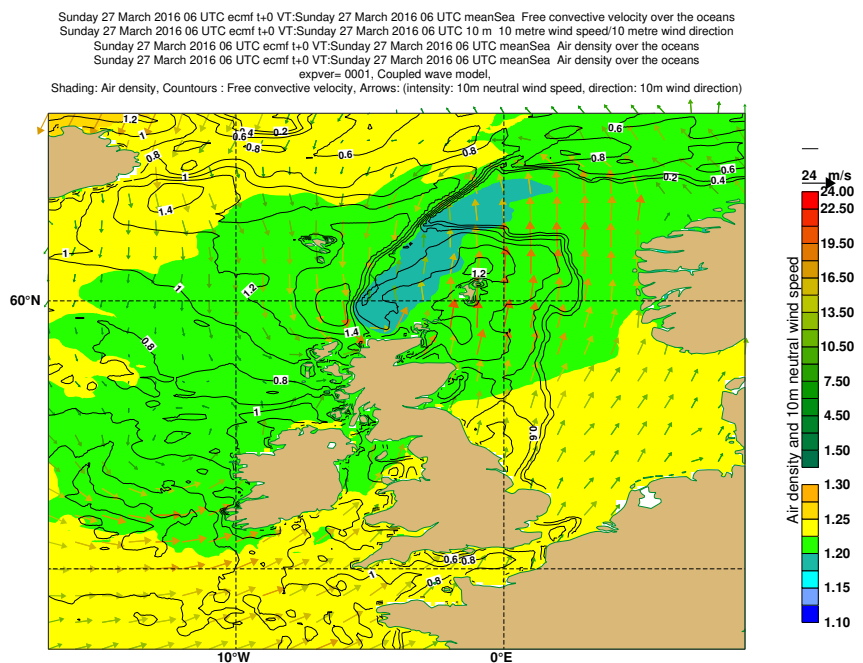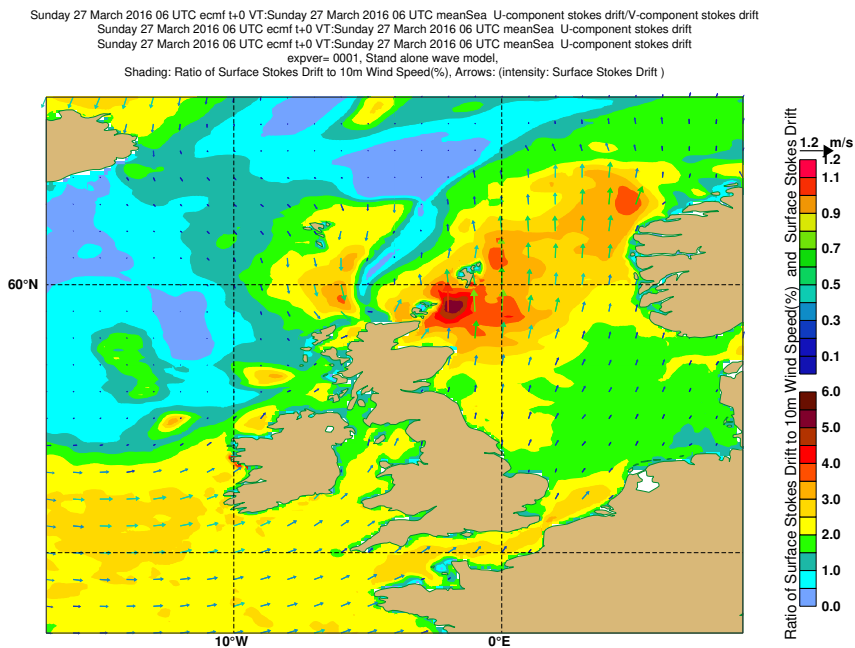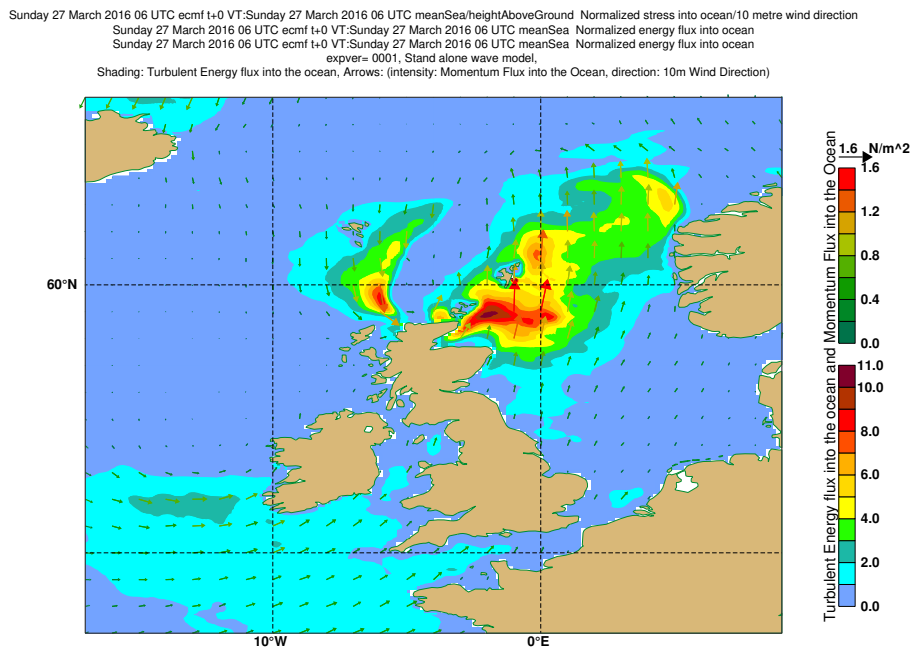
Figure 10.14 *Surface air density (ρ_{air}) (colour shading), free convection velocity scale (w_*) (black contours), and 10m neutral winds (arrows) on 23 March 2016, 6 UTC.*

Sunday 27 March 2016 06 UTC ecmf t+0 VT:Sunday 27 March 2016 06 UTC meanSea U-component stokes drift/V-component stokes drift
Sunday 27 March 2016 06 UTC ecmf t+0 VT:Sunday 27 March 2016 06 UTC meanSea U-component stokes drift
Sunday 27 March 2016 06 UTC ecmf t+0 VT:Sunday 27 March 2016 06 UTC meanSea U-component stokes drift
expver= 0001, Stand alone wave model,
Shading: Ratio of Surface Stokes Drift to 10m Wind Speed(%), Arrows: (intensity: Surface Stokes Drift)
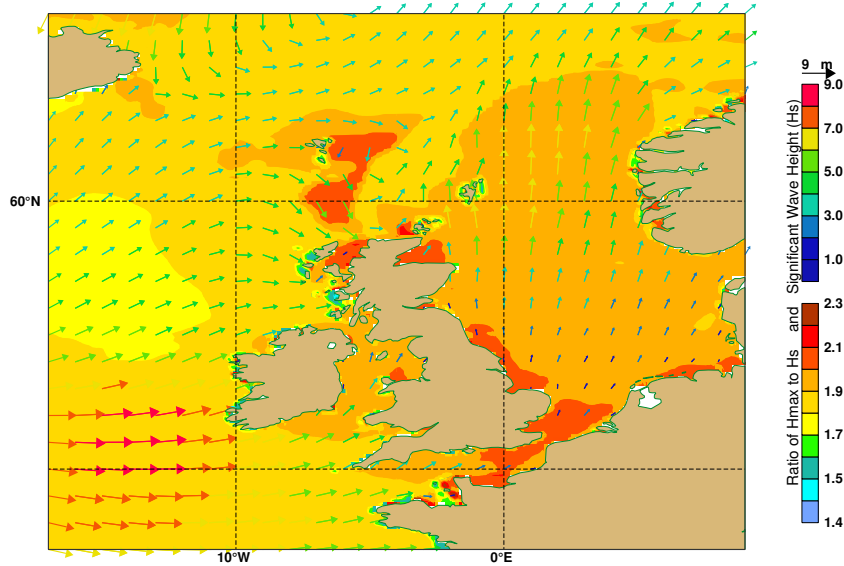
Figure 10.15 *Ratio (in percentage) of the surface Stokes drift magnitude to the 10m wind speed (colour shading), surface Stokes drift (arrow length and colour) on 23 March 2016, 6 UTC.*

Sunday 27 March 2016 06 UTC ecmf t+0 VT:Sunday 27 March 2016 06 UTC meanSea/heightAboveGround Normalized stress into ocean/10 metre wind direction
Sunday 27 March 2016 06 UTC ecmf t+0 VT:Sunday 27 March 2016 06 UTC meanSea Normalized energy flux into ocean
Sunday 27 March 2016 06 UTC ecmf t+0 VT:Sunday 27 March 2016 06 UTC meanSea Normalized energy flux into ocean
expver= 0001, Stand alone wave model,
Shading: Turbulent Energy flux into the ocean, Arrows: (intensity: Momentum Flux into the Ocean, direction: 10m Wind Direction)

Figure 10.16 *Wave energy flux into the ocean (colour shading), and momentum flux into the ocean (arrows) on 23 March 2016, 6 UTC.*

Figure 10.17 *Ratio of H_{max} to H_s (colour shading), Significant Wave Height (H_s) (arrow length and colour) on 23 March 2016, 6 UTC.*

References

A., M., Bortolozzo, U., Residori, S. and Arecchi, F. (2009). Non-gaussian statistics and extreme waves in a nonlinear optical cavity. *Physical Review Letters*, **103**, 173901.

Abdalla, S. and Bidlot, J. (2002). Wind gustiness and air density effects and other key changes to the wave model in cy25r1. *ECMWF Research Department Memo R60.9/SA/0273.*

A.E.M., J. P. and Janssen, A. J. (2019). Extreme ocean waves are a transient phenomenon. *J. Fluid Mech.*, **859**, 720–818.

Ardhuin, F., Rogers, W., Babanin, A., Filipot, J.-F. and R. Magne, A. v. d. W. P. Q. J.-M. L. L. A. F. C., A. Roland (2010). Semi-empirical dissipation source functions for ocean waves: Part i, definitions, calibration, and validations. *J. Phys. Oceanogr.*, **40**, 1917–1941.

Banner, M. L. (1990). Equilibrium spectra of wind waves. *J. Phys. Oceanogr.*, **20**, 966–984.

Barrick, D. E. and Weber, B. L. (1977). On the nonlinear theory for gravity waves on the ocean's surface. part ii: Interpretation and applications. *J. Phys. Oceanogr.*, **7**, 111–21.

Bauer, E., Hasselmann, S., Hasselmann, K. and Graber, H. C. (1992). Validation and assimilation of Seasat altimeter wave heights using the WAM wave model. *J. Geophys. Res.*, **C97**, 12671–12682.

Bidlot, J.-R. and Janssen, P. (2003). Unresolved bathymetry, neutral winds, and new stress tables in WAM. *ECMWF Research Department Memo R60.9/JB/0400.*

Bidlot, J.-R., Janssen, P. and Abdalla, S. (2006). A revised formulation of ocean wave dissipation and its model impact. *ECMWF Tech. Memo. No. 509.*

Birch, K. G. and Ewing, J. A. (1986). Observations of wind waves on a reservoir. *IOS-Rep. No. 234*, Wormley, 37 p.

Booij, N. and Holthuijsen, L. H. (1987). Propagation of ocean waves in discrete spectral wave models. *J. Comp. Phys.*, **68**, 307–326.

Breivik, L.-A., Reistad, M., Schyberg, H. and Sunde, J. (1998). Assimilation of ERS SAR wave spectra in an operational wave model. *J. Geophys. Res.*, **103**, 7887–7900.

Burgers, G., Koek, F., de Vries, H. and Stam, M. (2008). Searching for factors that limit observed extreme maximum wave height distributions in the north sea. In E. Pelinovsky and C. Kharif (Eds), *Extreme Ocean Waves*, *Springer Science+Business Media B.V.*, Vol. I, pp. 127–138.

Charnock, H. (1955). Wind stress on a water surface. *Q. J. R. Meteorol. Soc.*, **81**, 639–640.

Chi Wai Li (1992). A split operator scheme for ocean wave simulation. *Int. J. for Numerical Methods in Fluids*, **15**, 579–593.

Creamer, D. B., Heney, F., Schult, R. and Wright, J. (1989). Improved linear representation of ocean surface waves. *J. Fluid Mech.*, **205**, 135–161.

D. R. Crawford, P. G. S., B. M. Lake and Yuen, H. C. (1981). Stability of weakly nonlinear deep-water waves in two and three dimensions. *J. Fluid Mech.*, **105**, 177–191.

Dorrestein, R. (1960). Simplified method of determining refraction coefficients for sea waves. *J. Geophys. Res.*, **65**, 637–642.

Doyle J., C. A. S. C., P. Black and Wang, S. (2012). Wind-wave interactions under hurricane conditions. In *Proc. ECMWF Workshop on Ocean Waves*, 25-27 June 2012, Reading, UK.

Edson, J. B., Jampana, V., Weller, R. A., Bigorre, S. P., Plueddemann, A. J., Fairall, C. W., Miller, S. D., Mahrt, L., Vickers, D. and Hersbach, H. (2013). On the exchange of momentum over the open ocean. *J. Phys. Oceanogr.*, **43**, 1589–1610.

Edson, J. B., Jampana, V., Weller, R. A., Bigorre, S. P., Plueddemann, A. J., Fairall, C. W., Miller, S. D., Mahrt, L., Vickers, D. and Hersbach, H. (2014). On the exchange of momentum over the open ocean. *J. Phys. Oceanogr.*, **44**, 2590–2590.

Elfouhaily, T., Thompson, D., Vandemark, D. and Chapron, B. (1999). Weakly nonlinear theory and sea state bias estimations. *J. Geophys. Res.*, **106**, 7641–7647.

Forristall, G. Z. (1981). Measurements of saturated range in ocean wave spectra. *J. Geophys. Res.*, **86**, 8075–8089.

Groves, G. W. and Melcer, J. (1961). On the propagation of ocean waves on a sphere. *Geof. Int.*, **8**, 77–93.

Günther, H., Hasselmann, S. and Janssen, P. A. E. M. (1991). Wamodel cycle 4. *DKRZ Report No. 4*, Hamburg.

Günther, H., Lionello, P., Janssen, P. A. E. M., Bertotti, L., Brüning, C., Carretero, J. C., Cavaleri, L., Guillaume, A., B.Hansen, Hasselmann, S., Hasselmann, K., de las Heras, M., Hollingsworth, A., Holt, M., Lefevre, J. M. and Portz, R. (1992). Implementation of a third generation ocean wave model at the European Centre for Medium Range Weather Forecasts. Final report for EC Contract SC1-0013-C(GDF), ECMWF, Reading.

Hansen, B. and Günther, H. (1992). ERS-1 radar altimeter validation with the WAM model. In *Proc. ERS-1 Geophysical Validation Workshop*, European Space Agency, Paris, pp. 157–161.

Hanson, J. and Phillips, O. (2001). Automated Analysis of Ocean Surface Directional Wave Spectra. *J. Atmos. Oceanic. Technol.*, **18**, 277–293.

Hardy, T., Mason, L. and McConochie, J. (2001). A wave generation model for the Great Barrier Reef. *Ocean Engineering*, **28**, 45–70.

Hasselmann, D. E., Bösenberg, J., Dunckel, M., Richter, K., Grünewald, M. and Carlson, H. (1986). Measurements of wave-induced pressure over surface gravity waves. In O. M. Phillips and K. Hasselmann (Eds), *Wave Dynamics and Radio Probing of the Ocean Surface*, pp. 353–370, Plenum.

Hasselmann, K. (1962). On the non-linear energy transfer in a gravity-wave spectrum, part 1: general theory. *J. Fluid Mech.*, **12**, 481.

Hasselmann, K. (1974). On the spectral dissipation of ocean waves due to whitecapping. *Boundary-Layer Meteorol.*, **6**, 107–127.

Hasselmann, K., Barnett, T. P., Bouws, E., Carlson, H., Cartwright, D. E., Enke, K., Ewing, J. A., Gienapp, H., Hasselmann, D. E., Kruseman, P., Meerburg, A., Müller, P., Olbers, D. J., Richter, K., Sell, W. and Walden, H. (1973). Measurements of wind-wave growth and swell decay during the Joint North Sea Wave Project (JONSWAP). *Dtsch. Hydrogr. Z. Suppl. A*, **8(12)**, 95 p.

Hasselmann, K., Hasselmann, S., Bauer, E., Brüning, C., Lehner, S., Graber, H. and Lionello, P. (1988). Development of a satellite SAR image spectra and altimeter wave height data assimilation system for ERS-1. *ESA Report*, Max-Planck-Institute für Meteorologie, Nr. 19, Hamburg, 155 p.

Hasselmann, K., Ross, D. B., Müller, P. and Sell, W. (1976). A parametric wave prediction model. *J. Phys. Oceanogr.*, **6**, 200–228.

Hasselmann, S., Brüning, C., Hasselmann, K. and Heimbach, P. (1996). An improved algorithm for the retrieval of ocean wave spectra from SAR image spectra. *J. Geophys. Res.*, **101**, 16615–16629.

Hasselmann, S. and Hasselmann, K. (1985). Computations and parameterizations of the nonlinear energy transfer in a gravity-wave spectrum, part 1: A new method for efficient computations of the exact nonlinear transfer integral. *J. Phys. Oceangr.*, **15**, 1369–1377.

Hasselmann, S., Hasselmann, K., Allender, J. H. and Barnett, T. P. (1985). Computations and parameterizations of the nonlinear energy transfer in a gravity wave spectrum, part 2: Parameterizations of the nonlinear energy transfer for application in wave models. *J. Phys. Oceanogr.*, **15**, 1378–1391.

Hasselmann, S., Lionello, P. and Hasselmann, K. (1997). An optimal interpolation scheme for the assimilation of spectral data. *J. Geophys. Res.*, **102**, 15823–15836.

Hersbach, H. and Janssen, P. A. E. M. (1999). Improvement of the Short-Fetch Behavior in the Wave Ocean Model (WAM). *J. Atmos. Oceanic. Technol.*, **16**, 884–892.

Hoffschildt, M., Bidlot, J.-R., Hansen, B. and Janssen, P. A. E. M. (1999). Potential benefit of ensemble forecasts for ship routing. *ECMWF Tech. Memo. No. 287*.

Holthuijsen, M. D. P., L. H. and Pietrzak, J. D. (2012). Wind and waves in extreme hurricanes. *J. Geophys. Res.*, **117**, doi:10.1029/2012JC007983.

Hwang, P. A. and Wang, D. W. (2004). Field measurements of duration-limited growth of wind-generated ocean surface waves at young stage of development. *J. Phys. Oceanogr.*, **34**, 2316–2326.

Janssen, P. (2004). *The Interaction of Ocean Waves and Wind*. Cambridge University Press.

Janssen, P. A. E. M. (1982). Quasilinear approximation for the spectrum of wind-generated water waves. *J. Fluid Mech.*, **117**, 493–506.

Janssen, P. A. E. M. (1989). Wave-induced stress and the drag of air flow over sea waves. *J. Phys. Oceanogr.*, **19**, 745–754.

Janssen, P. A. E. M. (1991). Quasi-linear theory of wind wave generation applied to wave forecasting. *J. Phys. Oceanogr.*, **21**, 1631–1642.

Janssen, P. A. E. M. (1992). Experimental evidence of the effect of surface waves on the airflow. *J. Phys. Oceanogr.*, **22**, 1600–1604.

Janssen, P. A. E. M. (2000). ECMWF wave modeling and satellite altimeter wave data. In D. Halpern (Ed.), *Satellites, Oceanography and Society*, pp. 35–56, Elsevier.

Janssen, P. A. E. M. (2003). Nonlinear four-wave interactions and freak waves. *J. Phys. Oceanogr.*, **33**, 863–884.

Janssen, P. A. E. M. (2008). Some consequences of the canonical transformation in the Hamiltonian theory of water waves. *ECMWF Tech. Memo. No. 579*.

Janssen, P. A. E. M. (2009). On some consequences of the canonical transformation in the hamiltonian theory of water waves. *J. Fluid Mech.*, **637**, 1–44.

Janssen, P. A. E. M. (2014). On a random time series analysis valid for arbitrary spectral shape. *J. Fluid Mech.*, **759**, 236–256.

Janssen, P. A. E. M. (2015a). How rare is the draupner wave event? *ECMWF Tech. Memo. No. 775*.

Janssen, P. A. E. M. (2015b). Notes on the maximum wave height distribution. *ECMWF Tech. Memo. No. 755*.

Janssen, P. A. E. M. (2017). Shallow water version of the freak wave warning system. *ECMWF Tech. Memo. No. 813*.

Janssen, P. A. E. M. and Bidlot, J.-R. (2001). Impact of revised roughness length calculation on the occurrence of mini-vortices. *ECMWF Research Memo R60.9/PJ/44*, Reading, U.K.

Janssen, P. A. E. M. and Bidlot, J.-R. (2009). On the extension of the freak wave warning system and its verification. *ECMWF Tech. Memo. No. 588*.

Janssen, P. A. E. M., Bidlot, J.-R. and Hansen, B. (2000). Diagnosis of the ECMWF ocean-wave forecasting system. *ECMWF Tech. Memo. No. 318*.

Janssen, P. A. E. M. and Bouws, E. (1986). On the minimum width of a ravity wave spectrum. *KNMI-OO Memorandum No. OO-86-01*.

Janssen, P. A. E. M., Doyle, J. D., Bidlot, J.-R., Hansen, B., Isaksen, L. and Viterbo, P. (2001). Impact and feedback of ocean waves on the atmosphere. In W. Perrie (Ed.), *Advances in Fluid Mechanics*, *Atmosphere-Ocean Interactions*, Vol. I, pp. 155–198.

Janssen, P. A. E. M., Hansen, B. and Bidlot, J.-R. (1997). Validation of ERS Satellite Wave Products with the WAM model. *CEOS Wind and Wave Validation Workshop*, 3–5 June 1997, ESTEC, The Netherlands, ESA WPP-**147**, 101–108.

Janssen, P. A. E. M. and Komen, G. J. (1985). Effect of the atmospheric stability on the growth of surface gravity waves. *Boundary-Layer Meteorol.*, **32**, 85–96.

Janssen, P. A. E. M., Lionello, P., Reistad, M. and Hollingsworth, A. (1987). A study of the feasibility of using sea and wind information from the ERS-1 satellite, part 2: Use of scatterometer and altimeter data in wave modelling and assimilation. *ECMWF Report to ESA*, Reading.

Janssen, P. A. E. M., Lionello, P., Reistad, M. and Hollingsworth, A. (1989a). Hindcasts and data assimilation studies with the WAM model during the Seasat period. *J. Geophys. Res.*, **C94**, 973–993.

Janssen, P. A. E. M., Lionello, P. and Zambresky, L. (1989b). On the interaction of wind and waves. *Philos. Trans. Roy. Soc. London*, **A329**, 289–301.

Janssen, P. A. E. M. and Onorato, M. (2007). The intermediate water depth limit of the zakharov equation and consequences for wave prediction. *J. Phys. Oceanogr.*, **37**, 2389–2400.

Katsaros, K. B., Smith, S. D. and Oost, W. A. (1987). HEXOS - Humidity Exchange Over the Sea. A program for research on water-vapor and droplet fluxes from sea to air at moderate to high wind speeds. *Bull. Am. Meteorol. Soc.*, **68**, 466–476.

Kitaigorodskii, S. A. (1962). Application of the theory of similarity to the analysis of wind-generated water waves as a stochastic process. *Bull. Acad. Sci. USSR Geophys.*, Ser. no. 1, 73 p.

Komen, G. J., Cavaleri, L., Donelan, M., Hasselmann, K., Hasselmann, S. and Janssen, P. A. E. M. (1994). *Dynamics and Modelling of Ocean Waves*. Cambridge University Press.

Komen, G. J., Hasselmann, K. and Hasselmann, S. (1984). On the existence of a fully developed windsea spectrum. *J. Phys. Oceanogr.*, **14**, 1271–1285.

Lionello, P., Günther, H. and Janssen, P. A. E. M. (1992). Assimilation of altimeter data in a global third generation wave model. *J. Geophys. Res.*, **C97**, 14453–14474.

Lionello, P. and Janssen, P. A. E. M. (1990). Assimilation of altimeter measurements to update swell spectra in wave models. In *Proc. of the International Symposium on Assimilation of Observations in Meteorology and Oceanography* (Clermont-Ferrand, France), pp. 241–246, World Meteorological Organization.

Longuet-Higgins, M. S. (1963). The effect of non-linearities on statistical distributions in the theory of sea waves. *J. Fluid Mech.*, **17**, 459–480.

Longuet-Higgins, M. S. (1983). On the joint distribution of wave periods and amplitudes in a random wave field. *Proc. Roy. Soc. London*, **A389**, 241–258.

Lorenc, A. C. (1981). A global three-dimensional multivariate statistical interpolation scheme. *Mon. Wea. Rev.*, **109**, 701–721.

Miles, J. W. (1957). On the generation of surface waves by shear flows. *J. Fluid Mech.*, **3**, 185–204.

Mitsuyasu, H. (1968). On the growth of the spectrum of wind-generated waves. 1. *Rep. Res. Inst. Appl. Mech., Kyushu Univ.*, **16**, 251–264.

Mitsuyasu, H. (1969). On the growth of the spectrum of wind-generated waves. 2. *Rep. Res. Inst. Appl. Mech., Kyushu Univ.*, **17**, 235–243.

Mori, N. and Janssen, P. A. E. M. (2006). On kurtosis and occurrence probability of freak waves. *J. Phys. Oceanogr.*, **36**, 1471–1483.

Panofsky, H. A., Tennekes, H., Lenschow, D. and Wyngaard, J. (1977). The characteristics of turbulent velocity components in the surface layer under convective conditions. *Boundary-Layer Meteorol.*, **11**, 355–361.

Phillips, O. M. (1958). The equilibrium range in the spectrum of wind-generated water waves. *J. Fluid Mech.*, **4**, 426–434.

Plant, W. J. (1982). A relation between wind stress and wave slope. *J. Geophys. Res.*, **C87**, 1961–1967.

Saetra, O. (2004). Ensemble shiprouting. *ECMWF Tech. Memo. No. 435*.

Saetra, O. and Bidlot, J.-R. (2002). Assessment of the ECMWF ensemble prediction system for waves and marine winds. *ECMWF Tech. Memo. No. 388*.

Saetra, O. and Bidlot, J.-R. (2004). On the potential benefit of using probabilistic forecast for waves and marine winds based on the ECMWF ensemble prediction system. *Weather Forecasting*, **19**, 673–689.

Shyu, J. H. and Phillips, O. M. (1990). The blockage of gravity and capillary waves by longer waves and currents. *J. Fluid Mech.*, **217**, 115–141.

Snyder, R. L., Dobson, F. W., Elliott, J. A. and Long, R. B. (1981). Array measurements of atmospheric pressure fluctuations above surface gravity waves. *J. Fluid Mech.*, **102**, 1–59.

Stansell, P. (2005). Distributions of extreme wave, crest and trough heights measured in the north sea. *Ocean Engineering*, **32**, 1015–1036.

SWAMP Group: Allender, J. H., Barnett, T. P., Bertotti, L., Bruinsma, J., Cardone, V. J., Cavaleri, L., Ephraums, J., Golding, B., Greenwood, A., Guddal, J., Günther, H., Hasselmann, K., Hasselmann, S., Joseph, P., Kawai, S., Komen, G. J., Lawson, L., Linné, H., Long, R. B., Lybanon, M., Maeland, E., Rosenthal, W., Toba, Y., Uji, T. and de Voogt, W. J. P. (1985). Sea wave modeling project (SWAMP). An intercomparison study of wind wave predictions models, part 1: Principal results and conclusions. In *Ocean Wave Modeling*, Plenum, 256 p.

Takaya, Y., Bidlot, J.-R., Beljaars, A. C. M. and Janssen, P. A. E. M. (2010). Refinements to a prognostic scheme of skin sea surface temperature. *J. Geophys. Res.*, **C115**, doi:10.1029/2009JC005985.

Thomas, J. (1988). Retrieval of energy spectra from measured data for assimilation into a wave model. *Q. J. R. Meteorol. Soc.*, **114**, 781–800.

Tick, L. J. (1959). A nonlinear random model of gravity waves. I. *J. Math. Mech.*, **8**, 643–651.

Tolman, H. L. (2000). *Private communication* at WISE meeting in Iceland.

Tolman, H. L. (2003). Treatment of unresolved islands and ice in wind wave models. *Ocean Modelling*, **5**, 219–231.

Voorrips, A. C., Makin, V. K. and Hasselmann, S. (1997). Assimilation of wave spectra from pitch- and-roll buoys in a North Sea wave model. *J. Geophys. Res.*, **102**, 5829–5849.

Voorrips, A. C., Makin, V. K. and Komen, G. J. (1994). The influence of atmospheric stratification on the growth of water waves. *Boundary-Layer Meteorol.*, **72**, 287–303.

WAMDI Group: Hasselmann, S., Hasselmann, K., Bauer, E., Janssen, P. A. E. M., Komen, G. J., Bertotti, L., Lionello, P., Guillaume, A., Cardone, V. C., Greenwood, J. A., Reistad, M., Zambresky, L. and Ewing, J. (1988). The WAM model - a third generation ocean wave prediction model. *J. Phys. Oceanogr.*, **18**, 1775–1810.

Waseda, T. (2006). Impact of directionality on the extreme wave occurrence in a discrete random wave system. In *Proc. 9th Int. Workshop on Wave Hindcasting and Forecasting*, Victoria, Canada.

Wu, J. (1982). Wind-stress coefficients over sea surface from breeze to hurricane. *J. Geophy. Res.*, **C87**, 9704–9706.

Zakharov, V. E. (1968). Stability of periodic waves of finite amplitude on the surface of a deep fluid. *J. Appl. Mech. Technol. Phys.*, **9**, 190–194.